OPTIMIZATION OF THE THERMAL-HYDRAULIC PERFORMANCE OF THE HELIUM-COOLED MODULAR DIVERTOR WITH MULTIPLE JETS

A Dissertation
Presented to
The Academic Faculty

by

Bailey Zhao

In Partial Fulfillment
of the Requirements for the Degree
Doctor of Philosophy in the
George W. Woodruff School of Mechanical Engineering

Georgia Institute of Technology
December 2017

OPTIMIZATION OF THE THERMAL-HYDRAULIC PERFORMANCE OF THE HELIUM-COOLED MODULAR DIVERTOR WITH MULTIPLE JETS

Approved by:

Dr. Minami Yoda, Co-Advisor
George W. Woodruff School of
Mechanical Engineering
Georgia Institute of Technology

Dr. Said I. Abdel-Khalik, Co-Advisor
George W. Woodruff School of
Mechanical Engineering
Georgia Institute of Technology

Dr. S. Mostafa Ghiaasiaan
George W. Woodruff School of
Mechanical Engineering
Georgia Institute of Technology

Dr. Yogendra Joshi
George W. Woodruff School of
Mechanical Engineering
Georgia Institute of Technology

Dr. Michael Schatz
School of Physics
Georgia Institute of Technology

Dr. Yutai Katoh
Materials Science and Technology
Division
Oak Ridge National Laboratory

Date Approved: November 6, 2017

ACKNOWLEDGMENTS

The completion of this dissertation would not have been possible without the support of many individuals. First, I would to thank my advisors, Dr. Said Abdel-Khalik and Dr. Minami Yoda for their valuable advice, patience, and encouragement throughout this process. Their guidance has helped me overcome challenges that have contributed to my growth as a researcher and engineer over the past few years, and their professionalism is greatly appreciated. I would also like to thank the rest of my thesis committee members, Dr. S. Mostafa Ghiaasiaan, Dr. Yogendra Joshi, Dr. Yutai Katoh, and Dr. Michael Schatz for their time and efforts in reviewing this work. Their feedback and perspectives were very beneficial to the progress of this research.

I am grateful to Dr. Brantley Mills for his mentorship and collaboration, especially during the earlier stages of this project. I learned a significant amount from him, and appreciate his patience during our transition period. My thanks goes to Shekaib Musa for his assistance with conducting many hours of experiments. Working together with him made the process more manageable.

I would like to thank Dr. Takehiko Yokomine, Dr. Kazuhisa Yuki, and Mr. Ken Ohara for the interesting discussions during their time in Atlanta. I would like to acknowledge Sercan Akdeniz, Matt Golob, Daniel Lee, Carlos Charry León, Dr. Yaofa Li, Dr. Tongran Qin, Dr. Vladimer Tsiklashvili, and Andrew Yee for their suggestions.

Finally, my deepest gratitude goes to my parents and family for their unconditional love, support, and understanding throughout two decades of education. Without them, I would not have been able to close this chapter of my life.

TABLE OF CONTENTS

LIST OF TABLES

LIST OF FIGURES

x

NOMENCLATURE

Roman Symbols

Symbol	Definition	Units
A_c	Cooled surface area	m^2
A_h	Heated surface area	m^2
A_j	Total area of jet holes in the HEMJ divertor	m^2
A_T	Hexagonal tile area of the HEMJ divertor	m^2
c	Speed of light	$m\,s^{-1}$
c_p	Constant-pressure specific heat	$J\,kg^{-1}\,K^{-1}$
D	Diameter	m
D_h	Hydraulic diameter	m
D_j	Jet hole diameter	m
D_o	Central jet hole diameter	m
E	Energy in a physical system	J
F	Peak-to-average heat flux ratio	$-$
F_{ij}	View factor from surface i to j	$-$
h	Local heat transfer coefficient	$W\,m^{-2}\,K^{-1}$
$\bar{h}$	Average heat transfer coefficient	$W\,m^{-2}\,K^{-1}$
H	Jet exit-to-impingement surface separation distance	m
I	Turbulence intensity	$-$
k	Turbulent kinetic energy	$m^2\,s^{-2}$
k_f	Thermal conductivity of the coolant	$W\,m^{-1}\,K^{-1}$
k_s	Thermal conductivity of the outer shell	$W\,m^{-1}\,K^{-1}$
K_L	Loss coefficient	$-$
l	Turbulence length scale	m
L	Length of the outer shell	m

L_c	Characteristic length	m
m	Mass	kg
$\dot{m}$	Mass flow rate	kg s^{-1}
$\dot{m}_p$	Prototypical mass flow rate for the HEMJ divertor	kg s^{-1}
$\overline{Nu}$	Average Nusselt number	–
Nu	Local Nusselt number	–
Δp	Pressure drop across the test section	Pa
p_i	Coolant inlet pressure	Pa
p_o	Coolant outlet pressure	Pa
Pr	Prandtl number	–
Q	Thermal power	W
$\overline{q''}$	Time-averaged incident heat flux	W m^{-2}
$\overline{q''_{max}}$	Maximum allowable heat flux on the heated surface	W m^{-2}
$\overline{q''_T}$	Maximum allowable heat flux on the hexagonal tile	W m^{-2}
r	Effective radius	m
R	Thermal resistance	K W^{-1}
Re	Reynolds number	–
Re_p	Prototypical Reynolds number for the HEMJ divertor	–
T_{ave}	Average of the inlet and outlet coolant temperatures	K
$\overline{T_c}$	Area-averaged cooled surface temperature	K
$T_{c,r}$	Extrapolated local cooled surface temperature	K
T_i	Coolant inlet temperature	K
T_∞	Ambient temperature	K
T_r	Measured thermocouple temperature	K
$\overline{T_s}$	Average temperature of the pressure boundary	K
T_o	Coolant outlet temperature	K

V	Fluid velocity	m s^{-1}
$\overline{V}$	Average coolant velocity over all jets	m s^{-1}
$\dot{W}$	Coolant pumping power	W

Greek Symbols

Symbol	Definition	Units
β	Pumping power as a fraction of incident thermal power	–
δ_{TC}	Distance from thermocouple holes to cooled surface	m
ε	Dissipation of turbulent kinetic energy	m^2 s^{-3}
ε	Total, normal emissivity (Chapter 3)	–
κ	Thermal conductivity ratio	–
μ	Dynamic viscosity	Pa·s
μ_i	Dynamic viscosity of He at T_i	Pa·s
$\tilde{v}$	Modified turbulent kinematic viscosity	m^2 s^{-1}
ρ	Density	kg m^{-3}
$\overline{\rho}$	Average of coolant densities at T_i and T_o	kg m^{-3}
ρ_i	Coolant inlet density	kg m^{-3}
ρ_L	Coolant density evaluated at T_i and p_o	kg m^{-3}
ρ_o	Coolant outlet density	kg m^{-3}
ρ_v	Coolant density at venturi meter inlet	kg m^{-3}
σ	Stefan-Boltzmann constant	W m^{-2} K^{-4}
σ_v	Von Mises stress	Pa
ω	Specific dissipation rate	s^{-1}

Abbreviations

ASME	American Society of Mechanical Engineers
CFC	Carbon Fiber Composites

CFD	Computational Fluid Dynamics
CTE	Coefficient of Thermal Expansion
DBTT	Ductile-to-Brittle Transition Temperature
DEMO	Demonstration fusion reactor
EB	Electron Beam
EDM	Electrical Discharge Machining
EWT	Enhanced Wall Treatment
FEM	Finite Element Method
FZK	Forschungszentrum Karlsruhe
HCFP	Helium-Cooled Flat Plate Divertor
HEMJ	Helium-cooled Modular Divertor with Multiple Jets
HEMP	Helium-cooled Modular Divertor with Integrated Pin Array
HEMS	Helium-cooled Modular Divertor with Integrated Slot Array
HHF	High Heat Flux
HTC	Heat Transfer Coefficient
IFE	Inertial Fusion Energy
IR	Infrared
KIT	Karlsruhe Institute of Technology
GPF	Gas Puffing Facility
LCFS	Last Closed Flux Surface
MFE	Magnetic Fusion Energy
NIST	National Institute of Standard and Technology
ODS	Oxide Dispersion-Strengthened
ORNL	Oak Ridge National Laboratory
PFC	Plasma-Facing Component
PMI	Plasma-Material Interactions
RANS	Reynolds-Averaged Navier-Stokes
RCT	Recrystallization Temperature
RF	Radio Frequency
RKE	Realizable k-ε
RNGKE	Renormalization Group k-ε

RTD	Resistance Temperature Detector
S-A	Spalart-Allmaras
SKE	Standard k-ε
SKO	Standard k-ω
SOL	Scrape-Off Layer
SST	Shear-Stress Transport
STAR	Safety and Tritium Applied Research
TC	Thermocouple
W	Tungsten

SUMMARY

Controlled nuclear fusion has the potential to be a sustainable, large-scale energy source that can support increasing global energy demands by leveraging the same principle that powers our Sun. Magnetic confinement fusion reactors are promising devices that utilize magnetic fields and thermal energy to initiate fusion reactions within "burning plasma" (*i.e.*, a high temperature ionized gas) at temperatures in excess of 10^8 K. The divertor is a key component of magnetic confinement reactors that removes impurities and fusion byproducts to help sustain fusion reactions. As one of the few plasma-facing components (PFC) however, the divertor surfaces must withstand high steady-state incident heat fluxes of at least 10 MW/m^2. Moreover, a significant fraction (~20%) of the total fusion thermal power must be removed by the divertor.

Modular helium-cooled tungsten divertors are leading candidates for future power-producing fusion reactors. Helium is chemically inert, and can be operated at high temperatures and pressures in a power conversion cycle to improve the overall efficiency of a reactor. Specifically, the helium-cooled modular divertor with multiple jets (HEMJ) is a leading candidate for the international demonstration power plant (DEMO). The HEMJ uses 25 impinging jets of helium at inlet temperatures of 600 °C and inlet pressures of 10 MPa to cool the plasma-facing tungsten tiles.

This dissertation focuses on experimentally and numerically evaluating the thermal-hydraulic performance of the HEMJ. Experiments were performed on a single HEMJ module to characterize its thermal-hydraulics at coolant inlet temperatures up to 425 °C, inlet pressures of 10 MPa, and incident heat fluxes up to 6.6 MW/m^2 using a helium

loop for mass flow rates up to 10 g/s. The effect of varying the jets impingement distance from 0.5 mm to 1.5 mm was investigated. The data were used to develop correlations for the average Nusselt number over the cooled surface and loss coefficient, which were then used to develop parametric design charts that predict performance at prototypical inlet temperatures of 600 °C and heat fluxes of 10 MW/m^2.

A numerical model was developed using commercial software, and validated by experimental data. The model was used to study the thermo-mechanical performance of the HEMJ at prototypical conditions, and estimate thermally-induced stresses and deformation. The results suggest that the HEMJ can accommodate 10 MW/m^2 while keeping pumping power requirements within reasonable limits. Numerical simulations were also performed to optimize the divertor geometry; based on these numerical optimizations, a simplified design, which could reduce manufacturing costs for the large number ($O(10^6)$) of modules required, was fabricated and tested in the helium loop. This variant can accommodate ~8 MW/m^2 at prototypical conditions.

CHAPTER 1: INTRODUCTION

1.1.   Background and Motivation

In the next century, major advances in environmentally sustainable energy sources are required to meet the energy consumption demands of a growing world population. Anthropogenic consumption of finite resources for energy production has resulted in an unprecedented increase of greenhouse gas emissions, such as carbon dioxide (CO_2) and methane, since the pre-industrial era [1]. In the past 70 years, the concentration of atmospheric CO_2 (Figure 1.1) has grown to record levels, emerging as a leading cause for an increased average Earth temperature [2, 3]. A variety of clean energy technologies including nuclear fission, fusion, and renewables must therefore be developed to satisfy a greater demand for electricity without adversely affecting the climate.
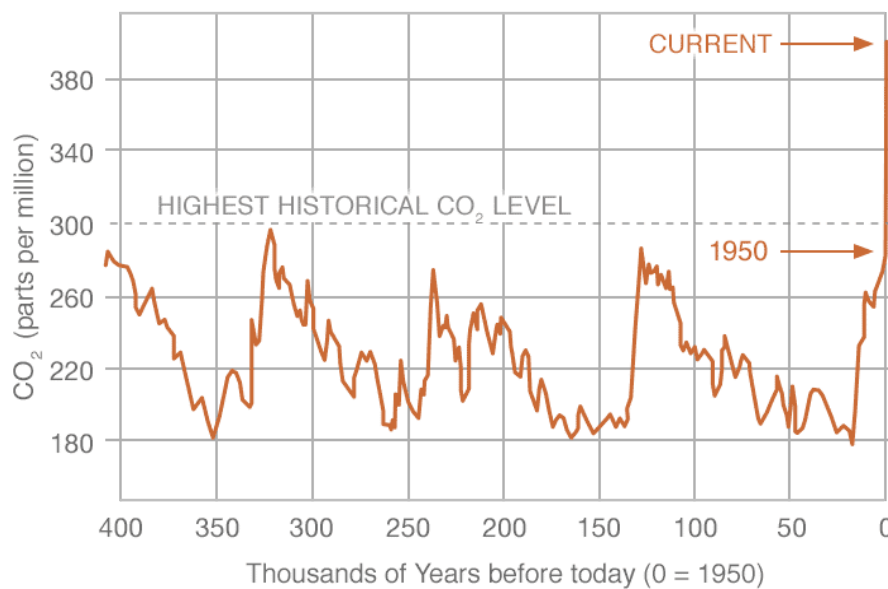
Figure 1.1. Atmospheric CO_2 levels during the last three glacial cycles [3].

Nuclear fission will make a notable contribution to electricity production but faces challenges in public acceptance, safety, and waste disposal. The vast majority of renewable sources are inherently intermittent, and considerable advances are needed to integrate energy storage systems into the current grid and provide constant baseload electricity.

Nuclear fusion offers carbon-free, large-scale energy with several important advantages over conventional systems. Fusion does not emit harmful toxins or greenhouse gases into the atmosphere since its major by-product is non-toxic, inert helium gas. Controlled fusion reactions release nearly four million times more energy than a chemical reaction such as burning coal. This type of energy density has the potential to provide the baseload electricity needed to power cities and industries. Fusion fuels are typically small quantities of hydrogen isotopes which can be harvested or produced from abundant and nearly inexhaustible sources such as the oceans. There is no risk of a meltdown in fusion devices since only small amounts of fuel are present in the reaction zone and any disturbances will rapidly quench the process. Finally, fusion devices preclude the use of enriched fissile materials, reducing the risk of nuclear proliferation.

The promise of harnessing fusion power has resulted in significant research on two ways to create fusion energy: inertial confinement fusion energy (IFE) and magnetic confinement fusion energy (MFE). Although IFE appeared to be a practical approach to fusion power generation when it was first proposed in the 1970s, low driver efficiencies have hindered its progress over the past few decades. In contrast, the best performance in terms of fusion power output, for example, has been achieved in MFE reactors, which is the subject of this dissertation.

Despite major strides in fundamental fusion science and predictive modeling, many challenges in areas such as plasma confinement, tritium sustainability, and plasma-material interactions (PMI) remain to be overcome before commercial fusion can become practical. Over the past decade, the fusion community has identified PMI as a knowledge gap critical to the progress of future power plants [4]. To that end, this work focuses on characterizing the performance of a particular plasma-facing component (PFC) in many modern MFE designs, namely, the divertor. Although a variety of divertor designs have been proposed, the most promising advanced concept is the helium-cooled modular tungsten divertor, which is described in more detail in the forthcoming sections.

In order to understand the role of the divertor in the context of MFE research, the remainder of this chapter will be dedicated to introducing several important concepts of fusion energy. First, the underlying principles of nuclear fusion will be briefly described. Next, an overview of the most prevalent MFE designs such as stellarators and tokamaks will be provided. Finally, details regarding the divertor will be provided with an emphasis on helium-cooled tungsten divertors.

1.2.   Fundamentals of Nuclear Fusion

Energy generation from both fission and fusion nuclear reactions occurs when there is a change in the total mass of particles before and after a reaction. This mass difference is converted into energy via Einstein's mass-energy equivalence

$$E = \Delta m c^2 \tag{1.1}$$

where E is energy, m is mass, and c is the speed of light. Even very small changes in the mass of nuclear fuel can therefore release a large amount of energy. To achieve a release of energy in a fusion reaction, smaller, less stable nuclei are joined together to form a more stable nucleus. The amount of energy released is directly related to the difference in nuclear binding energies of the initial and final components. The relationship between binding energy and mass number is shown in Figure 1.2.
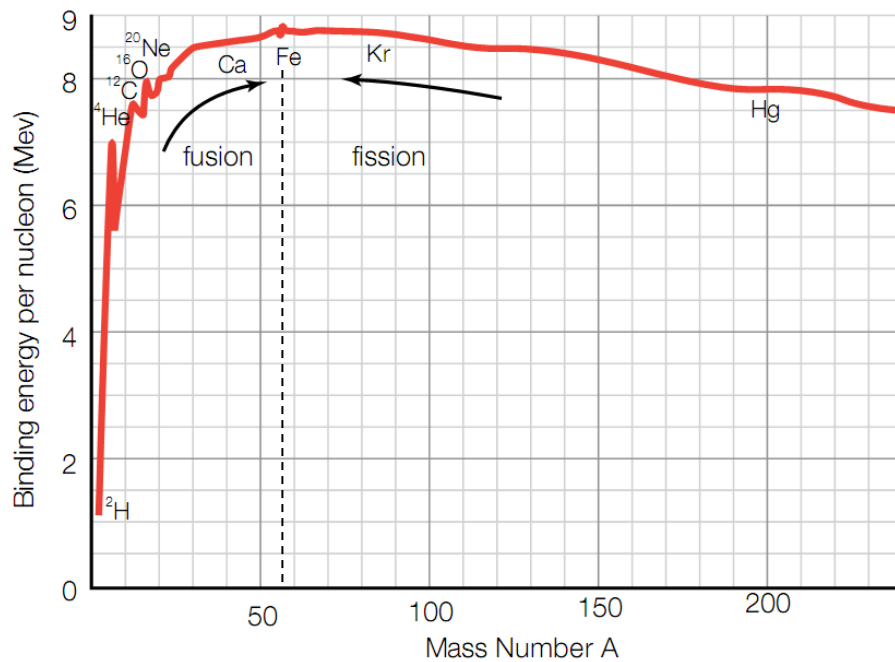
Figure 1.2. The relationship between binding energy and mass number [5].

The most promising fusion reactions occur when two very light nuclei (*e.g.*, hydrogen) "fuse" to produce a ^{4}He isotope and a large binding energy yield. In nuclear fission, heavy nuclei such as ^{235}U can be split into two lighter nuclei to release energy. However, the binding energy yield from fusion can be much larger than that of fission, especially with hydrogen-based fuels.

In a fusion device, positively charged atomic nuclei repel each other with a strong electrostatic force known as the Coulomb force. The Coulomb force is inversely proportional to the distance between two nuclei, and increases as the nuclei are brought closer together until a threshold called the Coulomb barrier is reached. In MFE reactors, this is achieved by confining fuel particles and injecting external energy which separates electrons and ions into a "fourth state of matter" known as plasma. Enough thermal energy must then be supplied such that the nuclei gain enough kinetic energy to collide and overcome the Coulomb barrier. The force then becomes attractive and binds the nuclei together, triggering a reaction upon contact. The lowest Coulomb barrier thresholds are associated with hydrogen isotopes, making them an attractive option for fusion fuel.

The amount of thermal energy required to initiate fusion depends on the specific type of reaction. Although several different reactions are possible, the probability of overcoming the Coulomb barrier is greater for exothermic reactions with two low atomic number reactants and two or more products. In particular, the fusion of deuterium and tritium (D-T) is favorable for both MFE and IFE reactors, and yields a 14.1 MeV neutron and 3.5 MeV helium ion (*i.e.*, "ash" or α-particle)

$$_1^2\text{D} + _1^3\text{T} \rightarrow _2^4\text{He} + _0^1\text{n} + 17.6\,\text{MeV} \tag{1.2}$$

The effectiveness of a fusion fuel is characterized by its reaction probability, or reactivity $<\sigma v>$. Figure 1.3 shows reactivity as a function of temperature for several reactions including D-T, deuterium-deuterium (D-D), and deuterium-helium-3 $(\text{D} - ^3\text{He})$. The D-T reaction has the largest reactivity for temperatures below 400 keV. At $10 - 20$ keV, for instance, it is 100 times larger than that of any other reaction.
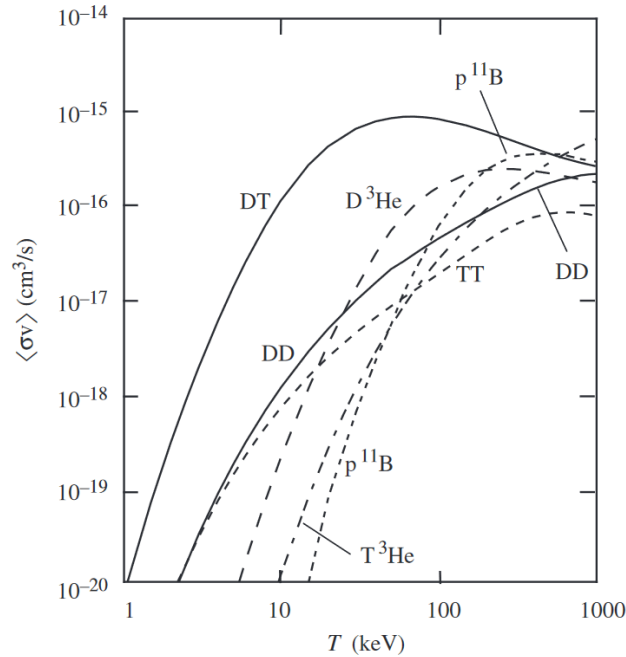
Figure 1.3. Reactivity *vs*. temperature for several fusion reactions [6].

The maximum reactivity for the D-T reaction occurs at a relatively modest temperature of 64 keV, which is favorable for producing a net energy gain [6]. Most of the generated energy is carried by neutrons that can escape magnetic confinement fields and transfer kinetic energy to surrounding structures in the form of heat. This thermal energy can then be extracted by a power conversion cycle to produce electricity.

A major advantage of fusion power is its large energy density. One kilogram of D-T fuel can provide as much energy as 10^7 kg fossil fuel [7]. Deuterium can be produced from ordinary water by mature technologies such as distillation or electrolysis, and since most of the Earth is comprised of water, the fuel is abundant. On the other hand, there is little, if any naturally occurring tritium due to its short half-life. Tritium can, however, be "bred" in a fusion reactor when the neutrons produced in the D-T reaction interact with a lithium isotope, namely $_3^6Li$ and $_3^7Li$. Natural lithium reserves are estimated to be

6

approximately 39 million tons in ore deposits and 276 billion tons in seawater, which suggests that fusion fuel resources can last for millions of years, assuming technologies for lithium extraction from seawater become more economically competitive [8, 9].

1.3.   Magnetic Confinement Fusion Energy

Nuclear fusion is the process that powers stars such as our Sun. Within the Sun's core, massive gravitational forces confine hydrogen into a highly dense plasma at temperatures of 10^7 K, resulting in a chain of proton-proton reactions with a yield of approximately 26.2 MeV [10]. However, without the mass required to sustain a large gravitational field or materials that can withstand such extreme plasma temperatures, terrestrial fusion must be controlled by other means, such as magnetic confinement. The most feasible magnetic approach involves confining plasma with low particle densities at the expense of high temperature requirements and long confinement times.

There are two main types of MFE reactors: stellarators and tokamaks (Figure 1.4). Both use multiple magnetic fields to confine plasma that moves around a torus. The stellarator concept was first developed by Lyman Spitzer in 1958 at what would later become the Princeton Plasma Physics Laboratory [11]. Unlike tokamaks, stellarators have an asymmetric magnetic field and utilize only one set of modular coils with a complex geometry, and are therefore difficult to manufacture. Stellarators were popular for two decades before interest largely shifted to improved tokamak designs with performance superior to stellarators. More recently, stellarators have garnered renewed interest and a number of new experimental devices, such as the German Wendelstein 7-X, have been

built. However, tokamaks remain more highly developed and future electricity producing

reactors such as DEMO will most likely be advanced tokamak machines.
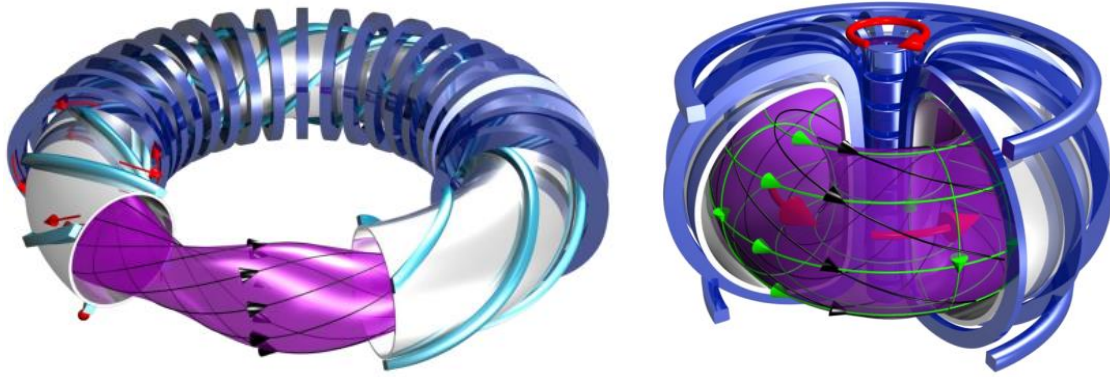
Figure 1.4. Rendering of a stellarator (left) and tokamak (right) design [12].

The tokamak concept was invented by Igor Tamm and Andrei Sakharov in 1950 at

the Kurchatov Institute in the former Soviet Union [13]. In the subsequent decades, the

concept was refined and improved through many international collaborations, which

helped establish tokamaks as a promising candidate for fusion power production.

Tokamaks feature a simple torus geometry with an axisymmetric cross-section that

improves confinement time and simplifies manufacturing. A combination of toroidal and

poloidal magnetic fields confines the plasma in the horizontal and vertical directions such

that charged particles move along field lines in a helical shape, and avoid direct contact

with the surrounding vessel walls. The poloidal field also induces an electric current within

the plasma itself. The current travels through the plasma and increases collisions between

electrons and ions to create heat. This phenomenon is known as ohmic heating and reaches

a threshold as the plasma temperature rises. The remaining thermal energy required to

sustain fusion reactions is provided by radio frequency (RF) heating and neutral beam

injection. With RF heating, external coils supply high-frequency waves at several different plasma resonant frequencies to increase temperature. Neutral beam injection involves discharging neutral atoms into the plasma at high velocities, where all of the kinetic energy is transferred to heat as the atoms are decelerated by plasma. All three methods will be used simultaneously to maintain the conditions required for "ignition" where fusion reactions can occur perpetually. Figure 1.5 shows an example of an advanced experimental tokamak called ITER, which is designed to demonstrate a ten-fold energy gain and provide the technological insight required to develop DEMO and a commercial fusion power plant.
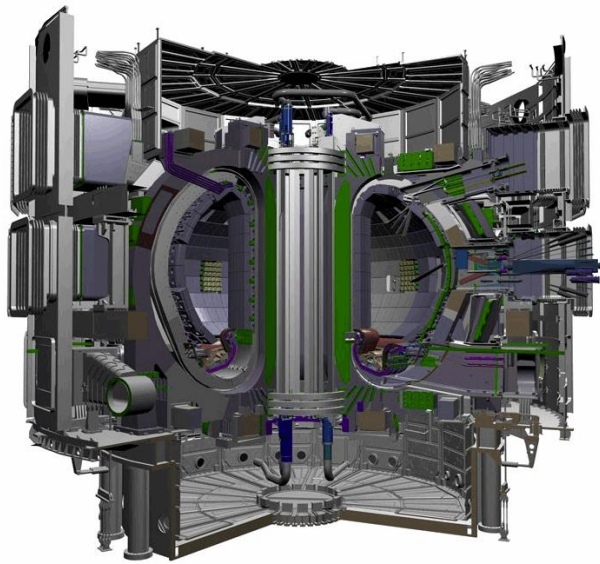
Figure 1.5. Rendering of ITER, currently under construction in France [14].

1.4. Divertors and Plasma Facing Components

The intense plasma temperatures and neutron fluences in a tokamak necessitate the use of robust PFCs. Most modern tokamaks contain two types of PFCs: the first wall and the divertor. The first wall and attached "blanket" must transfer the thermal energy from

the 14.1 MeV neutrons to a coolant that will ultimately drive turbines in a conventional power conversion cycle to generate electricity. These energetic neutrons will also be used to breed tritium by reacting with a coolant that contains lithium. Magnetic confinement prevents direct contact between the plasma and the first wall resulting in relatively modest thermal loads on the large wall surface area. The average neutron wall loads for ITER and DEMO, for example, are on the order of 0.5 MW/m^2 and 1 MW/m^2, respectively [15, 16]. This allows for simpler cooling designs, where a fluid such as helium or lead-lithium (PbLi) may be used effectively without additional heat transfer enhancement techniques.

The divertor is another important PFC that removes helium "ash" products, eroded wall particles, and unburned fuel from the plasma in order to prolong the fusion reaction and maintain high plasma temperatures. The ITER and DEMO reactors will utilize a divertor comprised of 54 and 48 identical "cassettes" that contain vacuum pumps and actively cooled target plates (Figure 1.6). Approximately 20% of the thermal energy from the fusion reaction must be absorbed by the relatively small divertor surface area, which will erode the plasma facing materials over time.

Figure 1.6. The ITER divertor (left) and a single divertor cassette (right) [14].

The divertor cassettes must be replaced periodically to avoid excessive damage and minimize potential contamination of the target plates from tritium retention. A modular design is therefore used to enable remote replacement of individual cassettes over the lifetime of a reactor.

Most tokamaks have a single-null divertor configuration (Figure 1.7) where magnetic fields are used to alter the outer edge of the plasma, creating a singularity called the X-point. This point defines two new regions: the scrape-off layer (SOL) and the "private flux" or "private plasma" zone [17]. The SOL is located immediately outside of the last closed flux surface (LCFS), or separatrix, and directly intersects the divertor. Charged particles in the SOL follow open magnetic field lines until they impinge on the divertor target plates. Lower energy particles scatter into the relatively cool private plasma, where they are removed by vacuum pumps. Higher energy particles transfer kinetic energy to the divertor target plates, resulting in extremely high steady-state heat fluxes. This thermal energy must be removed by a coolant and incorporated into the main power conversion cycle to improve the overall system efficiency and balance of plant.
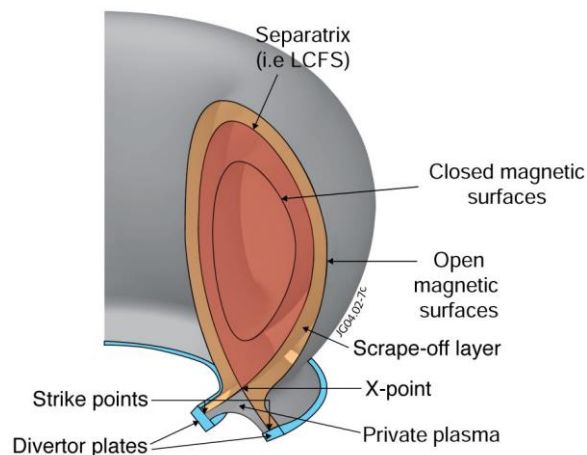
Figure 1.7. Illustration of a single-null divertor configuration [18].

The divertor target plates therefore face significantly higher thermal loads than the first wall. The design limits for DEMO are typically considered to be $10\,\mathrm{MW/m^2}$ at steady-state and $15 - 20\,\mathrm{MW/m^2}$ for short transient events [16, 19]. Several alternative divertor configurations such as the Super-X and Snowflake divertors have been proposed to reduce the high heat fluxes expected during continuous operation. The Super-X configuration involves extending the distance of one target plate to increase the major radius of the X-point and reduce heat flux [20]. The Snowflake divertor utilizes poloidal field coils situated outside of the toroidal coils to create a second-order null with a wide, hexagonal separatrix that spreads the heat flux into several branches and increases radiative cooling [21]. Although both concepts are promising, major challenges remain before they can be widely adopted in tokamak reactors. It is unclear, for example, how a more complex SOL will affect the plasma physics and stability. Significant changes in coil designs and component integration are also required to accommodate these advanced concepts. Furthermore, the performance of these concepts must be experimentally characterized under a variety of conditions including steady-state, transient, and short un-controlled disruption events. For these reasons, most divertor research has been based on the single-null configuration, with an emphasis on heat removal and materials development.

The number of materials suitable for a divertor target plate is severely limited. Solid materials must be able to survive extremely high temperatures and neutron irradiation for long periods of time without significant physical or chemical erosion (*i.e.*, sputtering). They must also have good thermal conductivity and low tritium retention rates. These criteria have restricted the selection of divertor PFC materials to two major candidates: carbon fiber composites (CFC) and tungsten. Modern divertors were largely based on

CFCs due to their favorable thermal shock resistance, plasma compatibility, and inability to melt. However, CFCs exhibit high tritium retention rates and excessive erosion that shortens operating times and raises concerns about radioactivity. France, for example, has imposed a maximum tritium limit of 700 g in ITER to ensure safe operation [22]. Although the ITER divertor was originally intended to be built with both CFCs and tungsten, recent experiments performed in the Joint European Torus have shown that tritium retention rates in full carbon PFCs are 10 times higher compared to full tungsten PFCs. Although CFCs offer many advantages, minimizing tritium retention rates has become critical, especially as heat fluxes and neutron fluences continue to increase in new MFE reactor concepts. Tungsten has therefore emerged as a more viable PFC material.

Tungsten has several advantages for fusion applications compared to other candidate materials such as beryllium, CFCs, or molybdenum. First, it has significantly lower sputtering rates for the ions present in a plasma, including tritium, which extends the reactor operating time and reduces the number of replacement intervals [23]. It also has a high melting point, high strength and good thermal conductivity, which allows for better thermal performance, even with large heat fluxes. Finally, it has a low activation and coefficient of thermal expansion (CTE). Unfortunately, tungsten loses ductility at relatively low temperatures, and neutron irradiation may cause transmutation and material swelling [24]. Exposure to He ions may also result in significant near-surface morphology changes such as bubble growth, pitting, and tendril (*i.e.*, "fuzz") formation [25, 26]. Despite its drawbacks, tungsten has emerged as a primary choice for PFC materials in advanced divertor designs.

The divertor coolant criteria for DEMO and future commercial fusion reactors differ significantly from those of ITER. Specifically, high coolant outlet temperatures are needed because the reactor power conversion system must include both the blanket and divertor to reach maximum efficiency. Helium has been widely studied as a coolant for the blanket and divertor, and has several advantages over water [27]. Helium is chemically inert and has a lower neutron cross-section, making it less likely to react adversely with large neutron fluences. Furthermore, it has a good specific heat among gases and is compatible with other coolants in the blanket such as Li or Pb, which simplifies the reactor design. It is also very straightforward to separate tritium from He. Finally, it is a single phase coolant, which allows the temperature of refractory metal PFCs to be kept above the ductile-to-brittle transition temperature (DBTT) without the need to operate at excessively high pressures.

Over the past decade, numerous divertor cooling systems have been proposed for near-term and advanced tokamak conceptual studies. The two most pertinent studies are the EU Power Plant Conceptual Study and the ARIES Advanced Conservative Tokamak study [28, 29]. Nearly all of the divertor configurations in these studies involve He-cooled W- or W-alloy target plates that are divided into a large number of individual "finger-type" modules as opposed to a large plate. This approach reduces thermal stresses on the PFCs and allows for parallel flow paths that reduce coolant pumping power. Although several cooling mechanisms have been proposed, the most promising divertor designs involve arrays of rectangular or circular impinging jets due to the high heat transfer coefficients (HTC) that can be produced from intense turbulent mixing. This research will focus on the

14

thermal-hydraulic performance of a specific finger-type divertor called the He-cooled modular divertor with multiple jets (HEMJ), which is the leading candidate for DEMO.

Although He-cooled divertors have been studied by multiple groups in the past, nearly all of the work has been based on numerical simulations. Recently, several different He-cooled divertor concepts have been experimentally evaluated using dynamic similarity, and the results were extrapolated to determine the thermal-hydraulic performance at fully prototypical conditions [30-32]. The extrapolated results are derived from correlations based on experimental data with different coolants, and can be incorporated into system codes to examine tradeoffs and determine operating conditions for future fusion reactors. However, these data were obtained under conditions that differ significantly from that of an actual reactor. Moreover, the effect of varying geometric parameters such as jet diameter has not been studied experimentally. Additional experiments are therefore required to improve confidence in the extrapolation to fully prototypical conditions and evaluate the effect of geometric changes on the divertor performance.

To this end, this work focuses on experimentally evaluating the thermal performance of the HEMJ design at nearly prototypical condition and characterizing the effects of geometric changes using experiments and numerical simulations. Specifically, a closed helium loop is used to conduct experiments on a single divertor module that is geometrically similar to the HEMJ, and the effect of varying the jet cartridge-to-cooled surface separation distance is investigated. Temperatures measured using thermocouples embedded within the divertor module are used to estimate the cooled surface temperature and determine Nusselt number correlations over a range of Reynolds numbers. The

15

measured pressure drop across the module is used to develop loss coefficient correlations that can also be used to predict pumping power requirements at prototypical conditions.

Numerical simulations are performed using the commercially available software package ANSYS® Workbench™ 17.0 to develop a computational fluid dynamics (CFD) and finite element method (FEM) model with one-way coupling. The model is validated against experimental data and used to predict the thermal performance of the divertor under fully prototypical conditions. The model is used to perform a parametric study in which the jet arrays parameters (*i.e.*, jet diameter, separation distance, and jet pitch) are varied to determine an optimal design that may simplify manufacturing and reduce costs. Finally, the thermal-hydraulic performance of the improved design is experimentally evaluated and compared with the performance of the HEMJ divertor.

The remainder of this thesis is organized as follows: Chapter 2 consists of a literature review of jet impingement heat transfer, modular helium-cooled divertor designs, and previous experimental and numerical studies of finger-type divertors. Chapter 3 presents experimental results of the HEMJ-like divertor obtained at nearly prototypical conditions. This includes results obtained at higher coolant inlet temperatures and incident heat fluxes than previously reported. The effect of varying the separation distance on the thermal-hydraulic performance is also reported. Chapter 4 describes the development of a one-way coupled CFD/FEM model of the divertor module used in the experiments, and the results obtained at fully prototypical conditions. Chapter 5 details a parametric optimization study of various jet arrays performed based on the numerical model developed in Chapter 4. Finally, Chapter 6 summarizes the conclusions of this research and makes recommendations for future work.

CHAPTER 2: LITERATURE REVIEW

A robust and reliable cooling system design for the target plates of the divertor is an important aspect of MFE reactor engineering. However, advanced divertor cooling concepts are needed to address the technological challenges associated with the extreme conditions within a commercial fusion reactor. To that end, experimental and numerical studies have been performed by various research groups over the past decade to improve the knowledge of divertor performance for both near-term and advanced reactors. The majority of current advanced divertor designs are based on the modular He-cooled tungsten divertor concept with jet impingement cooling. This section summarizes the underlying physics and previous research related to these promising He-cooled divertor designs.

Among the several different modular He-cooled divertor concepts, notable progress has been made on three particular designs: the HEMJ, the He-cooled modular divertor with integrated pin array (HEMP), and the He-cooled flat plate divertor (HCFP). As part of the ARIES study, an "integrated plate-type" divertor that combines the HEMJ and HCFP concepts was proposed to reduce the number of overall modules while maintaining good thermal performance. Limited research was also done on an earlier candidate called the T-Tube divertor, which is currently under investigation to cool target materials in a new experimental linear plasma device at Oak Ridge National Laboratory (ORNL).

Given that all of these divertor designs rely on turbulent jet impingement cooling, it is important to understand the fundamental fluid mechanics and heat transfer aspects of this type of cooling. This chapter therefore first presents a brief overview of the governing conservation laws for the fluid dynamics, heat transfer, and turbulence models commonly

used by commercially available CFD software packages used here to study divertors. Next, the fundamental characteristics of jet-impingement heat transfer will be discussed and previous studies of divertor-relevant geometries will be reviewed. The last section describes prior experimental and numerical investigations of the performance of various divertor designs.

2.1   Turbulent Flows and Heat Transfer

2.1.1   Conservation Laws

The flow of a Newtonian fluid in a continuum is described by three governing equations: the conservation of mass (continuity), conservation of momentum, and conservation of energy. The continuity equation is shown below using Cartesian index notation

$$\frac{\partial \rho}{\partial t} + \frac{\partial}{\partial x_i}(\rho u_i) = 0 \tag{2.1}$$

where ρ is the fluid density and u_i is the velocity component in the x_i direction. Conservation of momentum is described by the Navier-Stokes equations (Newton's second law)

$$\frac{\partial (\rho u_i)}{\partial t} + \frac{\partial}{\partial x_i}(\rho u_i u_j) = -\frac{\partial p}{\partial x_i} + \frac{\partial}{\partial x_j}\left[2\mu e_{ij} - \frac{2}{3}\mu(\nabla \cdot \mathbf{u})\delta_{ij} \right] + \rho g_i \tag{2.2}$$

where p is the fluid pressure, μ is the fluid dynamic viscosity, e_{ij} is the strain rate tensor, δ_{ij} is the Kronecker delta, and ρg_i is the gravitational body force. The strain rate tensor is defined as

$$e_{ij} = \frac{1}{2}\left(\frac{\partial u_i}{\partial x_j} + \frac{\partial u_j}{\partial x_i} \right) \tag{2.3}$$

which accounts for additional fluid stresses caused by fluid motion. The left-hand side of Eq. 2.2 represents the convective acceleration of a fluid element due to inertial forces, while the right-hand side describes contributions to momentum change due to pressure, viscous, and body forces. The conservation of energy equation (first law of thermodynamics) is given by

$$\frac{\partial(\rho E)}{\partial t} + \frac{\partial}{\partial x_i}(\rho u_i E) = \frac{\partial}{\partial x_j}(\tau_{ij} u_i) - \frac{\partial q_i}{\partial x_i} + \rho g_i u_i \tag{2.4}$$

where E is the total energy per unit mass, τ_{ij} is the stress tensor, and q_i is the heat flux vector. Here, E is defined as

$$E = h - \frac{p}{\rho} + \frac{u^2}{2} \tag{2.5}$$

where h is the specific fluid enthalpy. For a Newtonian fluid, the viscous stress tensor is

$$\tau_{ij} = -p\delta_{ij} + 2\mu e_{ij} - \frac{2}{3}\mu(\nabla \cdot \mathbf{u})\delta_{ij} \tag{2.6}$$

The heat flux is described by Fourier's law

$$q_i = -k\frac{\partial T}{\partial x_i} \tag{2.7}$$

where k is the thermal conductivity and T is the temperature.

Many engineering applications involve non-isothermal turbulent flows, which are characterized by random or stochastic fluctuating quantities. The Reynolds-Averaged Navier-Stokes (RANS) equations are therefore often used to obtain approximate time-averaged solutions to the Navier-Stokes equations

$$\frac{\partial \rho}{\partial t} + \frac{\partial}{\partial x_i}(\rho \overline{u_i}) = 0 \tag{2.8}$$

$$\frac{\partial \left(\rho \overline{u_i}\right)}{\partial t} + \frac{\partial}{\partial x_i}\left(\rho \overline{u_i u_j}\right) = -\frac{\partial \overline{p}}{\partial x_i} + \frac{\partial}{\partial x_i}\left[\mu\left(\frac{\partial \overline{u_i}}{\partial x_j} + \frac{\partial \overline{u_j}}{\partial x_i} - \frac{2}{3}\delta_{ij}\frac{\partial \overline{u_k}}{\partial x_k}\right)\right] + \frac{\partial}{\partial x_j}\left(-\rho \overline{u_i' u_j'}\right) \tag{2.9}$$

where $\overline{u_i}$ is the time-averaged component of u_i (based on the Reynolds decomposition of the Navier-Stokes equations) and $-\rho \overline{u_i' u_j'}$ is the Reynolds stress tensor. The Reynolds stress tensor is a second-order, symmetric tensor that accounts for turbulent fluctuations and introduces six new unknowns. A total of ten unknowns (the pressure, the three velocity components, and the six Reynolds stresses) are therefore required to solve, or "close" the problem. Numerous "turbulence closure" models have been developed in the past century to model the Reynolds stress tensor for different types of flows. This work will focus on the RANS turbulence models implemented in the commercial software package ANSYS® Fluent®, which was used for the numerical simulations in this thesis.

2.1.2   *Turbulence Models and Heat Transfer*

The high temperatures and pressures within a divertor system make experimental characterization of turbulent flow impractical in many cases. As a result, several groups have used commercial CFD software packages such as ANSYS® CFX® or Fluent® to

model fluid flow and heat transfer within various divertor designs. This section focuses on the six different turbulence models available in ANSYS® Fluent®, including the Spalart-Allmaras (S-A), k-ε models, and k-ω models.

All of the models above relate the Reynolds stress tensor to the mean velocity gradients based on the eddy viscosity concept introduced by Boussinesq:

$$-\rho \overline{u_i' u_j'} = \mu_t \left(\frac{\partial \overline{u_i}}{\partial x_j} + \frac{\partial \overline{u_j}}{\partial x_i} \right) - \frac{2}{3} \left(\rho k + \mu_t \frac{\partial \overline{u_k}}{\partial x_k} \right) \delta_{ij} \tag{2.10}$$

where μ_t is the turbulent, or Boussinesq eddy, viscosity and k is the turbulence kinetic energy [33]. In this section, k is mathematically defined as

$$k = \frac{1}{2} \overline{u_i' u_i'} \tag{2.11}$$

and represents the kinetic energy per unit mass of the fluctuations u_i'. This approach has the advantage of a relatively low computational cost associated with evaluating the Boussinesq eddy viscosity and kinetic energy. One caveat is that μ_t is assumed to be an isotropic scalar quantity, which is not strictly true. However, this assumption is reasonable for shear flows where the turbulent shear stress is only significant in one direction, which applies to many flows including wall boundary layers and jets [33].

The Spalart-Allmaras model is a one-equation model that neglects the turbulence kinetic energy k and closes the RANS equations by solving the following transport equation for a modified turbulent kinematic viscosity $\tilde{v}$:

$$\frac{\partial (\rho \tilde{v})}{\partial t} + \frac{\partial}{\partial x_i} \left(\rho \tilde{v} u_i \right) = G_v + \frac{\partial}{\sigma_{\tilde{v}}} \left[\frac{\partial}{\partial x_j} \left\{ \left(\mu + \rho \tilde{v} \right) \frac{\partial \tilde{v}}{\partial x_j} \right\} + C_{b2} \rho \left(\frac{\partial \tilde{v}}{\partial x_j} \right)^2 \right] - Y_v + S_{\tilde{v}} \tag{2.12}$$

21

where G_v is the production of kinematic viscosity, Y_v is the destruction of kinematic viscosity in the near-wall region, $S_{\tilde{v}}$ is a source term, and $\sigma_{\tilde{v}}$ and C_{b2} are constants. The Boussinesq eddy viscosity can then be related to the transported variable $\tilde{v}$ by

$$\mu_t = \rho \tilde{v} f_{v1} , \quad f_{v1} = \frac{\left(\tilde{v}/v\right)^3}{\left(\tilde{v}/v\right)^3 + C_{v1}^3} \tag{2.13}$$

where C_{v1} is another constant. A total of twelve empirical constants deduced from experimental data are used to compute the terms on the right-hand side of Eq. 2.12 and hence, μ_t and the Reynolds stress tensor to close the problem.

The S-A model was designed for wall-bounded flows with boundary layers subject to adverse pressure gradients. Although a fine, or spatially well-resolved, mesh near the wall was originally required to properly resolve the boundary layer, ANSYS® Fluent® uses Enhanced Wall Treatment (EWT) instead to decouple the S-A model from these near-wall spatial resolution requirements. The low computational cost associated with the one-equation approach is a key advantage of the S-A model, but it is not a very accurate model for turbulent shear flows.

Two-equation models are a more complex class of models that use two additional transport equations to compute μ_t. In addition to k, two-equation models also account for the turbulent kinetic energy dissipation rate, ε, which represents the rate at which k is converted into thermal kinetic energy due to viscous stresses. Most industrial applications rely on one of the three types of what are known as k-ε models: standard k-ε (SKE), renormalization group k-ε (RNGKE), or realizable k-ε (RKE). These models determine a turbulent length scale and a time scale by solving transport equations for k and ε [33]. The

transcription equation for k was derived from the Navier-Stokes equations while empirical results were used to develop the transport equation for ε. The transport equations or the SKE model are

$$\frac{\partial(\rho k)}{\partial t}+\frac{\partial}{\partial x_i}(\rho k u_i)=\frac{\partial}{\partial x_j}\left[\left(\mu+\frac{\mu_t}{\sigma_k}\right)\frac{\partial k}{\partial x_j}\right]+G_k+G_b-\rho\varepsilon-Y_M+S_k \qquad (2.14)$$

$$\frac{\partial(\rho\varepsilon)}{\partial t}+\frac{\partial}{\partial x_i}(\rho\varepsilon u_i)=\frac{\partial}{\partial x_j}\left[\left(\mu+\frac{\mu_t}{\sigma_\varepsilon}\right)\frac{\partial\varepsilon}{\partial x_j}\right]+C_{1\varepsilon}\frac{\varepsilon}{k}(G_k+C_{3\varepsilon}G_b)-C_{2\varepsilon}\rho\frac{\varepsilon^2}{k}+S_\varepsilon \qquad (2.15)$$

where G_k is the production of turbulence kinetic energy due to mean velocity gradients, G_b is the production of k due to buoyancy, Y_M is the contribution of compressible turbulence to ε, $C_{1\varepsilon}$, $C_{2\varepsilon}$, $C_{3\varepsilon}$ are constants, and σ_k and σ_ε are the turbulent Prandtl numbers for k and ε, respectively. The turbulence dynamic viscosity can then be related to k and ε by

$$\mu_t=\rho C_\mu\frac{k^2}{\varepsilon} \qquad (2.16)$$

where C_μ is a value obtained from experiments and depends on the turbulence model. For the simulations performed in this work, C_μ was assumed to be 0.09 based on the results of Launder and Spalding [34]. This definition is also valid for the RNGKE model (at high flow rates) and the RKE model [33].

The RNGKE and RKE models are variations of the SKE model that were developed to provide more accurate predictions under certain conditions. For rapidly strained and rotating flows, the RNGKE model improves accuracy by including an additional term in the ε equation. In contrast, the RKE model involves a variable C_μ that depends on mean

strain and rotation rates, and a modified ε transport equation. The RKE model has similar applications as RNGKE, but may converge more easily.

Another type of two-equation models are the k-ω models, which solve transport equations for k and the specific dissipation rate ω (*i.e.*, the ratio of ε to k). These include the standard k-ω (SKO) and shear-stress transport (SST) k-ω models. The transport equations for the SKO model are given by

$$\frac{\partial(\rho k)}{\partial t} + \frac{\partial}{\partial x_i}(\rho k u_i) = \frac{\partial}{\partial x_j}\left(\Gamma_k \frac{\partial k}{\partial x_j}\right) + G_k - Y_k + S_k \tag{2.17}$$

$$\frac{\partial(\rho \omega)}{\partial t} + \frac{\partial}{\partial x_i}(\rho \omega u_i) = \frac{\partial}{\partial x_j}\left(\Gamma_\omega \frac{\partial \omega}{\partial x_j}\right) + G_\omega - Y_\omega + S_\omega \tag{2.18}$$

where G_ω is the production of ω, Γ_k and Γ_ω is the effective diffusivity of k and ω, and Y_k and Y_ω is the dissipation of k and ω, respectively. The turbulent viscosity is then given by

$$\mu_t = \alpha^* \rho \frac{k}{\omega} \tag{2.19}$$

where α^* is a damping coefficient equal to 1 for high flow rates. The SKO model accounts for compressibility and shear effects, but is very sensitive to k and ω values in the freestream. The SST model combines the advantages of the SKE and SKO models by blending the accurate near-wall k-ω formulations with the free-stream independent k-ε model in the far-field, but does not include compressibility effects.

The last RANS model available in ANSYS® Fluent® is the Reynolds Stress model, which does not rely on the assumption that μ_t is isotropic. As a result, it is considered more accurate for flows with buoyancy and significant strain rates, but it is also more

computationally expensive and has not been used to date for divertor simulations. The transport equations and additional details are therefore excluded for brevity.

In addition to turbulent flow, modeling of thermal energy transport within both solids and fluids is critical to predicting the thermal performance of divertors. In ANSYS® Fluent®, turbulent heat transport for a fluid is modeled using the Reynolds' analogy, where the energy equation becomes

$$\frac{\partial}{\partial t}(\rho E) + \frac{\partial}{\partial x_i}\left[u_i(\rho E + p)\right] = \frac{\partial}{\partial x_j}\left(k_{eff}\frac{\partial T}{\partial x_j} + u_i \tau_{ij}^{eff}\right) + S_h \tag{2.20}$$

Here, $k_{eff} = k_f + k_t$ is the effective thermal conductivity of the fluid, k_f is the thermal conductivity of the fluid, k_t is the turbulent thermal conductivity, τ_{ij}^{eff} is the stress tensor based on μ_{eff} (discussed below), and S_h is a source term. The first two terms on the right-hand side represent energy transfer due to conduction and viscous dissipation, respectively. With the exception of RNGKE, all of the RANS models in ANSYS® Fluent®, define the turbulent thermal conductivity as

$$k_t = \frac{c_p \mu_t}{Pr_t} \tag{2.21}$$

where c_p is the constant-pressure specific heat of the fluid, and Pr_t is the turbulent Prandtl number. For flows where convective heat transfer is significantly greater than conduction, Pr_t has been shown to be approximately 0.85 [35]. The RNGKE model accounts instead for variations in Pr_t by defining the thermal conductivity as

$$k_t = \alpha c_p \mu_{eff} \tag{2.22}$$

25

where the effective viscosity μ_{eff} is the sum of the laminar and turbulent viscosities, and α is obtained by solving

$$\left| \frac{\alpha - 1.3929}{Pr^{-1} - 1.3929} \right|^{0.6321} \left| \frac{\alpha + 2.3929}{Pr^{-1} + 2.3929} \right|^{0.3679} = \frac{\mu}{\mu_{eff}} \tag{2.23}$$

Finally, heat transfer within a solid material is governed by the following energy equation

$$\frac{\partial}{\partial t}(\rho_s h_s) = \nabla \cdot (k_s \nabla T) + S_h \tag{2.24}$$

where ρ_s, h_s, and k_s are the density, enthalpy, and thermal conductivity of the solid, respectively. All solids modeled in this work are assumed to have an isotropic thermal conductivity.

2.1.3 The Empirical Approach

Divertor target plates require active cooling, or forced convection, to withstand the high heat fluxes supplied to the plasma-facing surfaces. The effectiveness of a convective heat transfer system is governed by Newton's Law of Cooling

$$q'' = h(T_c - T_\infty) \tag{2.25}$$

where q'' is the heat flux from the solid to the fluid, h is the convective heat transfer coefficient (HTC), T_c is the temperature of the solid boundary, and T_∞ is the temperature of the bulk fluid. Any study of convection ultimately requires characterizing h.

Although the HTC is influenced by several factors including the boundary layer conditions and surface geometry, it can be determined or estimated with two main

approaches: theoretical and empirical. The theoretical approach involves deriving analytical expressions of the local convection coefficient through dimensional analysis, exact analysis of the boundary layer, or analogies between momentum and energy transfer. However, this is impractical for a complex geometry such as the HEMJ, which has different surface curvatures and involves turbulent flow. The empirical approach is therefore used in this work, which involves performing experiments under controlled conditions and correlating the data in terms of dimensionless parameters. Empirical correlations are often developed for an average convection coefficient $\bar{h}$, based on the entire surface area of the experimental setup.

The average heat transfer coefficient is typically given in terms of the nondimensional average Nusselt number

$$\overline{Nu} = \frac{\bar{h}D}{k_f} \tag{2.26}$$

where D is a length scale that characterizes the geometry and k_f is the thermal conductivity of the fluid. The Nusselt number represents the ratio of thermal energy transferred across a solid/fluid interface by convection (*i.e.*, both advection and diffusion) to that of conduction, and depends on geometry, flow velocity, and flow properties. However, for forced convection with negligible viscous dissipation (*i.e.*, moderate velocity gradients), the average Nusselt number depends only on the Reynolds number *Re* and the Prandtl number *Pr* for a given geometry. The Reynolds number may be expressed in terms of the flow velocity as

$$Re = \frac{\rho VD}{\mu} \tag{2.27}$$

where V is a velocity scale that represents the flow. The fluid mass flow rate can be non-dimensionalized into the Reynolds number, which represents the ratio of inertial forces to viscous forces. The Prandtl number is given as

$$Pr = \frac{\mu c_p}{k_f} \qquad (2.28)$$

which represents the ratio of momentum (*i.e.*, viscous) diffusivity to thermal diffusivity of a fluid. Experimentally estimated Nusselt numbers for the turbulent flow of a given fluid, and hence Prandtl number, often show a power law dependence on the Reynolds number. Generalized Nusselt number correlations for different fluids are therefore often assumed to be of the form

$$\overline{Nu} = CRe^m Pr^n \qquad (2.29)$$

where C, m, and n are constants that are independent of the fluid choice and only depend on the nature of the surface geometry and the flow regime.

The Biot number Bi is another dimensionless parameter that can characterize the relative importance of convection to conduction

$$Bi = \frac{hL_c}{k_s} \qquad (2.30)$$

where L_c is a characteristic length typically defined as the ratio of the solid's volume to surface area and k_s is the thermal conductivity of the solid. Unlike Nu however, the Biot number represents the relative significance of temperature differences *within* a solid compared to the temperature differences created by convection. The Nusselt number is typically used to determine local and average HTCs, while the Biot number often serves as

a criterion to justify the assumption of a uniform temperature distribution within a solid with surface convection effects (*i.e.*, a "lumped body" approximation).

The pressure drop through a flow component is another important parameter that affects the overall performance of an system with internal forced convection. The pressure drop can be measured and expressed as the dimensionless loss coefficient

$$K_L = \frac{\Delta p}{\frac{1}{2}\rho V^2} \qquad (2.31)$$

For incompressible duct flow, the pressure drop can be used to estimate the power required to move the fluid (*e.g.*, by a pump or compressor). The thermal-hydraulic performance is therefore most favorable when $\overline{Nu}$ is maximized and K_L is minimized.

2.2   Jet Impingement Heat Transfer

As mentioned previously, many He-cooled divertor designs rely on jet impingement as a heat transfer enhancement technique. Jet-impingement cooling is a well-established method known for its high heat transfer coefficients, and is used in applications that include turbine blade cooling, glass annealing, and more recently, electronics cooling. Although many jet-impingement studies exist in the literature, the design of such systems is challenging since heat transfer characteristics are influenced by (among other factors) a large number of geometric factors such as jet diameter, hole pitch, and jet exit-to-impingement surface separation distance. In addition, there are few previous jet-impingement studies that are directly relevant to gas-cooled divertor geometries. The present review focuses on arrays of round impinging jets at small separation distances,

which are most relevant to the HEMJ divertor studied here. We start, however, with a review of the fluid mechanics and heat transfer phenomena relevant to basic jet-impingement systems.

2.2.1   Single Jet Impingement

The flow in a single jet is typically divided into three regions: the free jet, stagnation, and wall jet regions (Figure 2.1). A round or 2D jet exits from a nozzle of diameter *D* or rectangular slot of width *W*, respectively, and develops in the free jet region where the jet boundaries gradually broaden due to entrainment of the surrounding fluid. This entrainment of the surrounding fluid, which is usually at rest, leads to an increase in the jet diameter or width, and a decrease in the diameter or width of the potential core (*i.e.*, the region of uniform flow at the nozzle exit velocity) away from the nozzle. The length of the potential core is typically 4 to 7 nozzle diameters [36, 37]. Farther downstream in the developing zone, the potential core disappears and the maximum axial velocity begins to decay until the flow is fully developed. Once the jet is fully developed (but remains within the free jet region), the average velocity profile no longer changes with distance from the nozzle and can often be approximated as a Gaussian function. Within the stagnation region, the influence of the impingement plate becomes stronger, resulting in curved streamlines where the flow is decelerated axially and accelerated laterally. After striking and stagnating at the impingement surface, the flow then spreads parallel to the surface in the wall jet region, spreading and decelerating with increasing distance from the stagnation point, giving rise to a thin boundary layer. In this region, the outer edge of both

the wall jet and the boundary layer grow simultaneously until fully developed conditions are reached and the wall jet transitions from laminar to turbulent. Velocity profiles in this regime are characterized by zero velocity at the impingement and wall jet boundaries, with a maximum value near the wall that decreases as the flow spreads outward [38].
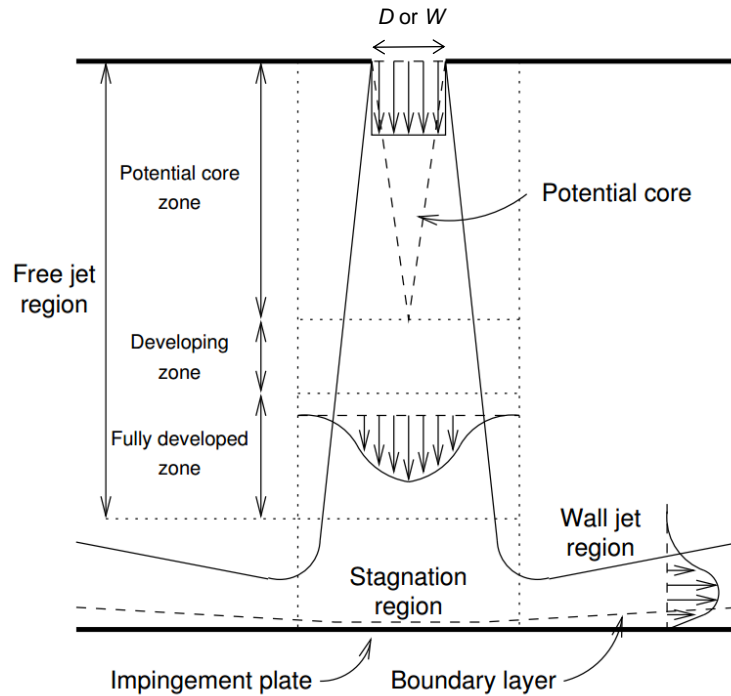
Figure 2.1. Flow characteristics for a single round or slot impinging jet [39].

2.2.2 Multiple Jet Impingement

Although multiple impinging jets have flow regions similar to those reported for single jets, jet arrays have two fundamentally different flow interactions that must also be considered. First, there is the possibility of interference between adjacent jets upstream of impingement. This type of interference is important for arrays with small jet-to-jet spacing and large jet-to-impingement surface spacing. Second, the collision of adjacent wall jets

31

may form recirculating flow regions known as "fountains" (Figure 2.2) that can significantly affect heat transfer rates. This fountain effect becomes increasingly important for closely spaced jets with large jet velocities at small separation distances. Both of these effects can be amplified if crossflow occurs between the jets after impingement.

Fountain flow
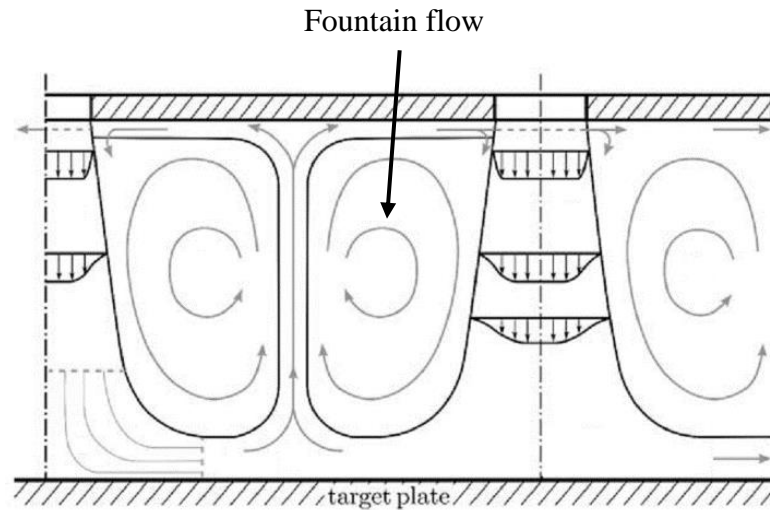
Figure 2.2. Flow regimes for an array of impinging jets [40]

The principal factors that influence heat transfer in single jet impingement systems also apply to multiple jet arrays, and typically include the nozzle shape, jet exit-to-impingement surface separation distance H, and the fluid mass flow rate $\dot{m}$. However, multiple jet arrays are more complex, and include additional factors such as the center-to-center jet spacing or pitch S, and the nozzle arrangement. The mass flow rate is typically given in terms of the Reynolds number Re, while the jet diameter is used to define a normalized separation distance H/D and pitch S/D. The thermal performance of jet impingement systems is described by the average Nusselt number $\overline{Nu}$, which generally increases with Re if all other parameters remain constant [41].

2.2.3 Effect of Jet-to-Surface Separation Distance

The effect of separation distance on thermal performance has been investigated in numerous jet impingement studies. Several studies suggest that the maximum local *Nu* occurs at $H/D = 1 – 3$ in jet arrays, compared to $H/D = 6 – 8$ for single jets [42-44]. Kercher and Tabakoff experimentally studied square arrays of impinging air jets for $H/D = 1 – 4.8$ and observed higher stagnation point *Nu* for $H/D = 2.7$ at any given *Re* [45]. Goldstein and Timmers used liquid crystals to visualize the heat transfer coefficient distribution of single and multiple jets impinging on a flat plate for $H/D = 2$ and 6 at $Re = 4 \times 10^4$ [46]. They found that the local Nusselt numbers produced from a hexagonal array of seven jets at *H/D* = 2 were approximately 26% higher on average compared with those at $H/D = 6$ [46]. Garimella and Schroeder studied confined impinging air jets for $0.5 \leq H/D \leq 4$ and reported greater local and average HTC at small *H/D*, which was attributed to an increased turbulence intensity due to mixing with the spent flow of neighboring jets [47]. This increase was more pronounced at higher *Re*, where additional flow interactions (*i.e.*, crossflow) shifted the maxima of local HTC distributions towards the central jet. Huber and Viskanta also used a liquid crystal technique to show that surface heat transfer rates in arrays with large separation distances may be degraded by adjacent jet interactions that entrain surrounding fluid prior to impingement and decrease the jet velocity, which is less likely to occur at small *H/D* [48]. As shown in Figure 2.3, Huber and Viskanta observed the greatest $\overline{Nu}$ for an array of round jets with $H/D = 1$ and jet-to-jet spacing $S/D = 4$. These studies suggest that maximum average heat transfer rates occur when $H/D \leq 3$ and this maximum value increases with *Re* [39, 41, 42].
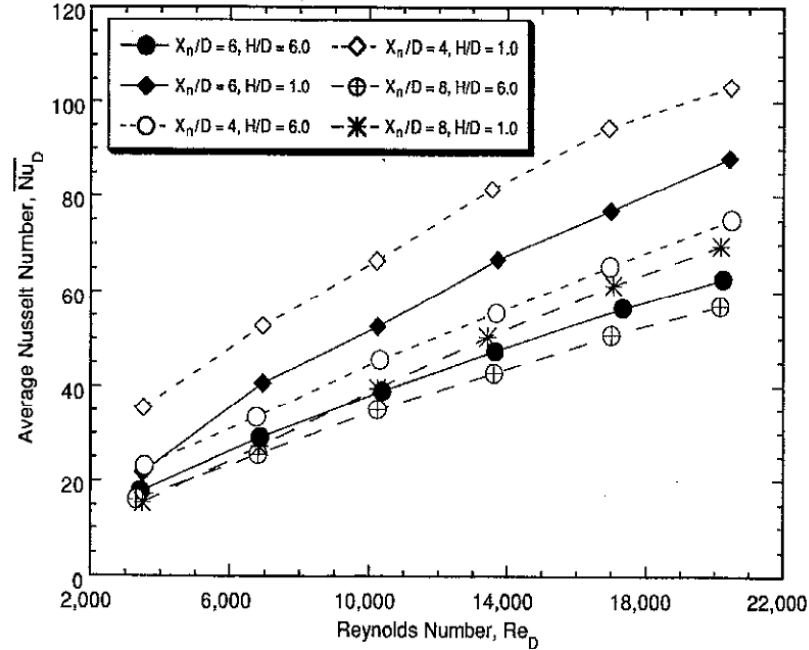
Figure 2.3. Comparison of average Nusselt numbers for S/D (*i.e.*, X_n/D) = 4, 6, and 8 at H/D = 1 and 6 [48].

2.2.4   Effect of Jet-to-Jet Spacing

The degree to which average *Nu* depend on *H* is also determined by the center-to-center hole spacing, or pitch *S*, which may vary along different directions depending upon the arrangement of the jet array. The highest average heat transfer rates have been reported for configurations with $S/D \leq 10$ [49]. For $S/D > 10$, the interaction between adjacent jets prior to impingement is negligible, and so the heat transfer characteristics for such configurations can be determined from single-jet impingement data. However, arrays of multiple interacting jets with $S/D \leq 10$ have better thermal performance than non-interacting jets, and a number of studies suggest that the best thermal performance is achieved at $3 \leq S/D \leq 6$ for a *Re* of $O(10^4)$ [39, 47, 50-52]. The influence of *S/D* on average heat transfer rates appears, however, to be minor compared with separation distance effects.

34

Attalla reported average *Nu* as great as ~170 for *S/D* = 6 and *Re* = 4.14×10^4 at separation distances of 2 ≤ *H/D* ≤ 4 for both square and hexagonal arrays [53]. San and Lai found a maximum stagnation point *Nu* ≈ 90 using a hexagonal array with *S/D* = 8, *H/D* = 2 at *Re* = 3×10^4 [54]. Saripalli visualized a pair of impinging round jets at *Re* = 2.38×10^4 and *H/D* = 4 and found no interaction between the jets at *S/D* = 12 [55].

Although a number of studies have proposed correlations for $\overline{Nu}$ in various jet array configurations [43, 45, 47-49, 56], it is unclear if these correlations are applicable to different geometries, given the large number of studies that suggest that jet-impingement cooling is a strong function of the flow geometry, including the geometry of the impingement surface. In most studies, the jet(s) impinge upon a flat surface and the wall jet is normal to the free jet. Studies of jet impingement on curved surfaces, whether experimental or numerical, are limited. The results of the few studies that exist on multiple jet impingement on concave surfaces suggest that the separation distance required for maximum heat transfer differs from that for a flat-plate configuration under otherwise identical conditions [57-59]. It is therefore unclear if these correlations, and the findings of previous studies of jet-impingement cooling, even at small separation distances, are relevant to the complicated geometry of the HEMJ divertor, which has an array of jets that issue from a convex surface and impinge upon a concave surface. The thermal-hydraulics of the specific HEMJ geometry should therefore be investigated experimentally and numerically.

2.3 Helium-Cooled Divertor Designs

Several modular helium-cooled divertor designs are discussed in this section. While certain designs have more favorable thermal-hydraulic performance than others, each design has specific advantages and drawbacks. It is important to note that helium-cooled divertors remain an active area of research and the actual divertor design for DEMO has not yet been finalized.

2.3.1 Helium-cooled Modular Divertor with Multiple Jets

One of the most-studied designs to date is the helium-cooled modular divertor with multiple jets (HEMJ), originally developed at the Karlsruhe Institute of Technology (KIT) in 2004 [60]. As shown in Figure 2.4, a single HEMJ module is comprised of a pure W tile, W-alloy endcap, and oxide dispersion-strengthened (ODS) Eurofer steel jets cartridge. The plasma-facing surface consists of a 5 mm thick hexagonal W tile with a width (between two parallel edges) of 18 mm. The tile is brazed to a 15 mm OD WL10 (99% W, 1.0% La_2O_3) endcap (*i.e.*, pressure boundary) with a thickness of 1 mm that restricts potential crack propagation to the interface. The endcap is also brazed to a conical ODS Eurofer steel sleeve with a copper(Cu)-based alloy to reduce the coefficient of thermal expansion (CTE) mismatch between WL10 and steel. Arrays of multiple finger modules are assembled on a steel manifold, and the ring serves as a transition piece between the thimble and manifold.
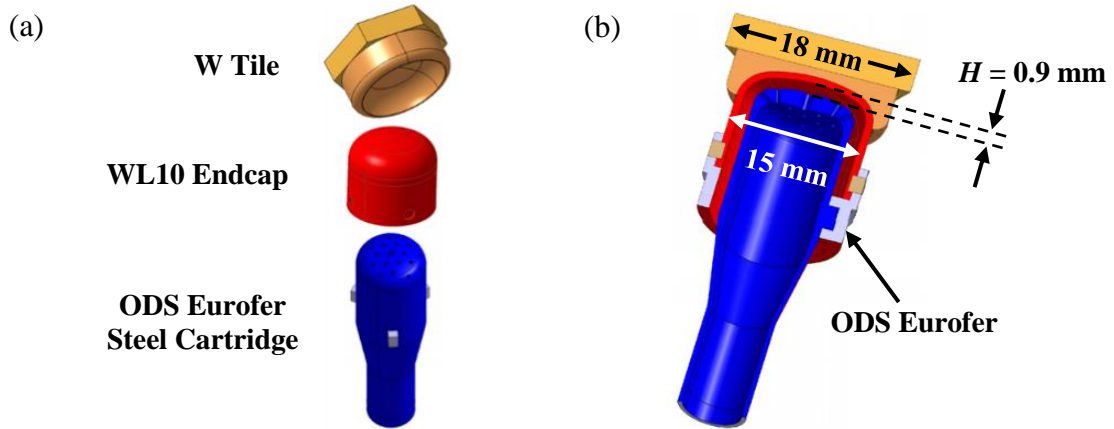
Figure 2.4. (a) Exploded view of the HEMJ divertor and (b) a cross-section of a single module [61].

The WL10 endcap restricts the coolant temperature range to ~600 °C – 1300 °C due to its estimated DBTT and recrystallization temperature (RCT), respectively. Although the W tile has a high melting point of 3410 °C, a design limit of ~2500 °C was assumed for the HEMJ to account for temperature increases during short transients and plasma disruptions. Moreover, the coolant pumping power should be kept below 10% of the total incident thermal power in order to achieve a reasonable system efficiency [60]. An analytical study of early He-cooled divertor designs suggests that a He operating pressure between 8 – 14 MPa is required to maintain an acceptable pumping power [62].

Helium entering the 0.8 mm thick, 11.1 mm OD jets cartridge at 600 °C and 10 MPa is accelerated through twenty-four $\emptyset$0.6 mm holes arranged in a four-row hexagonal array surrounding a larger $\emptyset$1.04 mm central hole. The He jets then impinge upon and cool the pressure boundary, and exits at ~700 °C through the annular gap between the jets cartridge and the endcap. The reference design is designated as J1c, where the separation distance between the cartridge and thimble is 0.90 mm. Early CFD studies concluded that a nominal prototypical mass flow rate $\dot{m}_p$ = 6.8 g/s (corresponding to a prototypical

37

Reynolds number $Re_p = 2.2 \times 10^4$) could withstand a 10 MW/m^2 heat flux and satisfy the pumping power requirement.

The finger modules are combined into a larger 9-finger unit with one helium inlet and outlet port. Several 9-finger units are assembled in series to create a long "stripe-unit". Finally, the stripe-units are assembled in parallel to form divertor target plate. Each stage of this assembly process is depicted in Figure 2.5. This approach allows for individual testing of small units before assembly, which improves reliability. Arrays of small module units also help reduce the overall thermal stresses on the target plates. However, this results in a very large number of finger modules required for full divertor coverage. Approximately 535,000 HEMJ modules, for example, are needed to cover the target plates in a tokamak with a 150 m^2 divertor area. Scaling the production of W(-alloys) and improving the thimble-tile brazing process will be major challenges in the design of future commercial fusion reactors.
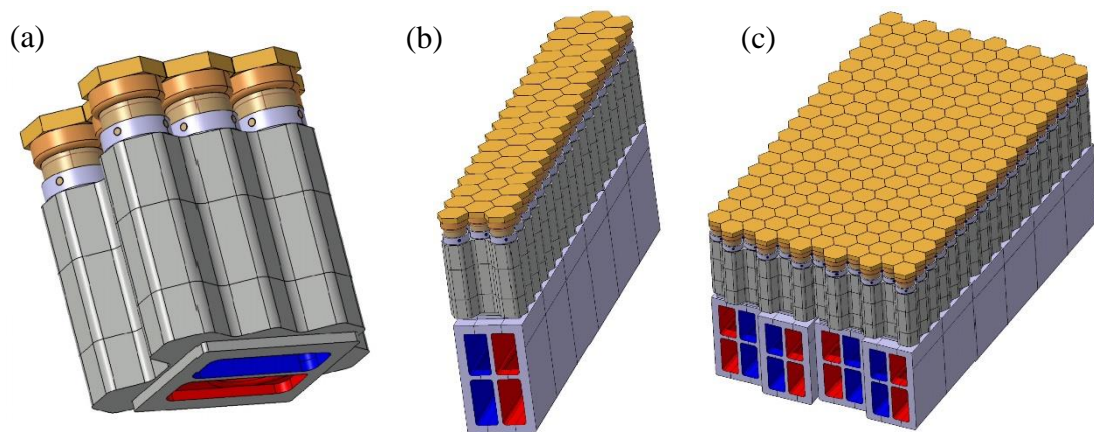
Figure 2.5. The HEMJ assembly process: (a) the 9-finger unit, (b) the stripe-unit, and (c) the target plate [61].

The HEMJ is an advanced divertor design that built on the knowledge gained from the HEMP and helium-cooled modular divertor with integrated slot array (HEMS) designs (discussed in Section 2.3.2). It has therefore been experimentally studied by multiple groups to characterize its thermal-hydraulic performance under a variety of operating conditions. The Gas Puffing Facility (GPF) was one of the first facilities created for the testing of helium-cooled divertors at nearly prototypical conditions [63, 64].

In a collaboration between Forschungszentrum Karlsruhe (FZK, now KIT) and the D.V. Efremov Institute, the GPF was constructed in 2003 to validate preliminary CFD simulations and evaluate the thermal performance of different divertor mock-ups. An early iteration of the facility, known as GPF1, was used to measure pressure drops in various mock-ups at nominal helium inlet conditions using short gas pulses on the order of milliseconds. The facility was later expanded into the GPF2, which consisted of a closed helium loop operating at inlet pressures of 10 MPa and temperatures of 634 °C in longer pulses of ~100 seconds.

Helium was circulated in the loop using a diaphragm compressor at mass flow rates of 5 – 15 g/s. The helium heater consisted of a NiCr resistor jacket that contained 4 mm steel balls and flow ports. The gas cooler at the outlet had a similar design, except the jacket was water-cooled. The thermal performance was evaluated using a "reversed heat flux" principle, where the incident heat flux was determined by cooling a test section heated by helium. The thermal power transferred from hot helium at inlet/outlet temperatures of ~700 °C/600 °C was determined using an energy balance while the heated test section was cooled by a thin film (~0.1 mm) of pressurized water flowing at 30 – 50 kg/s at steady-

state. Pressure drops and HTCs were measured and computed over a range of helium mass flow rates for several different divertor cartridges.

The HEMJ mock-ups for the later GPF2 experiments were composed of L63 brass, which has a thermal conductivity similar to that of tungsten at elevated temperatures. The minimum distance between the top surface of the module and the pressure boundary was only 2 mm (*vs*. 6 mm in the reference design). Two HEMJ variants were studied: the J1a with $D = 0.6$ mm and $H = 1.2$ mm, and the J1e with $D = 0.85$ mm and $H = 0.9$ mm. As shown in Figure 2.6 and Figure 2.7, the J1a and J1e designs could withstand heat fluxes of 12.5 MW/m^2 and 10.5 MW/m^2, respectively, at the nominal mass flow rate. However, the J1a had a larger pressure drop of ~100 kPa compared to ~45 kPa for the J1e [64, 65].
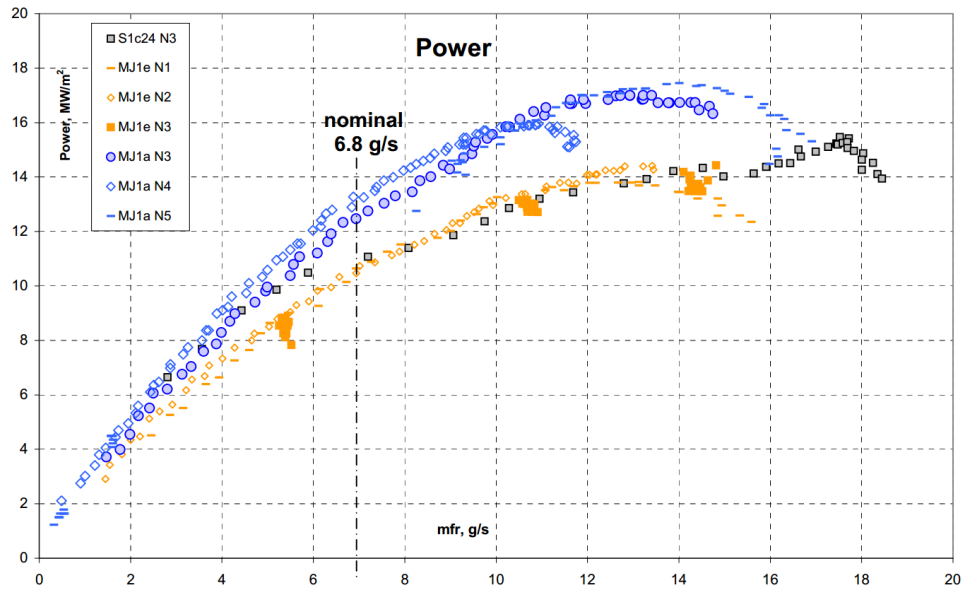
Figure 2.6. Maximum heat flux *vs*. mass flow rate derived from the GPF experiments for two HEMJ variants (blue and orange) and the HEMS (gray) [64].
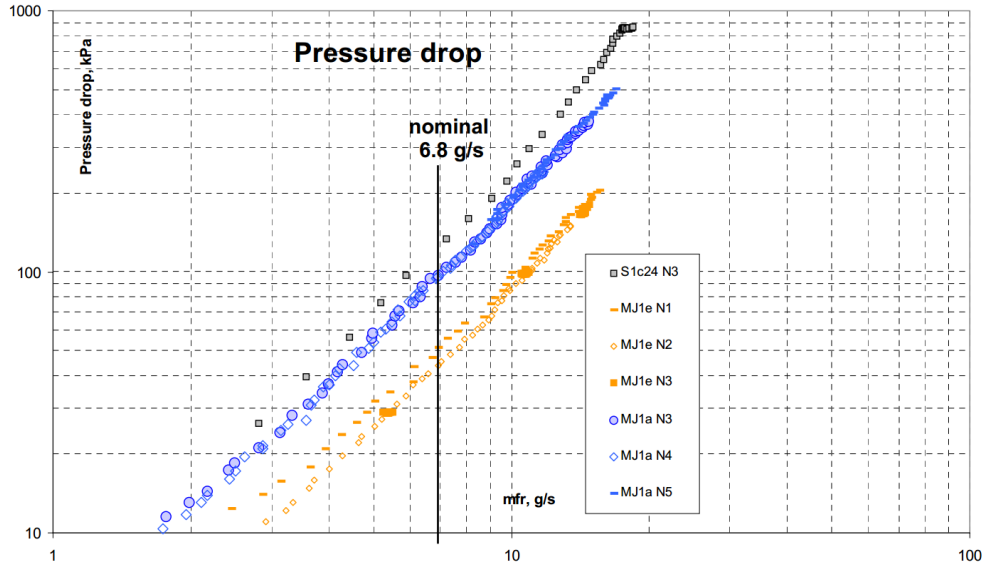
Figure 2.7. Pressure drop *vs*. mass flow rate measured in the GPF experiments for two HEMJ variants (blue and orange) and the HEMS (gray) [64]

From 2006 to 2010, the Efremov Institute and KIT continued experimental studies of the HEMJ at fully prototypical conditions. A high heat flux (HHF) testing facility that contained a closed helium loop and a 60 kW electron beam (EB) was constructed, which allowed for helium pressures, inlet temperatures, and incident heat fluxes of ~520 – 600 °C, 10 MPa, and 5 – 14 MW/m^2 for mass flow rates between 7 and 13.5 g/s [66, 67]. Several variations of the HEMJ were tested in this facility, including designs with castellated tiles, different brazing materials, and different grades of W tiles. In all cases, the J1c design was used for the jets cartridge configuration. One mock-up of the HEMS design was also tested. Instead of operating under steady-state conditions, the mock-ups were thermally loaded in on/off cycles of 30 s/30 s, 60 s/60 s, and 30 s/60 s to evaluate fatigue life and reliability.

Four series of HHF experiments were performed. Two of the six mock-ups tested in the first series survived 10 cycles at 11 MW/m^2 without damage, albeit at a higher flow

rate of 13.5 g/s. While neither sudden brittle failure nor thimble recrystallization was observed in any mock-up, destructive post-examination suggested that defects (*e.g.*, micro-cracks) introduced during the fabrication process greatly reduced the lifetime of a divertor module [68]. The pressure drop in the HEMJ ranged from ~100 kPa to 380 kPa compared to ~300 – 500 kPa in the HEMS. The HEMS was therefore disregarded in subsequent HHF tests due to its high pressure drop and more complex design.

Ten additional mock-ups were created for both the second and third series of tests in 2007 – 2008, where improved machining resulted in better thermal performance. Four of the mock-ups survived 100 heating cycles at 10 MW/m^2 and ~13 g/s. One mock-up accommodated a maximum incident heat flux as great as 14 MW/m^2 for six cycles. Following an upgrade to a 200 kW EB, the fourth test series was conducted on six existing modules in 2010. Five of these modules survived over 200 total cycles at over 10 MW/m^2 before failure, while one module survived 1114 total cycles.

A 9-finger steel mock-up was fabricated in 2009 to characterize pressure drop within the unit without heating. The gas puffing approach was used for He entering at 600 °C and 10 MPa, and mass flow rates between 20 – 100 g/s. The measured pressure drop was ~170 kPa, which was consistent with the range predicted by CFD simulations. An infrared (IR) camera showed a relatively uniform tile surface temperature distribution with temperatures ranging from 500 °C to 550 °C. The temperature distribution within the unit suggested that flow distribution within each finger was also uniform.

After a long hiatus, a 9-finger W unit (Figure 2.8) was fabricated and tested in the HHF facility in late 2013 [69, 70]. The He inlet temperature and pressure was 500 °C and 9.5 – 10 MPa. The W unit survived 25 cycles with an on/off interval of 20 s/20 s at 3

42

MW/m^2 and 26 g/s. The mass flow rate was increased to 50 g/s, allowing the module to sustain a maximum heat flux of 6 MW/m^2 for 3 cycles before a helium leak was detected. Infrared images taken at 6 MW/m^2 suggest that while the surface tile temperature distribution is mostly uniform, localized hot spots appear between the tiles.
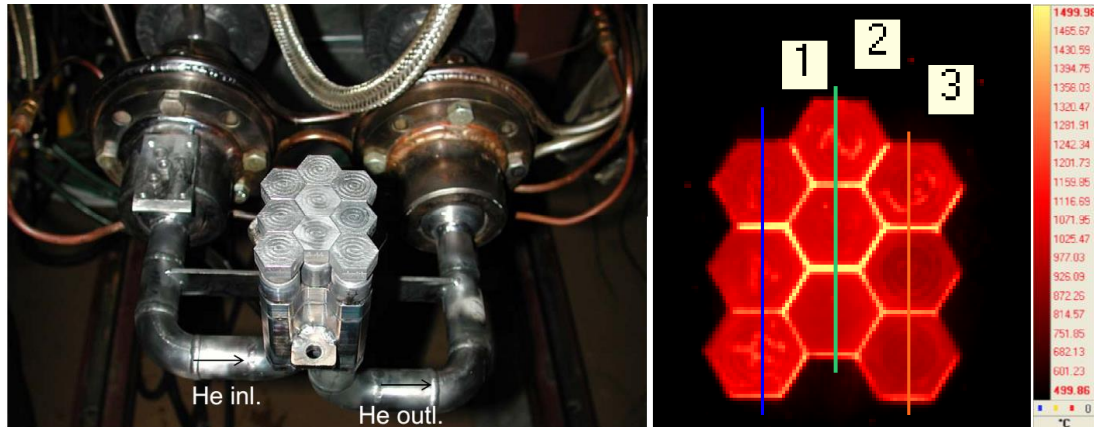
Figure 2.8. Picture of the 9-finger W unit in the HHF facility (left) and IR image of the unit at 6 MW/m^2 (right) [70].

A finger module with dimensions similar to the HEMJ has also been studied in dynamically similar small-scale experiments by our group at the Georgia Institute of Technology (GT). Weathers *et al.* [71, 72] and Crosatti *et al.* [73, 74] performed experiments on a single brass HEMJ finger module heated with an electric cartridge heater and cooled with air at ambient temperature and pressure for mass flow rates and incident heat fluxes up to 8 g/s and 1 MW/m^2, respectively. The Nusselt number results were effectively independent of incident heat flux over the range of mass flow rates studied. A numerical model of the module was developed in ANSYS® Fluent® 6.2 and validated against the experimental results in terms of pressure drop and HTCs.

Rader *et al*. [31, 75] performed additional experiments on this module with the goal of developing parametric divertor performance curves. Experiments were conducted with air, argon, or helium at ambient temperature and pressures up to 1.4 MPa. An oxy-acetylene torch provided incident heat fluxes up to 3 MW/m². Measured temperatures and pressures were used to calculate average Nusselt numbers and pressure loss coefficients. In addition, a new non-dimensional parameter was introduced

$$\kappa = k_s/k_f \tag{2.32}$$

where k_s is the thermal conductivity of the outer shell evaluated at the area-averaged cooled surface temperature $\overline{T_c}$ and k_f is the thermal conductivity of the fluid evaluated at $T_{ave} = (T_i + T_o)/2$. This term was required to account for changes in $\overline{Nu}$ due to different combinations of structural materials and coolants. Although *Bi* was also considered as a nondimensional parameter for Rader's $\overline{Nu}$ calculations, *Bi* is a function of $\bar{h}$, which was unknown during his experiments. Generalized correlations for the Nusselt number and loss coefficient were therefore developed based on experimental data by matching only *Re* and κ for multiple coolants and module materials. The correlations were then extrapolated to prototypical conditions for different average pressure boundary temperatures $\overline{T_s}$ and coolant pumping powers (as a fraction of the incident thermal power) β.

More recently, Mills *et al*. [32, 76] performed experiments on a WL10 HEMJ module at nearly prototypical conditions using a helium loop. A reciprocating compressor provided He mass flow rates up to 10 g/s at 10 MPa, and two 2 kW electric cartridge heaters provided inlet temperatures up to 300 °C. An induction heater was used to supply steady-state incident heat fluxes up to 6.6 MW/m². Correlations developed based on these data

44

were again extrapolated to fully prototypical conditions. Figure 2.9 depicts the prototypical design curves for a single HEMJ module with $T_i = 600\ °C$.
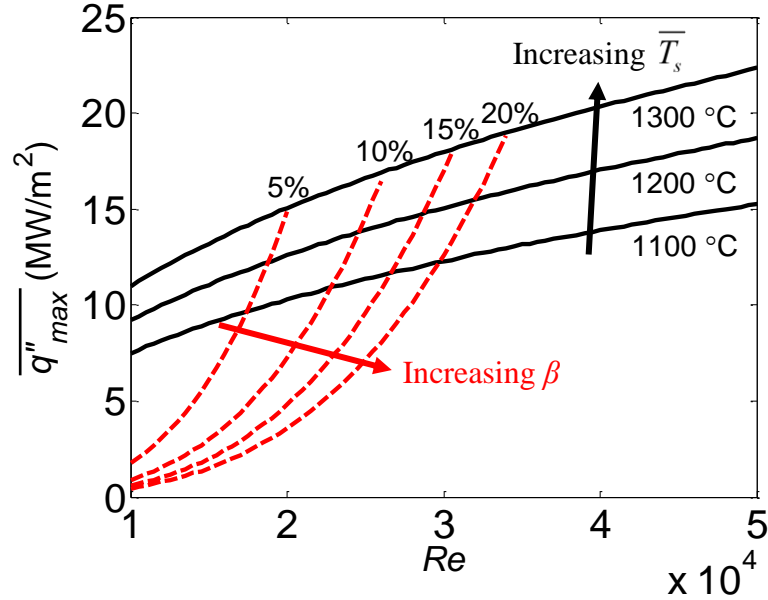
Figure 2.9. Maximum heat flux for a single HEMJ module with $T_i = 600\ °C$ [32].

The extrapolated results reported by Mills *et al*. suggest that the HEMJ can accommodate a maximum incident heat flux of 10.7 MW/m² at $\dot{m}_p = 6.8$ g/s when $T_i = 600\ °C$ and $\overline{T}_s = 1200\ °C$. The mass flow rate corresponding to a maximum heat flux of ~10 MW/m² is significantly lower compared to those used in the HHF experiments for similar heat fluxes and coolant inlet temperatures. Further experiments are therefore required to confirm the validity of the proposed correlations and extrapolations, especially at higher inlet temperatures and incident heat fluxes.

2.3.2   Helium-cooled Modular Divertor with Integrated Pin/Slot Array

One of the earliest modular helium-cooled tungsten divertor designs was the helium-cooled modular divertor with integrated pin array (HEMP) proposed by Diegele *et al*. in 2003 [77]. The HEMP design is shown in Figure 2.10 and consists of a square W tile brazed to a 1 mm thick WL10 thimble. The inner surface of the thimble contains an array of cylindrical extended surfaces, or pin fins, that enhance heat transfer and allow the divertor to accommodate high heat fluxes. Helium enters the annulus created by the thimble and ODS Eurofer steel tube at 600 °C and 10 MPa, flows through the pin fins to remove heat, and exits through the inner tube at approximately 700 °C.
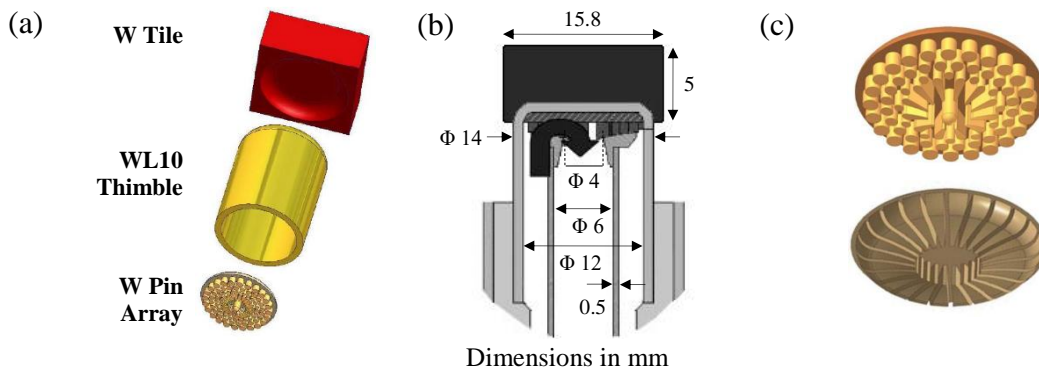
Figure 2.10. (a) Exploded view of the HEMP module, (b) HEMP cross-section, and (c) rendering of a pin and slot array [77, 78].

Rader *et al*. [79] and Mills *et al*. [80, 81] performed experiments on a single HEMP divertor module for two types of flow configurations: forward and reverse flow, where the He enters from the inner tube and annulus, respectively. Each configuration was also tested for designs with and without fins, resulting in a total of four different cases. The experiments were conducted on steel and brass test sections cooled by either air, argon, or

helium at ambient temperature and pressures up to 700 kPa. The results were then extrapolated to fully prototypical conditions. The cases with pin fins consistently allowed for higher maximum heat fluxes, while the reverse flow cases resulted in higher pressure drops. Extrapolating these results to prototypical conditions suggested that the forward flow configuration with pin fins provided the best thermal-hydraulic performance, with a maximum incident heat flux of 20.6 MW/m^2 and pumping power of 12.3% at a helium mass flow rate of 4.8 g/s, coolant inlet temperature of 600 °C, and maximum thimble temperature of 1200 °C.

Although the HEMP design was considered to be a leading candidate in the early stages of divertor research, fabrication of the pin fin arrays proved to be a major challenge, even for a single module. It was therefore abandoned in favor of simpler designs such as the HEMS. As shown in Figure 2.10, the main difference between the HEMP and HEMS is the fin array geometry, which is somewhat simpler to manufacture in the latter design. As previously mentioned, the HEMS was only briefly studied before it was overshadowed by the HEMJ. One HEMS mock-up was tested during the first series of experiments at the HHF facility, and survived 200 cycles at heat fluxes of 9 MW/m^2 before failing. However, it was ultimately eliminated as a potential divertor candidate due to its relatively high pressure drop and complex geometry.

2.3.3   T-Tube Divertor

Several additional modular He-cooled divertor designs have been proposed that contain larger plasma-facing surfaces than finger-type divertors, such as the T-Tube

divertor. The T-Tube concept was first proposed by Ihli *et al*. [82] for the ARIES Compact

Stellarator study, which has the same divertor performance criteria as tokamaks. A cross-

section of a single T-Tube module is shown in Figure 2.11. Helium enters a central channel

at 600 °C and 10 MPa and flows across a ~100 mm long perpendicular tube in two opposite

directions. The flow is accelerated through several 0.5 mm wide slots equally spaced along

the length of the W-alloy inner tube, cools the 0.3 mm thick W tile armor on the outer tube,

and travels though the annulus between the tubes before exiting parallel to the inlet channel.

A circular cross-section was adopted to allow for low radial temperature differences, and

hence, thermal stresses. Although the T-Tube is simpler than finger-type units, maintaining

a uniform flow through such a long slot is a major issue for this design. A total of ~110,000

T-Tube modules would be required to cover a divertor area of 150 m^2, compared to the

535,000 finger-type units required for full plate coverage.
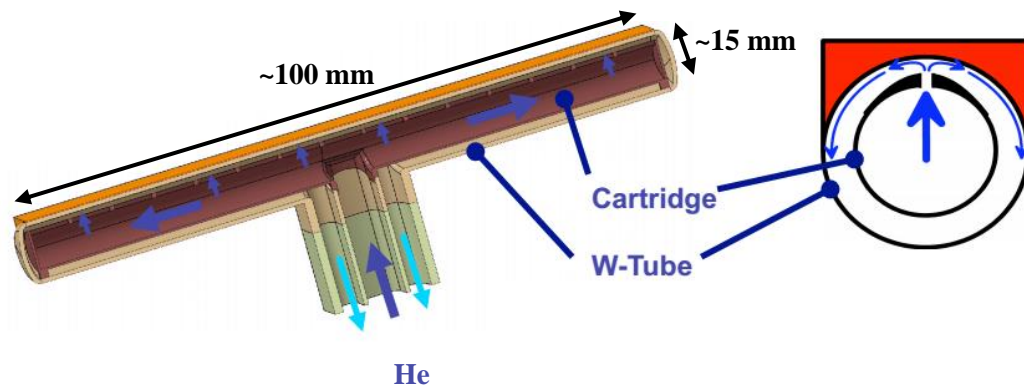
Figure 2.11. Cross-section (left) and end view (right) of the T-Tube divertor [82].

The thermal performance of the T-Tube divertor was experimentally investigated

by Crosatti *et al*. [73]. The dynamically similar experiments were performed with an open

flow loop containing air at room temperature and a pressure of 414 kPa for mass flow rates

up to 20 g/s. Electric cartridge heaters embedded in a Cu heater block were used to provide

steady-state heat fluxes as great as 0.85 MW/m^2 incident on a C36000 brass test section with dimensions similar to the T-Tube divertor. The experimental results obtained from thermocouple measurements showed good agreement with numerical simulations performed with ANSYS® Fluent® over a wide range of Reynolds numbers.

More recently, Burke *et al*. [83] performed numerical simulations using ANSYS® CFX® 12.0 to evaluate and optimize the thermal performance of the T-Tube divertor at prototypical conditions as part of the ARIES study. Five designs were considered including configurations where the W tile thickness was either 1 mm or 5 mm, and the inner tube was either tapered or non-tapered. The simulation results suggested that all five designs could accommodate heat fluxes greater than 10 MW/m^2 while remaining within a maximum alloy temperature of 1300 °C and stress limit of 450 MPa. The maximum allowable heat flux for the T-Tube divertor can also be increased by decreasing certain dimensions such as the outer tube diameter or outer wall thickness. An incident heat flux of 20 MW/m^2, for example, would require a tube diameter of 7.5 mm and outer wall thickness of 0.25 mm [82]. However, the outer wall thickness in the original design is already small (~1 mm), and any further reduction in size may lead to fabrication and reliability issues.

2.3.4   *Helium-cooled Flat Plate Divertor*

The helium-cooled flat plate (HCFP) divertor has the largest plasma-facing surface area for a given module among the different divertor designs. The HCFP was originally proposed by FZK in 2002 prior to the development of modular finger-type divertors [78].

Recent iterations of this 'plate-type' divertor consist of planar jets impinging on relatively large tile areas in order to maintain a uniform surface temperature distribution and to reduce thermal stresses [84]. The latest iteration of the HCFP design proposed by the ARIES team is depicted in Figure 2.12. The plate consists of a 5 mm thick castellated W tile and an array of nine 1 m long channels with a total width of ~20 cm. The main advantage of the HCFP divertor is that these larger individual modules significantly reduce the total number of units required in a target plate. Since each module can cover an area of ~2000 cm^2, only ~750 plate units are needed to cover a divertor area of 150 m^2.
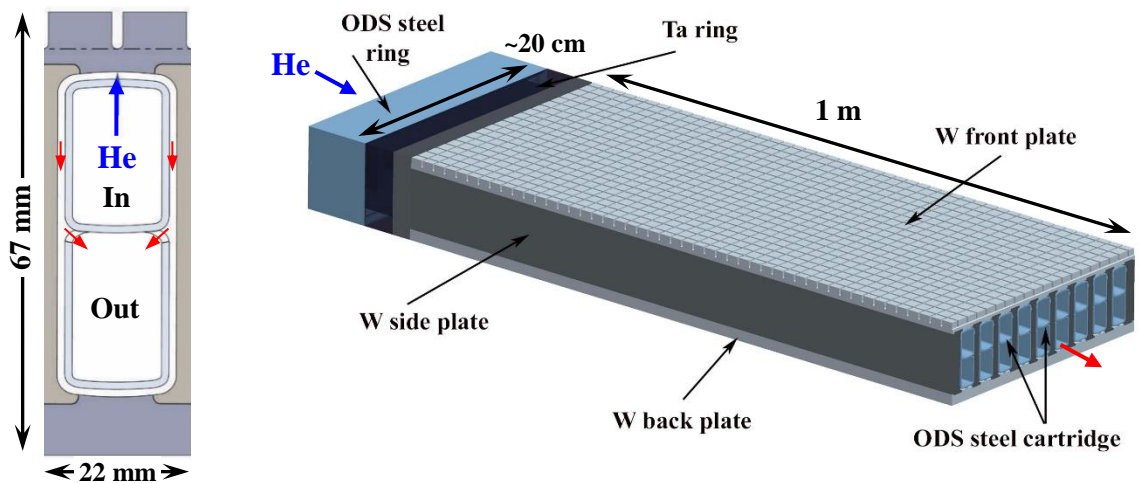
Figure 2.12. A cross-section of a single HCFP module (left) and the ARIES plate-type divertor (right) [85, 86].

The ARIES team has performed several design studies and numerical simulations to characterize the thermal performance of various versions of the HCFP. Wang *et al*. [86] performed thermo-mechanical simulations on the HCFP using ANSYS® Workbench™ assuming a He operating pressure of 10 MPa and an inlet temperature of ~700 °C (based on a higher DBTT expected from neutron irradiation effects). The results suggested that

thermal stress limits could only be met if the maximum allowable heat flux for the HCFP was restricted to ~9 MW/m^2, which is much lower than the ~14 MW/m^2 limit predicted for the HEMJ divertor under similar conditions.

In contrast, Hageman *et al.* [30] performed dynamically similar experiments on a brass test section based on a single HCFP module using air at room temperature and an inlet pressure up to 700 kPa. His results suggested that a single HCFP module could accommodate heat fluxes of 13 MW/m^2 and 18 MW/m^2 at prototypical conditions for configurations with and without pin fins, respectively. The most favorable configuration involved a jet exiting from a 2 mm wide slot impinging upon a surface with pin fin arrays, although the pin fins also increased the pressure drop by 40% – 80% compared to cases without fins. Further experiments are required to characterize the thermal performance of the HCFP, especially at prototypical conditions with He and W.

2.3.5   *Combined Divertor Concepts*

While many helium-cooled divertors studies have operated under the assumption that the nominal incident steady-state heat flux is a constant 10 MW/m^2 distributed uniformly over the surface of a single tile, the actual heat flux profile in future reactors is currently unknown, and transient heat flux values could be as great as 50 MW/m^2 [87]. For DEMO, the steady-state heat flux distribution for an outboard (*i.e.*, radially furthest from the tokamak center) target plate is assumed to have a Gaussian profile with a peak of 10 MW/m^2 that varies in the poloidal direction [28, 60]. As depicted in Figure 2.13, the location of the actual peak is assumed to lie between 0.1 – 0.5 m from the bottom edge. To

reduce the overall pressure drop, the plate is divided into two 0.5 m long zones, where He

enters at ~600 °C and ~634 °C in the first and second zone, respectively. Since only part

of the plate will be subjected to a 10 MW/m^2 heat flux, it may be advantageous to use

simpler divertor designs with lower thermal performance in conjunction with the HEMJ

divertor to reduce costs. This type of configuration is known as a "combined" or

"integrated" divertor design.
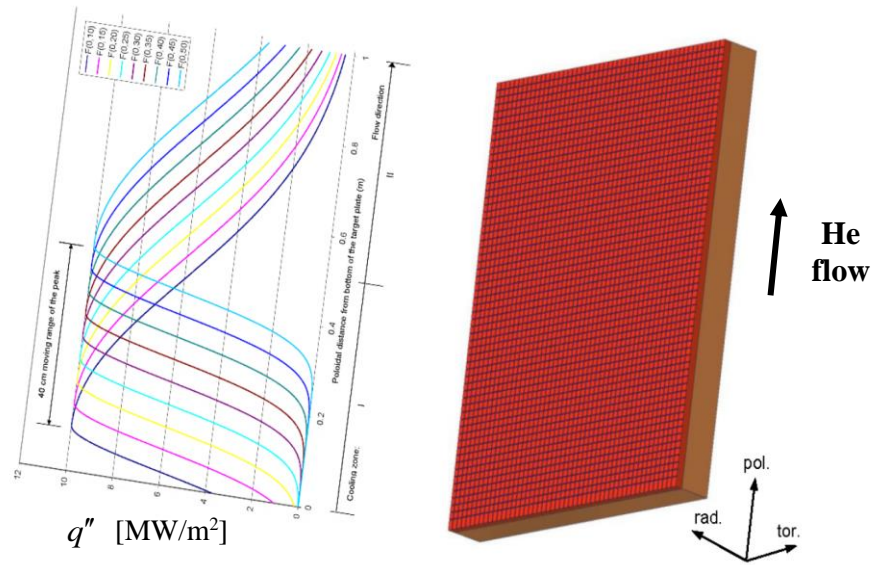
Figure 2.13. Poloidal surface heat flux distribution assumed for an outboard target plate
of the DEMO reactor [28].

An example of a combined divertor design for a two-zone target plate is a

configuration in which arrays of T-Tube and HCFP modules cover the high and low heat

flux regions, respectively [88]. For a 19.2 cm wide target plate with a 25 cm long high

heat flux region (in the poloidal direction), this combined divertor configuration would

reduce the number of units to ~27,500 T-Tube modules and 562 plate units. A unique

manifold layout that attaches to a common support structure would be required to provide the appropriate flow paths for the two different module arrays.

The integrated plate/finger concept (Figure 2.14) is another promising example of a combined divertor design proposed by Wang *et al*. [88] in 2009. This design utilizes the HCFP concept in regions where the heat flux remains below $6 - 8$ MW/m^2 while HEMJ-like finger modules are used in regions where the heat flux exceeds $6 - 8$ MW/m^2. An important advantage of this approach is that unlike the original HEMJ design, brazing is only required between the thimble and top plate which are both composed of a W-alloy. This may simplify manufacture and improve reliability due to reduced CTE mismatch between the thimble and the supporting structure. For a 25 cm long high heat flux zone, the integrated divertor significantly reduces the number of required finger units to ~87,820.
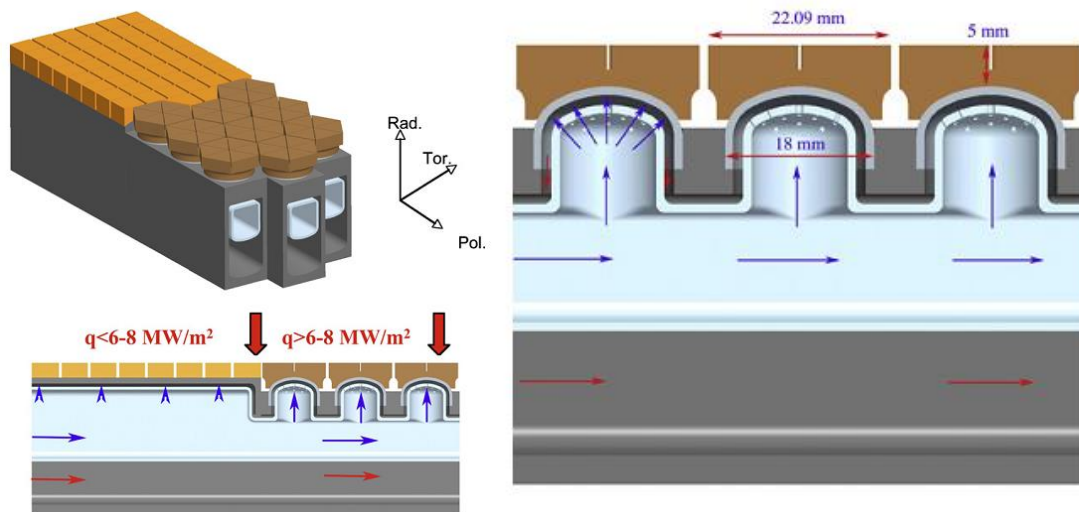
Figure 2.14. Rendering of an integrated plate/finger-type divertor (left) and dimensions of the finger units (right) [88].

2.4   Numerical Simulations of the HEMJ Design

Experimental studies of divertor modules are both challenging and costly due to the high pressures, temperatures, and incident heat fluxes expected in fusion reactors. The few experiments that have been conducted at fusion-relevant conditions have only considered a single module, or a few modules, of a specific geometry. New test sections must be fabricated to account for even minor geometric changes, which requires additional time and resources, and fabrication of W and W-alloy components imposes even more challenges. Moreover, the extreme conditions within a reactor make it impractical to obtain certain measurements such as local temperature distributions and thermal stresses. Numerical simulations are therefore a rapid and cost-effective alternative for evaluating various divertor designs over a range of conditions.

Most numerical simulations of the HEMJ design have been performed with modules available in the commercial software package ANSYS® and validated by experimental measurements from Efremov. The thermal-hydraulics of a complex divertor finger such as the HEMJ is often simulated using a steady-state RANS turbulence model available in ANSYS® CFX® or Fluent®. More recently, several groups have performed thermo-mechanical simulations that couple the CFD results with a structural FEM simulation using ANSYS® Mechanical™ or ABAQUS®. This section summarizes the numerical simulations performed on HEMJ-like divertor modules using commercial software packages.

A parametric study of the HEMJ divertor was performed by Kruessmann *et al*. [89] at FZK in 2008 using ANSYS® CFX®. Eight different jet arrays were studied including cases where *H* ranged from 0.6 mm to 1.2 mm and the number of jet holes ranged from 7 to 25 (while keeping the total jet area constant). Steady-state simulations were performed using the RNGKE model with boundary conditions that include a uniform incident heat flux of 10 MW/m^2, inlet mass flow rate of 6.8 g/s, coolant inlet pressure of 10 MPa, and inlet temperature of 634 °C. The results showed that varying *H* and the number of jet holes had relatively little effect on the maximum thimble temperature and pressure drop. The results also suggested that all of the designs with 25 jet holes could remove a heat flux of 10 MW/m^2 at a mass flow rate of 6.8 g/s. A design with 24 $\emptyset$0.4 mm holes gave slightly higher HTCs but also significantly increased pressure drop. The design with 24 $\emptyset$0.6 mm diameter holes surrounding a $\emptyset$1 mm central hole at *H* = 0.9 mm was selected as the reference design due to a reasonable balance of thermal performance and pressure drop.

Crosatti *et al*. [73] developed a half-model of an HEMJ-like brass divertor module that included the cartridge heater, insulation, and manifold used in the corresponding dynamically similar experimental setup. The simulations were performed using the SKE model in ANSYS® Fluent® with standard wall functions and boundary conditions that were chosen to match the experimental measurements. The predicted temperatures showed good agreement with measurements from embedded thermocouples. Moreover, the temperature distribution within the solid (Figure 2.15) was shown to be fairly uniform due to the relatively good thermal conductivity of brass. The local HTCs at each thermocouple

location also agreed well with the simulations predictions over a wide range of Reynolds numbers. No simulations were performed, however, for fully prototypical conditions.
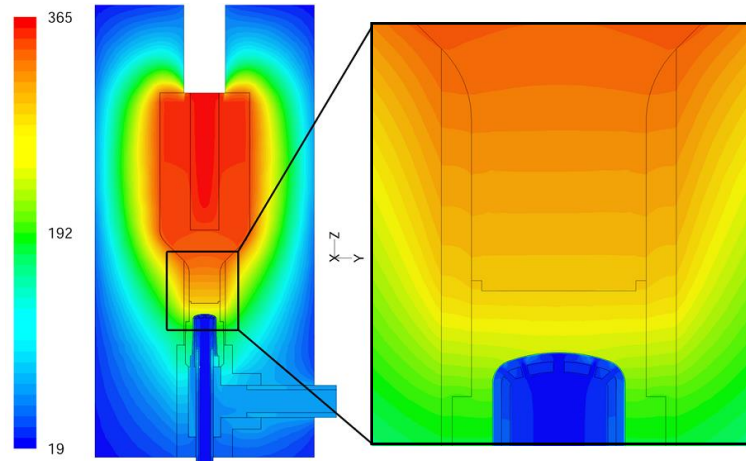
Figure 2.15. Temperature distribution [°C] of the brass HEMJ test section (left) and in a close-up of the impingement region (right) [73].

2.4.2   *Thermo-mechanical Simulations*

Several groups have recently extended the numerical thermo-fluid analysis of divertor modules to include structural analysis. This is typically achieved by supplying the HTC and pressure results from CFD simulations to an FEM model and applying appropriate boundary conditions. Norajitra *et al*. [28] applied this one-way coupling technique to the model developed by Kruessmann *et al*. to create tile designs with reduced stresses in the divertor module. Several different W tile shapes were simulated and von Mises stresses were compared to the original HEMJ design. The results of these one-way coupled CFD/FEM simulations suggested that a tile with a concave chamfered shoulder (Figure 2.16) could reduce maximum von Mises stresses at the expense of slightly higher maximum tile and thimble temperatures, while also remaining below the thimble RCT.

This tile design was further improved by incorporating diagonal castellations, resulting in the W divertor designs ultimately tested at Efremov.
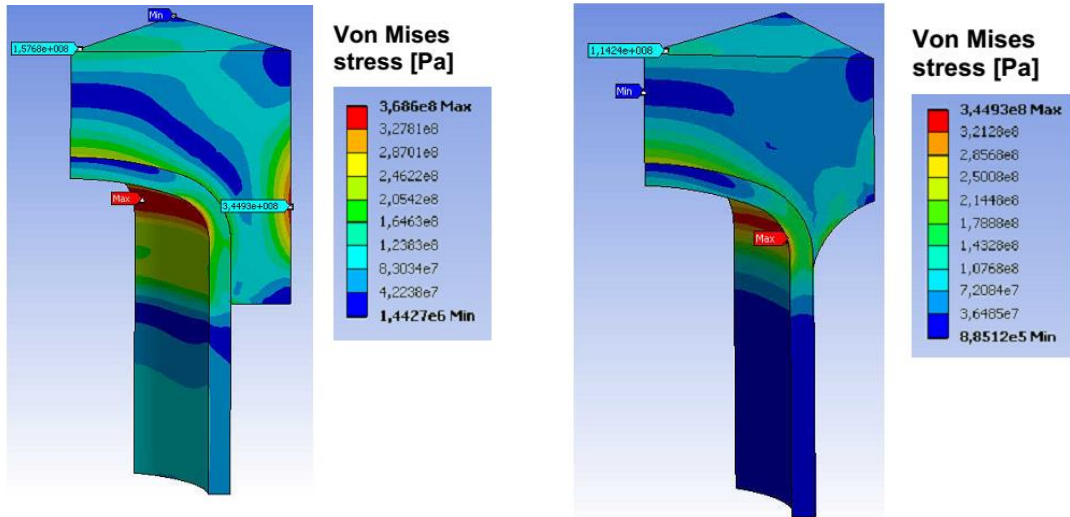
Figure 2.16. Calculated von Mises stress distributions for the original (left) and optimized (right) HEMJ tile designs [28].

More recently, Wang *et al*. [90] performed thermo-mechanical simulations of a single HEMJ-like finger module for the integrated plate/finger concept at prototypical conditions using the SKE model in ANSYS® CFX® with EWT. Unlike the base design, the thimble diameter and tile width was enlarged to 20 mm and 23 mm, respectively. The tile was also castellated with small triangles, and vacuum-metallized W was chosen for the thimble material. The mechanical simulations were performed using one-way coupling between the CFD results and a finite element model. Thermal stresses were calculated by applying the HTCs and temperatures at the He/W interfaces as boundary conditions. For this design, the simulations predicted a maximum von Mises stress of 481 MPa at the thimble and a maximum thimble temperature of ~1295 °C (Figure 2.17).
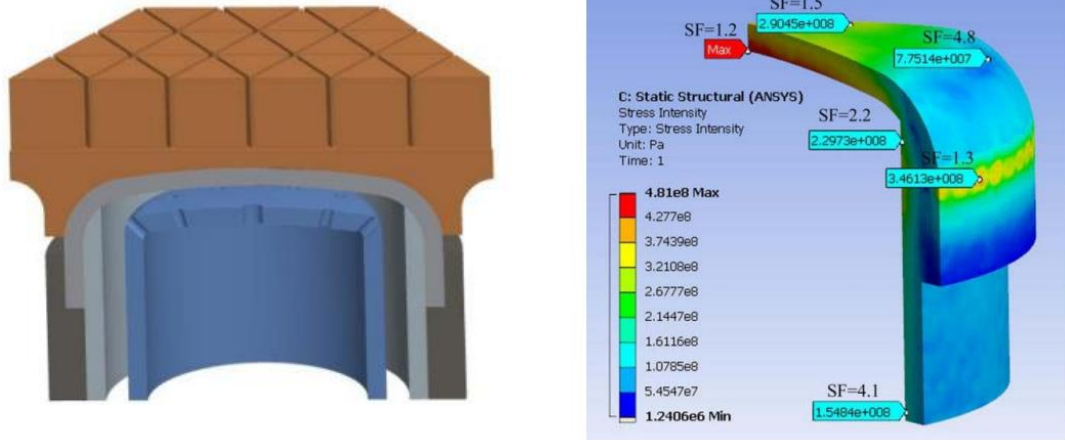
Figure 2.17. The ARIES modular finger unit (left) and the calculated von Mises stress distribution in the W-alloy thimble (right) [90].

Many helium-cooled divertor concepts have been proposed and studied numerically. Finger-type divertors are promising because they have HTCs large enough to effectively remove the heat fluxes incident on the W tiles. Specifically, the HEMJ is the only modular helium-cooled divertor design that has been experimentally shown to withstand heat fluxes of at least 10 MW/m^2. However, the few experimental studies of the HEMJ at prototypical conditions were performed for a limited range of coolant mass flow rates and helium inlet temperatures. A detailed experimental investigation of the HEMJ design that spans a wider range of operating conditions will therefore improve understanding of divertor performance for future long-pulse fusion reactors.

CHAPTER 3: HEMJ DIVERTOR EXPERIMENTS

This chapter describes the setup, procedure, and results for experiments performed at nearly prototypical conditions on a W-alloy divertor test module that closely resembles the HEMJ design. Steady-state experiments were performed on MT185 (97% W, 1% Fe, 2% Ni) and WL10 test sections at coolant inlet temperatures ranging from nearly ambient (~30 °C) to 425 °C (*vs.* a prototypical value of 600 °C) over a range of Reynolds numbers (spanning Re_p). A closed helium loop and an induction heating system provided prototypical inlet pressures of ~10 MPa and incident heat fluxes based on a coolant energy balance as great as 6.6 MW/m^2 (*vs.* a prototypical value of 10 MW/m^2). Average Nusselt numbers and loss coefficients were calculated from experimental measurements of area-averaged cooled surface temperatures and pressure drop, respectively, and compared with previous results obtained by Mills [32] at lower inlet temperatures and incident heat fluxes. The effect of varying the separation distance H between about 0.5 mm and 1.5 mm was also investigated.

3.1.   Experimental Apparatus

3.1.1   HEMJ Test Section

The HEMJ test section used in this work consists of an AISI 304 stainless steel jets cartridge confined by a W-alloy outer shell and an AISI 304 stainless steel manifold that contains the inlet and outlet flow ports. As shown in Figure 3.1, the outer shell and jets cartridge are geometrically similar to the J1c design of the HEMJ divertor proposed by

KIT. However, the outer shell is composed of a single material (*vs*. W and WL10 in the J1c design) and has a simpler design that only models the pressure boundary (*vs.* a thimble brazed to the hexagonal plasma-facing tile).
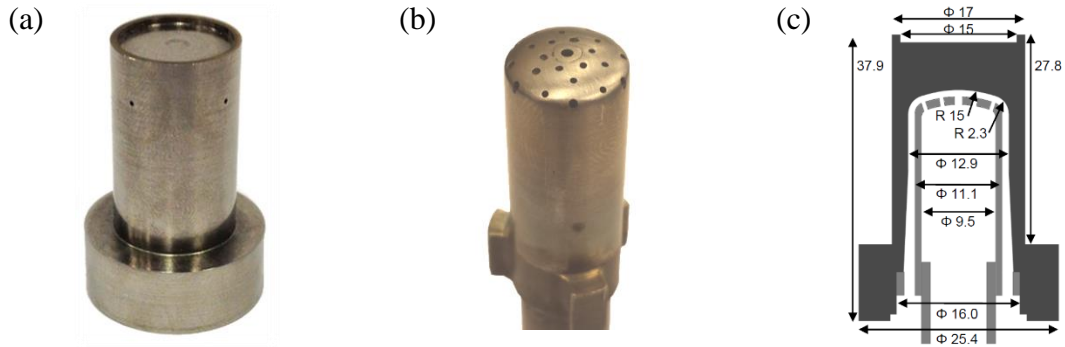
Figure 3.1. Pictures of (a) the W-alloy outer shell and (b) the steel jets cartridge. (c) A cross-section of the HEMJ test section (dimensions in mm).

The outer shell is a 27.8 mm tall cylinder with a 17 mm OD and a 12.9 mm ID cavity that models the divertor module pressure boundary. The cooled surface has a 15 mm radius of curvature with a fillet with a radius of 2.3 mm at the edge; these dimensions are identical to those of the J1c design of the HEMJ. The bottom of the outer shell has a 10.1 mm thick flange with a 25.4 mm OD used to seal the test section to the manifold. The top of the shell has a 1 mm thick ridge used to secure the workpiece for induction heating.

Two different W-alloys were used in this work: MT185 and WL10, both purchased from Midwest Tungsten Service. Eight thermocouple (TC) holes spaced azimuthally by 90° were machined by electrical discharge machining (EDM) into the side of the outer shell at different axial locations and radial depths. Four type-K TCs with 0.5 mm OD probe sheaths were embedded into these holes, which ended ~0.5 mm away from the cooled surface, at radial distances $r = 0$ mm, 2.1 mm, 4.2 mm, and 6.4 mm measured from the

centerline (Figure 3.2). The temperatures measured by these TCs were used to estimate an area-averaged cooled surface temperature. Four additional type-K TCs with 1 mm OD probes were silver-soldered into ~1 mm deep holes within the side wall of the outer shell; these TC measurements were used in turn to estimate the heat transferred through the sidewalls by conduction.
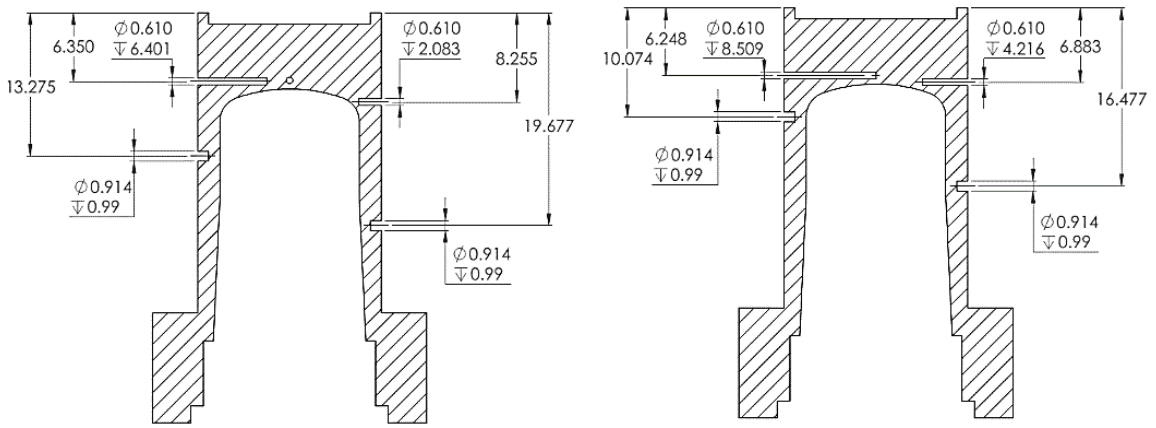
Figure 3.2. Thermocouple hole locations at two orthogonal planes (dimensions in mm).

The stainless steel jets cartridge used in this work (Figure 3.3) is geometrically identical to the HEMJ J1c design. The cartridge ends in a curved surface containing an array of jet holes with 24 $\emptyset$0.6 mm holes surrounding a single 1.04 mm diameter central hole in a hexagonal array. The 24 smaller holes are arranged in four rows of six equally spaced holes, with a different *S/D* for each row. The inner contour of this curved surface has a 13.1 mm radii of curvature and a 1 mm fillet, while the outer contour has a 14.1 mm radii of curvature and a 2 mm fillet.

The inlet tube of the jets cartridge has a 9.5 mm ID and 11.1 OD with a 16.3 mm OD flange at the bottom. The inner surface of the flange is threaded, allowing it to be

61

mounted onto a holder and for *H* to be adjusted between experiments. A compression spring was used to secure the position of the cartridge and maintain a consistent *H* during the experiment. The maximum clearance between the outer flange surface and manifold port was ~0.1 mm, which ensured that the jet cartridge remained concentric with the test section.
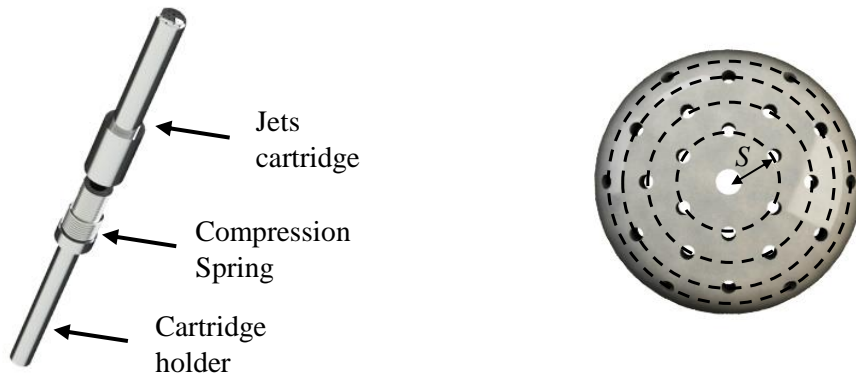
Figure 3.3. Jets cartridge assembly (left) and end view of the jet nozzle (right). The dashed lines indicate one row of equally spaced holes.

The test section was sealed to the manifold (Figure 3.4) by compressing the outer shell and a 1.02 mm thick copper (Cu) gasket using a steel compression collar. The jet cartridge assembly was secured within the vertical manifold port (*cf.* Figure 3.3). Helium (He) enters the inlet port at the bottom of the manifold vertically, exits through the holes in the jets cartridge to form 25 jets, which then impinge on and cool the inner surface of the outer shell. The heated He then flows downward in the annular gap between the cartridge and outer shell, finally exiting the test section horizontally through a 12.7 mm OD outlet port. The inlet and outlet He temperatures were measured by four-wire resistance temperature detectors (RTDs) (OMEGA P-M-A-1/8-6-0-TS-8) with closed

probes to prevent direct contact between the fluid and the sensor element. The temperature

rating of these RTDs depend on both the element and cable selection. Although the

maximum temperature rating for these RTD elements was 450 °C, the actual maximum

temperature rating was limited to 250 °C by the temperature limit of the perfluoroalkoxy

insulated cables. The remaining three 6.4 mm OD ports on the manifold are

instrumentation ports, two of which are used for pressure measurements. The static

pressure of the coolant at the outlet was measured by a static pressure transducer (Dwyer

626-16-GH-P1-E2-S1) at the manifold, while the pressure drop across the test section was

measured by a differential pressure transducer (Rosemount 1151DP5S22) connected to the

inlet port and the manifold.
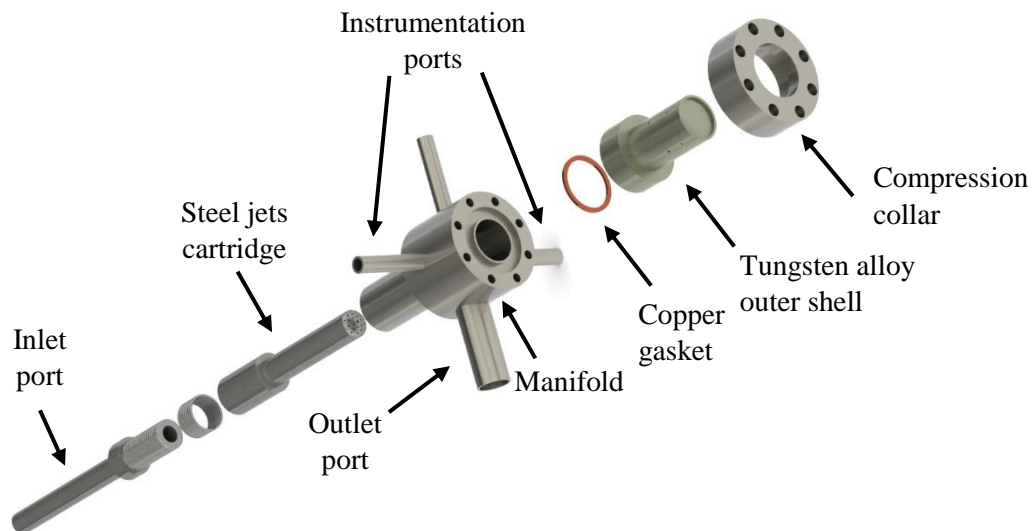
Figure 3.4. Exploded view of the test section assembly

The entire assembly was supported by a Unistrut® frame and heavily insulated with

mineral wool to reduce thermal losses. The region around the outer shell is surrounded by

a stack of Marinite® plates, except for the ~10 mm thick portion near the heated surface which is insulated instead with Marinite® powder to make it possible to insert the TCs and adjust their positions. The support structure and Marinite® plates contain through-holes that were used to bolt the plates together and clamp the TCs, after adjustment, at a fixed location.

3.1.2 Induction Heating

The previous experiments of the HEMJ test section by Mills [32] used an oxy-acetylene flame that impinged upon the top surface of the outer shell to simulate a steady-state incident heat flux. Although such a flame should be able to provide high heat fluxes, the flame diameter was limited to ~2 mm, which restricted the maximum heat flux to 2.8 MW/m^2. The torch was therefore replaced in these experiments with an induction heating system to achieve higher heat fluxes.

A 10 kW induction heater (Ambrell EasyHeat LI) on loan from the Safety and Tritium Applied Research (STAR) facility at Idaho National Laboratories was used for the experiments performed in this work. This induction heater generates a rapidly alternating magnetic field by passing high frequency AC current through an electromagnet (*i.e.*, coil). Eddy currents are produced in an electrically conducting object, or "workpiece", placed in the center of the magnetic field, which results in rapid Joule heating of the workpiece. A major advantage of induction heating is that there is no direct contact between the workpiece and the coil. However, oxidation of metal workpieces can become an issue over longer heating times or if the workpiece is exposed to air over long times.

Axial conduction from an inductively heated workpiece was used to simulate the incident heat flux on the test section. A workpiece of MT185 or WL10 was heated by a water-cooled Cu coil and placed in contact with the top surface of the outer shell; a 0.15 mm thick Cu shim between the workpiece and outer shell was used to improve heat transfer. The workpieces consisted of 30 mm long pieces of 25.4 mm OD rod with a tapered end that fit inside the 15 mm ID rim of the WL10 outer shell. Experiments were also performed on an MT185 outer shell with an extended axial dimension of 62.4 mm (the "integrated" outer shell) to enable direct induction heating of the test section without a workpiece. Several different coils were tested to determine the optimal dimensions required to maximize the thermal energy generated within the workpiece, and a custom helical coil made from 4.76 mm OD Cu tubing was ultimately used for these experiments. The coil had a 38.1 mm diameter, 19 mm height, and three turns (Figure 3.5).

To reduce the effects of oxidation, a small enclosure was constructed around the coil and workpiece, and supplied with a continuous flow of argon (Figure 3.5). The enclosure consisted of three 25.4 mm thick Duraboard® side walls, one transparent pane of 6.35 mm thick Pyroceram® glass, and a top Duraboard® cover. Argon (Ar), supplied at a constant pressure of ~55 kPa from a 20.7 MPa source tank (Airgas AR300), entered the enclosure via several 3.18 mm OD stainless steel tubes placed in the Duraboard® walls. Although mineral wool insulation was used to fill gaps between the walls, Ar continuously flowed out from the enclosure and a significant portion of the workpiece became oxidized over experiments lasting a total of ~5 h. Oxidized workpieces were replaced with new workpieces over the course of these experiments, and steady-state heat fluxes as great as 6.6 MW/m^2 were achieved with newer (*i.e.*, less oxidized) workpieces.
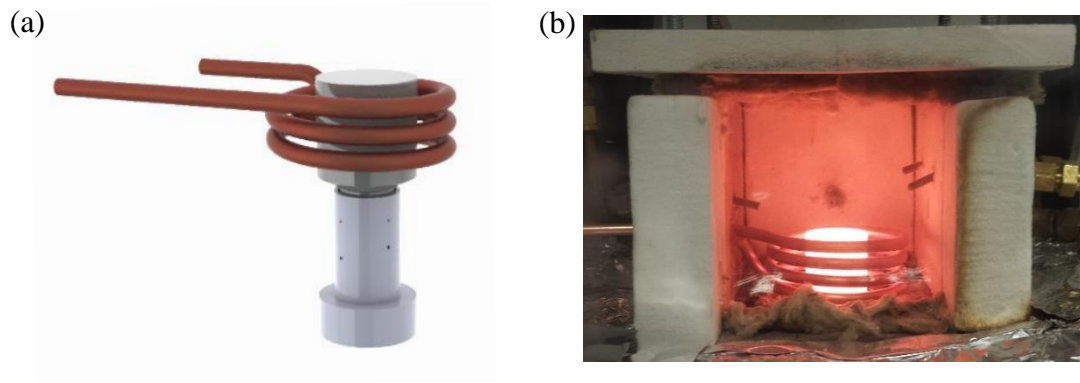
Figure 3.5. (a) Sketch of the induction heating setup above the outer shell and (b) picture of a heated workpiece inside the Argon-filled enclosure.

Further experiments were conducted using a sealed chamber designed to minimize oxidation (Figure 3.6). The chamber consisted of two 304 stainless steel vessels made from 30.48 cm (12 in.) Schedule 80 tubing with a standard 35.56 cm diameter flange welded to the rim of both vessels. The vessels were sealed to each other by using 30 bolts to compress a silver-plated Cu gasket between the flanges. The top vessel contains a 11.43 cm diameter viewport aligned with the top of the test section to allow visual inspection of the workpiece during an experiment.
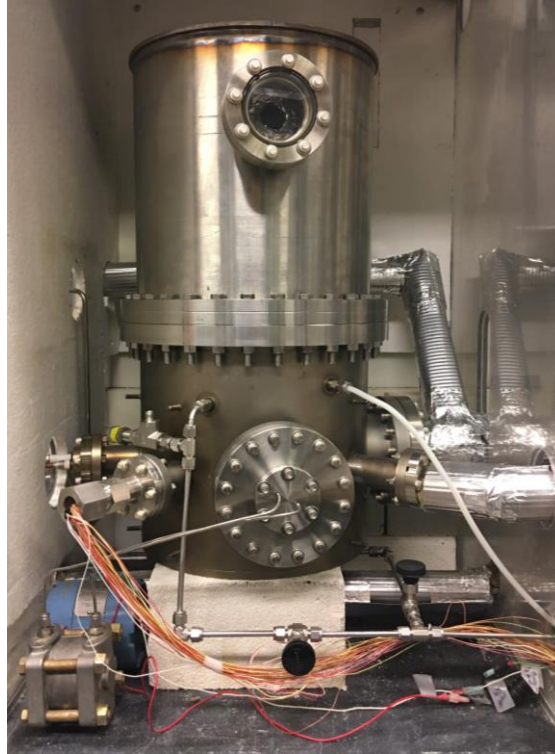
Figure 3.6. Picture of the steel sealed chamber (and the lower and upper vessels) designed to minimize oxidation of the inductively heated workpiece and test section.

All five feedthrough ports for the instrumentation were in the lower vessel so that the test section could be accessed by simply removing the top vessel. Four of these ports, with 6.98 cm diameter flanges, are for the inlet flow tubing, pressure sensor tubing, induction heater coil and electrical wires. The fifth port, with a 15.24 cm diameter flange, is for the outlet flow tubing. The three flanges used as tubing feedthroughs were directly welded to the tubing to prevent leaks. The induction coil feedthrough was purchased from Kurt J. Lesker Company (FTT0823253), while the wire feedthrough was custom made by Spectite, Inc. to contain 40 conductors for the thermocouples, RTDs, and pressure transducers. The lower vessel also contains an inlet port for the inert gas supply and an outlet port connected to a relief valve to keep the pressure inside the sealed chamber below 101 kPa (1 atm) to minimize the risk of damage to the viewport and the vacuum pump.

3.1.3 Helium Loop

The experiments reported here were conducted using the GT helium loop constructed by Mills in 2013 [32]. A schematic of the loop is depicted in Figure 3.7.
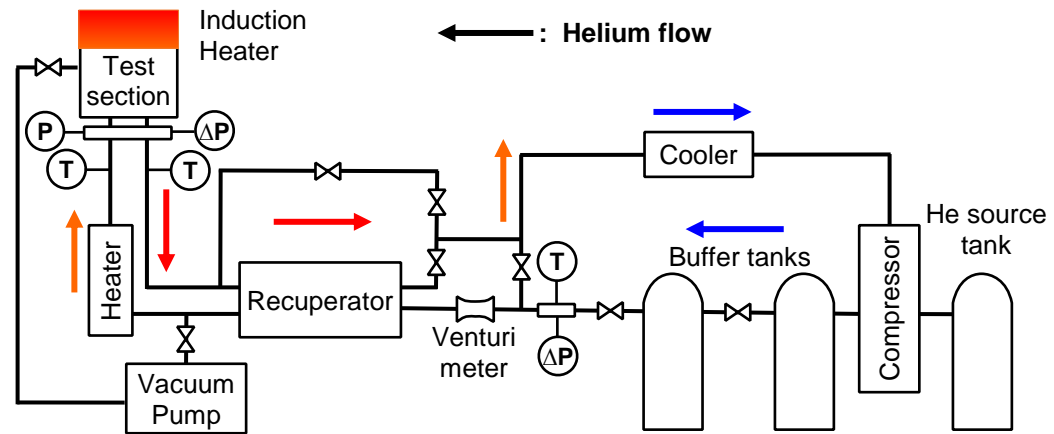
Figure 3.7. Schematic of the GT helium loop.

The loop operates with He at inlet pressures $p_i \approx 10$ MPa and inlet temperatures $T_i \leq 425$ °C for mass flow rates $\dot{m} \leq 10$ g/s. Before an experiment, most of the loop (except for the section containing the "buffer tanks") are evacuated using a vacuum pump (Thomas GH-605B), then charged to ~5 psi with He from the downstream buffer tank; the loop is evacuated and partially charged with He two more times to clean out the loop, then evacuated one last time. The buffer tanks are not evacuated because the He remaining in these tanks from previous experiments is used to reduce the amount of gas required to recharge the entire loop. After cleaning the loop, the He remaining in the buffer tanks is

used to charge the loop to ~9 MPa, and additional He from a 41.4 MPa source tank (Airgas HE HP6K) is used to increase the pressure to its nominal operating value of ~10 MPa.

A single-stage reciprocating compressor (Hydro-Pac C0.15-0.5-450LX) circulates the He through the loop. Helium exits the compressor (Figure 3.8) at room temperature and ~10 MPa, and flows through two 8.5 m^3 compressed-gas cylinders ("buffer tanks") that increase the inventory of He within the loop and reduce pulsations created by the reciprocating motion of the compressor pistons. A static pressure transducer (OMEGA PX309-2KGI) and type-K TC measure the pressure and temperature, respectively, of the He after it exits the second buffer tank and flows through a 140 μm particulate filter (Swagelok SS-8F-140).

Figure 3.8. Pictures of the front (left) and back (right) of the reciprocating compressor.

As depicted in Figure 3.9, a portion of the He flows through a 7 μm inline particulate filter (Swagelok SS-8F-7) in series with a main bypass valve (Swagelok SS-1RS4) used to control the helium mass flow rate and the pressure drop across the

compressor. The compressor pressure drop is kept below the maximum value of ~1.24 MPa recommended by the manufacturer.
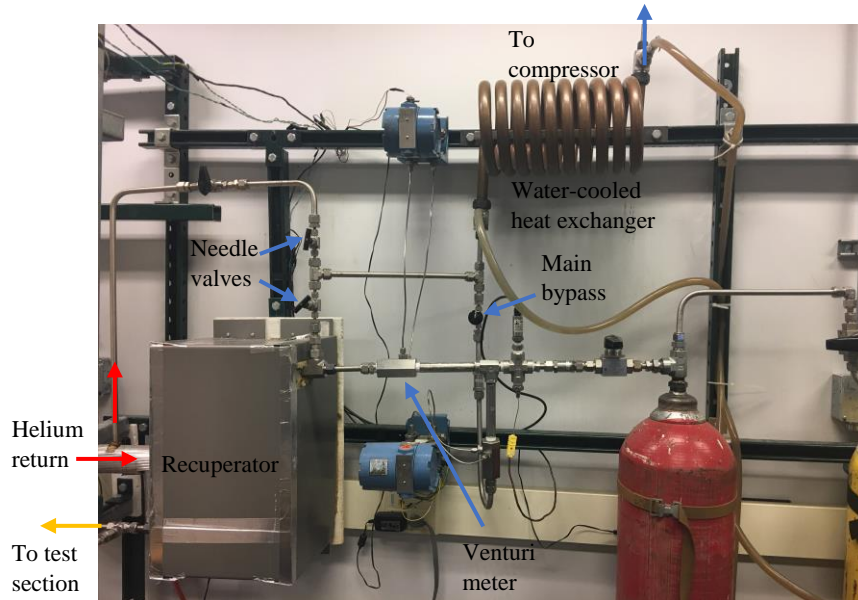
Figure 3.9. Picture of the room temperature section of the helium loop.

The remaining He flows through a venturi meter (Lambda Square V50-10) that measures the mass flow rate of the He downstream of the buffer tanks, which should then be the mass flow rate through the test section, barring any leaks. A differential pressure transducer (Rosemount 1151DP4E22) connected to the venturi meter measures the pressure drop across the meter, which is then used to determine the mass flow rate. The He then flows through a coil-in-coil counterflow heat exchanger (Sentry Equipment DTC-SSB/SSD-8-1-1), or "recuperator," where the heated He leaving the test section flows through the outer coil, pre-heating the room-temperature He flowing in the opposite direction in the inner coil. This pre-heated He is then further heated to the desired inlet temperature by two 4.5 kW cylindrical cartridge heaters (Tempco HDC01919) mounted

inside a 1 in Schedule 80 316 stainless steel pipe. Each heater has 35.6 cm long electrical leads with mica/glass insulation rated for temperatures up to 550 °C. Two electrical feedthroughs (Conax PL-14-A2-G) are used to connect the leads inside the tubing to a variable autotransformer that controls the power supplied to the cartridge heaters.

After removing heat from the HEMJ test section, the hot He flows through either the outer coil of the recuperator, or through a bypass line for experiments conducted at ambient temperature (Figure 3.9). Two needle valves (Swagelok SS-3NRS4-G) are used to control the flow path through the recuperator or bypass lines. Since the He flowing through these valves is at elevated temperatures, the bypass line contains an additional ball valve (Swagelok SS-H83PS4) used to isolate the hot He. This ball valve is closed when experiments are performed at $T_i > 100$ °C to reduce degradation of the high temperature Grafoil sealant within the bypass needle valve. The He leaving the recuperator or bypass lines merges with the flow through the main bypass, and flows through the inner coil of a water-cooled coil-in-coil heat exchanger. The outer coil is supplied with cold water from the building lines flowing at 1.26 m^3/s, which cools the He back down to nearly ambient temperatures to meet the maximum temperature requirements for the compressor.

Most of the loop piping is 12.7 mm (0.5 in) 304 stainless steel tubing with 1.24 mm (0.049 in) thick walls. Swagelok compression fittings made from 316 stainless steel are used for all pipe connections. The recuperator is heavily insulated with mineral wool and encased within a rectangular housing composed of sheet metal. The tubing between the test section and recuperator is also insulated with mineral wool. The heater assembly is insulated with layers of Duraboard® blocks bolted together to ensure good contact. Finally,

71

the tubing outside of the recuperator and heated region is not insulated since the coolant is at nearly room temperature in those locations.

3.2.   Experimental Methods and Results

3.2.1. Experimental Methods

In each single set of experiments with the helium loop, data were obtained at multiple values of $\dot{m}$ at a fixed H and T_i. After setting the separation distance H to its desired value, several sets of experiments were conducted by heating the He to a given T_i and increasing $\dot{m}$ from ~3 g/s to ~8 g/s. Detailed procedures for setting the separation distance and operating the loop are provided in Appendix A.

In all cases, steady-state is defined as a 5 min interval over which both the inlet and outlet temperatures vary by less than 0.5 °C. In most cases, these temperatures vary by less than 0.2 °C. Although the mass flow rate measurements have oscillations at the frequency of the reciprocating pistons in the compressor (~1 Hz), the amplitude of the oscillations is less than 5% of the time-averaged mass flow rate. The measured quantities (*i.e.*, $\dot{m}$, pressures, and temperatures) used in the subsequent calculations were all time-averaged over an interval of at least 180 s.

The He mass flow rate $\dot{m}$ is determined from the pressure drop measured across the venturi meter:

$$\dot{m} = CA_1 \sqrt{\frac{2\rho_v \Delta p_v}{(A_1/A_2)^2 - 1}} \qquad\qquad (3.1)$$

where ρ_v is the density of the coolant at the venturi meter inlet, Δp_v is the pressure drop between the smallest and largest inner diameters of the venturi meter, $A_1 = 196.0$ mm^2 and $A_2 = 26.3$ mm^2 are the larger and smaller cross-sectional areas, respectively, of the venturi meter, and $C = 0.8828$ is the flow coefficient of the meter, according to the manufacturer.

The mass flow rate is given in terms of the dimensionless Reynolds number based on the diameter of the central jet

$$Re = \frac{\rho V D_o}{\mu_i} = \frac{\dot{m} D_o}{A_j \mu_i} \tag{3.2}$$

where $D_o = 1.04$ mm is the central jet diameter of the HEMJ J1c design, $A_j = 7.64 \times 10^{-6}$ m^2 is the total cross-sectional area of the jets, and μ_i is the dynamic viscosity of He evaluated at the coolant inlet temperature T_i. The properties of He over a range of temperatures at a pressure of 10 MPa were obtained from the National Institute of Standard and Technology (NIST) [91].

The Reynolds number therefore depends on both $\dot{m}$ and T_i. At the prototypical mass flow rate $\dot{m}_p = 6.8$ g/s, the corresponding Reynolds number is $Re_p = 2.20 \times 10^4$ for $T_i = 600$ °C (*i.e.*, divertor modules located in 'Cooling Zone I' of a target plate, see Section 2.3.5). For divertor modules in 'Cooling Zone II', $Re_p = 2.14 \times 10^4$ based on $T_i = 634$ °C. The He loop can provide a maximum mass flow rate $\dot{m} = 10$ g/s, which corresponds to $Re < 6.72 \times 10^4$ for experiments conducted at room temperature ($T_i = 27$ °C) but only $Re < 3.88 \times 10^4$ for $T_i = 400$ °C.

The average incident heat flux incident on the test section is estimated from an energy balance on the He

$$\overline{q''} = \frac{\dot{m}c_p\left(T_o - T_i\right)}{A_h} \qquad (3.3)$$

where c_p is the constant-pressure specific heat evaluated at the average coolant temperature $T_{ave} = \left(T_i + T_o\right)/2$ and $A_h = 227$ mm^2 is the cross-sectional area of the outer shell. Thermal losses were assumed to be negligible in all cases, as detailed in Section 3.4

The temperature measurements from the four TCs nearest to the cooled surface are used to determine an area-weighted average of the entire cooled surface $\overline{T_c}$. The readings are first extrapolated to the four temperatures on the actual cooled surface $T_{c,r}$ assuming 1D conduction through ~0.5 mm of W-alloy

$$T_{c,r} = T_r + \frac{\overline{q''}\delta_{TC}}{k_s} \qquad (3.4)$$

where T_r is the TC reading (at the radial distance from the centerline in mm, r), δ_{TC} is the distance to the cooled surface, and k_s is the thermal conductivity of the outer shell evaluated at the average temperature of T_r and $T_{c,r}$ (which requires iteration). Temperature-dependent values of k_s for the WL10 test section are based on linear interpolation of data obtained by Roedig *et al*. [92] using the expression

$$k_{s,WL10}\left(T\right) = \left(3.372 \times 10^{-5}\right)T^2 - 0.1143T + 206.8 \qquad (3.5)$$

where T is the temperature in K. The thermal conductivity of the MT185 test section is linearly interpolated from

$$k_{s,MT185}(T) = (5.325 \times 10^{-8})T^3 - (1.261 \times 10^{-4})T^2 + 0.105T + 58.36 \qquad (3.6)$$

based on measurements taken at ORNL using the laser-flash method for temperatures ranging from ~25 °C to ~727 °C [32].

An expression for $\overline{T}_c$ is derived based on the extrapolated cooled surface temperatures using a CAD model of the WL10 outer shell

$$\overline{T}_{c,WL10} = 0.0169T_{c,0} + 0.1423T_{c,2.1} + 0.3181T_{c,4.2} + 0.5227T_{c,6.4} \qquad (3.7)$$

The TC at $r = 6.4$ mm has the greatest weight in this area average because the 2.3 mm radius fillet at the edge of the cooled surface results in a larger cooled area (*vs.* that for the central region). The TC locations in the extended MT185 outer shell were slightly different from those in the WL10 thimbles due to imperfections caused by EDM during the fabrication process. Hence, a separate area-weighted average cooled surface temperature expression $\overline{T}_{c,MT185}$ was derived after re-measuring the TC locations

$$\overline{T}_{c,MT185} = 0.0258T_{c,0} + 0.1587T_{c,2.1} + 0.3175T_{c,4.2} + 0.4980T_{c,6.4} \qquad (3.8)$$

The average HTC $\overline{h}$ is then

$$\overline{h} = \frac{\overline{q''}}{(\overline{T}_c - T_i)} \frac{A_h}{A_c} \qquad (3.9)$$

where $A_c = 184.2$ mm^2. The area-averaged Nusselt number over the cooled surface is

$$\overline{Nu} = \frac{\overline{h}D_o}{k_f} \qquad (3.10)$$

where k_f is the thermal conductivity of the fluid evaluated at T_{ave}. Eq. 3.3 assumes that all of the heat supplied at the heated surface is removed by convection at the cooled surface. However, previous experimental studies of finger-type divertors have shown that some of

the heat is removed by conduction along the divertor sidewalls [32]. As mentioned in Chapter 2, the correlations developed for $\overline{Nu}$ are therefore assumed to be only a function of Re and the thermal conductivity ratio κ. The effects of Pr on $\overline{Nu}$ were neglected since the Pr for He varies by less than 2% for temperatures ranging from 30 °C to 1200 °C.

The nondimensional pressure drop is given by the loss coefficient

$$K_L = \frac{\Delta p}{\frac{1}{2}\rho_L \overline{V}^2} \tag{3.11}$$

where ρ_L is the He density and $\overline{V}$ is the average velocity over all the jets. The He density is evaluated at T_i and p_o because numerical simulations of finger-type divertor modules suggest that most of the pressure drop occurs as the He exits the jet holes before impingement, and the fluid properties at these locations are best approximated when evaluated at the inlet temperature and outlet pressure. The loss coefficient represents the ratio of the static pressure drop across the jet holes to the dynamic pressure at the jet exit. If the dynamic pressure is evaluated at the inlet port, Eq. 3.11 would be equivalent to a pressure coefficient C_p typically used to express the pressure at any point in the flow.

3.2.2. Experimental Results

The results summarized here are from two sets of experiments covering 95 steady-state cases performed with different test sections and separations distances H. The first set of experiments were performed at nominal values of H of 0.50 mm, 0.90 mm, and 1.50 mm at $T_i \leq 300$ °C using a single 4 kW electric heater. Subsequent measurements with

air-dry clay showed, however, that the actual separation distances of these three configurations were $H = 0.44 \pm 0.03$ mm, 0.90 ± 0.02 mm, and 1.49 ± 0.03 mm, respectively. The extended MT185 test section was used for the experiments at $H = 0.44$ mm, while the shorter WL10 outer shell was used for $H = 0.09$ mm and 1.49 mm.

The second set of experiments was conducted after re-calibrating the differential pressure transducer on the extended WL10 test section for $T_i \leq 425$ °C with the new 9 kW heater at $H = 0.90$ mm. The test section was enclosed within the sealed chamber used to minimize oxidation and thermal losses, and experiments were performed at relatively low incident heat fluxes $\overline{q''} \leq 2.2$ MW/m^2 compared with the earlier experiments.

The experimental parameters for each value of H are summarized in Table 3.1. In all cases, the mass flow rate varied from ~3.0 g/s to 8.0 g/s, which spans the prototypical value $\dot{m}_p = 6.8$ g/s. The corresponding Reynolds numbers ranged from 1.2×10^4 to 5.4×10^4, vs. the prototypical value $Re_p = 2.2 \times 10^4$ at $T_i = 600$ °C.

Table 3.1. Summary of experimental parameters in this work.

W-alloy	H [mm]	H/D_j	T_i [°C]	$\overline{q''}$ [MW/m^2]
MT185	0.44	0.73	30 – 300	2.7 – 4.0
WL10	0.90	1.50	30 – 300	4.6 – 6.6
WL10	1.49	2.48	30 – 200	3.3 – 5.2
WL10	0.90	1.50	30 – 425	0.7 – 2.2

Figure 3.10 shows the results for the average HTC $\overline{h}$ for three different separation distances in the first set of experiments. The error bars represent the experimental uncertainty for $\overline{h}$ (details regarding the uncertainty calculations are given in Appendix D).

As expected, $\bar{h}$ increases with Re in all cases, with values ranging from $\bar{h} = 1.6 \times 10^4$ W/(m²·K) at $Re = 1.2 \times 10^4$ to $\bar{h} = 3.1 \times 10^4$ W/(m²·K) at $Re = 5.3 \times 10^4$. Interestingly, varying H has a negligible effect on heat transfer for the range of H values considered here. The $\bar{h}$ results at a given $\dot{m}$ are comparable for all four T_i since the He density (and hence Re) decreases at higher inlet temperatures.
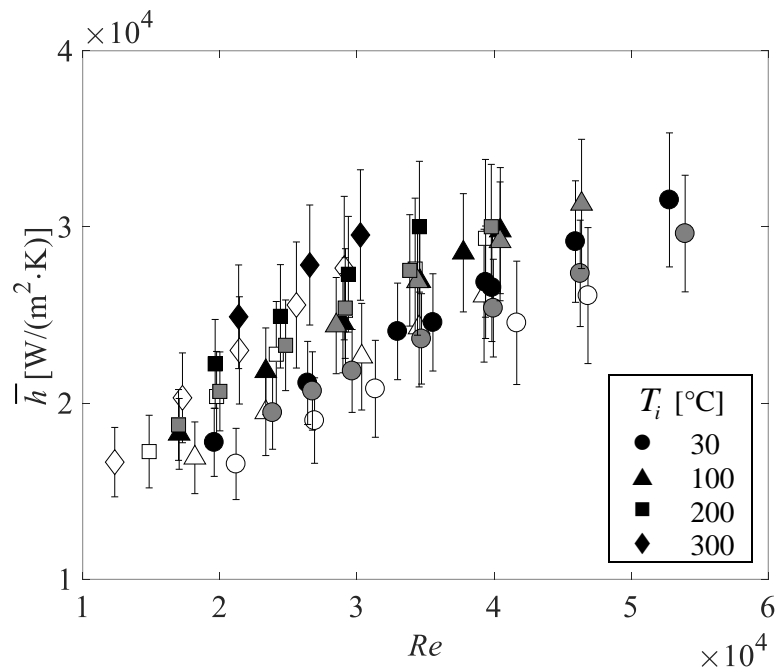
Figure 3.10. Average HTC $\bar{h}$ for three separation distances: $H = 0.44$ mm (open symbols), 0.90 mm (black symbols), and 1.49 mm (gray symbols).

Figure 3.11 shows the corresponding results for the average Nusselt number. At a given Re and H, the variations in $\overline{Nu}$ are within the experimental uncertainty for $T_i \leq 300$ °C, which suggests that thermal losses through the insulation was small compared to the incident thermal power and that most of the supplied thermal power is removed at the

cooled surface. Nevertheless, the $\overline{Nu}$ results at $T_i = 300\,°\text{C}$ also appear to be consistently

lower than those obtained at $T_i < 300\,°\text{C}$, especially for $H = 0.90$ mm and $H = 1.49$ mm.
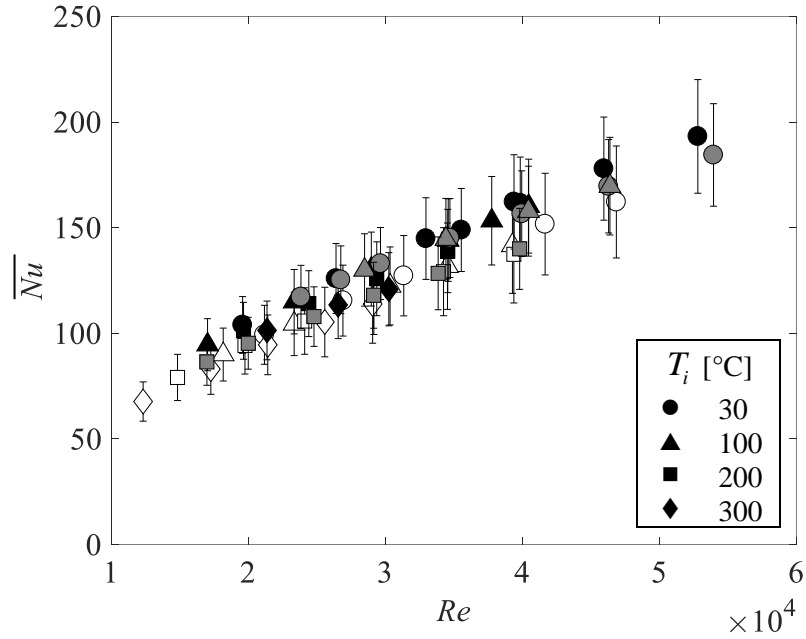
Figure 3.11. Average Nusselt number $\overline{Nu}$ for three different separation distances using the same legend as Figure 3.10.

These data agree with the results obtained by Mills [32] who used a thermal

conductivity ratio κ to account for this discrepancy with the following correlation:

$$\overline{Nu} = 0.085 Re^{0.59} \kappa^{0.19} \tag{3.12}$$

which is valid for:

$$\begin{bmatrix} 1.5 \times 10^4 \leq Re \leq 5.3 \times 10^4 \\ Pr \approx 0.7 \\ 347 \leq \kappa \leq 908 \end{bmatrix} \tag{3.13}$$

79

Inclusion of the thermal conductivity ratio in the Nusselt number correlation accounts for conduction effects (vis-à-vis convection) and is equivalent to inclusion of a Biot number as an independent variable in the correlation. The exponent for κ is based on the experimental results obtained by Rader [31] on an HEMJ module tested using coolants at room temperature and low pressures. Since Rader's correlations were valid for a larger range of κ ($\kappa \approx 340 - 7000$), the $\overline{Nu}$ correlation proposed by Mills is also assumed to have the form $\overline{Nu} \propto \kappa^{-0.19}$. Figure 3.12 compares Mills' correlation with these experimental data for $H = 0.44$ mm, 0.90 mm, and 1.49 mm.
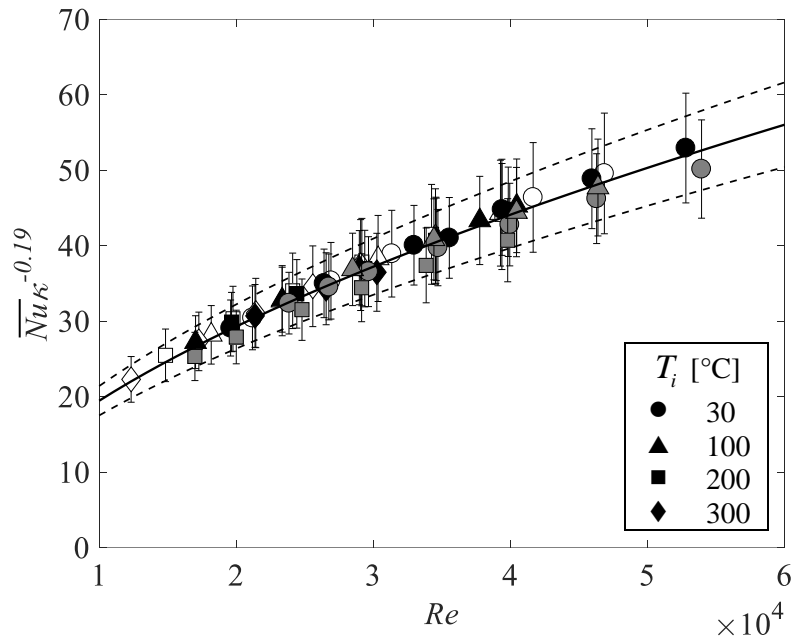
Figure 3.12. Comparison of the experimental data for $\overline{Nu}\kappa^{-0.19}$ as a function of Re and the correlation of 3.12. The dashed lines denote ±10% bounds on the correlation. The legend is identical to Figure 3.10.

The experimental data for $T_i \leq 300$ °C and these three H are within 10% of the correlation, which enhances confidence that this correlation can be used to predict the

thermal performance of the HEMJ at prototypical conditions. Including κ in the correlation for $\overline{Nu}$ reduces the variation in $\overline{Nu}$ at a given Re by ~20%. Again, varying H within this range appears to have a negligible effect on $\overline{Nu}$.

The results for the loss coefficient are shown in Figure 3.13 as a function of Re. In all cases, K_L is effectively constant and independent of Re over the range of Re studied here. The experimental results for $H = 0.44$ mm, 0.90 mm, and 1.49 mm give an average K_L of 3.12, 2.43, and 2.34, respectively. As expected, K_L was significantly higher for the cases at $H = 0.44$ mm.
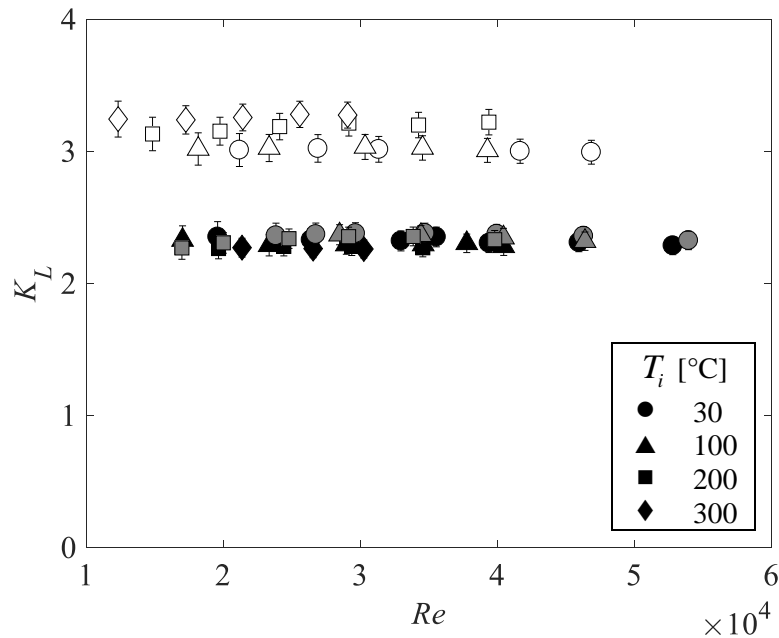
Figure 3.13. Loss coefficient K_L for three different separation distances using the same legend as Figure 3.10.

The scatter at $H = 0.44$ mm, where the K_L increase with T_i, is likely caused by a stronger influence of variations in H due to differential thermal expansion of the outer shell

81

and jets cartridge. However, the $\overline{Nu}$ results for this separation distance showed no enhancement compared with the results for $H = 0.90$ mm or 1.49 mm, which suggests that reducing H within this range will result in larger pressure drops, and hence coolant pumping power, but will not improve heat transfer rates.

After completing the first set of experiments, additional experiments were conducted, with a focus on further investigating the decrease in $\overline{Nu}$ observed at $T_i > 300$ °C for $H = 0.90$ mm. These experiments were performed using the sealed chamber filled with Ar (as described in Section 3.1.2) to minimize oxidation and thermal losses. These experiments were also conducted after re-calibrating the differential pressure transducer used to measure the pressure drop across the test section.

Figure 3.14 compares the $\overline{Nu}$ results for this second set of experiments at $T_i = 30$ – 425 °C with those obtained in the first set of experiments. The effect of T_i appears to be negligible for both sets of experiments (within a given set) except for the cases at $T_i = 300$ °C in the first set, and $T_i = 425$ °C in the second set; in other words, at the highest inlet temperature studied for both sets of experiments. Specifically, the results at $T_i = 425$ °C in the second set of experiments are consistently lower by 12% on average compared to those at $T_i < 400$ °C, although these results are within the experimental uncertainty in all cases. Interestingly, the $\overline{Nu}$ results for the second set of experiments are on average 18% higher compared to the results of the first set, although the heat fluxes are lower than those used for the earlier set of experiments. This discrepancy may be due to reduced thermal losses at the outlet.
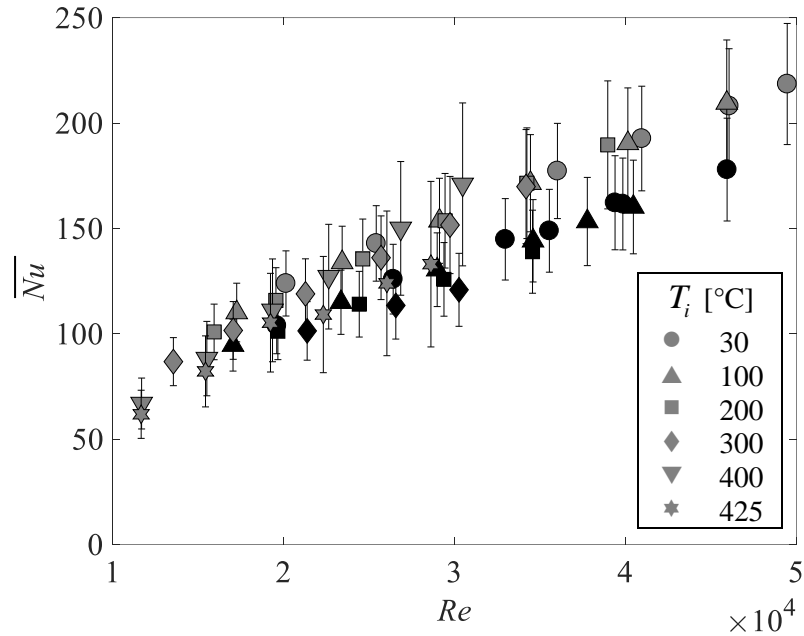
Figure 3.14. Comparison of the average Nusselt number $\overline{Nu}$ for the first (black symbols) and second (gray symbols) set of experiments at $H = 0.90$ mm.

Given that the results for the second set of experiments are consistently higher compared to those of the first set, a new correlation was developed based on the data obtained at all at T_i, including the results at $T_i \geq 400$ °C. Since only one test section material and coolant was studied here, $\overline{Nu}$ was again assumed to be proportional to $\kappa^{0.19}$. A curve-fit of these data using MATLAB R2017a yields the following correlation:

$$\overline{Nu} = 0.045 Re^{0.667} \kappa^{0.19} \tag{3.14}$$

which is valid for:

$$\begin{bmatrix} 1.1\times10^4 \leq Re \leq 4.9\times10^4 \\ Pr \approx 0.65 \\ 488 \leq \kappa \leq 1031 \end{bmatrix} \tag{3.15}$$

Figure 3.15 compares this new correlation with Eq. 3.12. The new HEMJ correlation gives a $\overline{Nu}$ that is 10% higher at $Re = 1 \times 10^4$, 15% higher at Re_p, and 26% higher at $Re = 5 \times 10^4$.
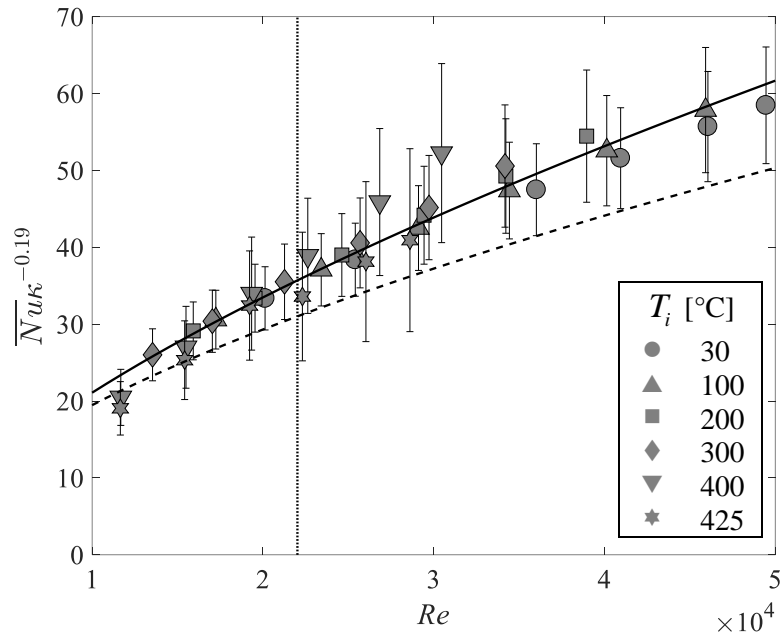
Figure 3.15. The $\overline{Nu}$ results and the new HEMJ correlation (black line) compared with the correlation of 3.12 (dashed line). The vertical dotted line denotes Re_p.

Figure 3.16 shows the results for the loss coefficient as a function of Re at $H = 0.90$ mm for the experiments performed before and after re-calibration of the differential pressure transducer.
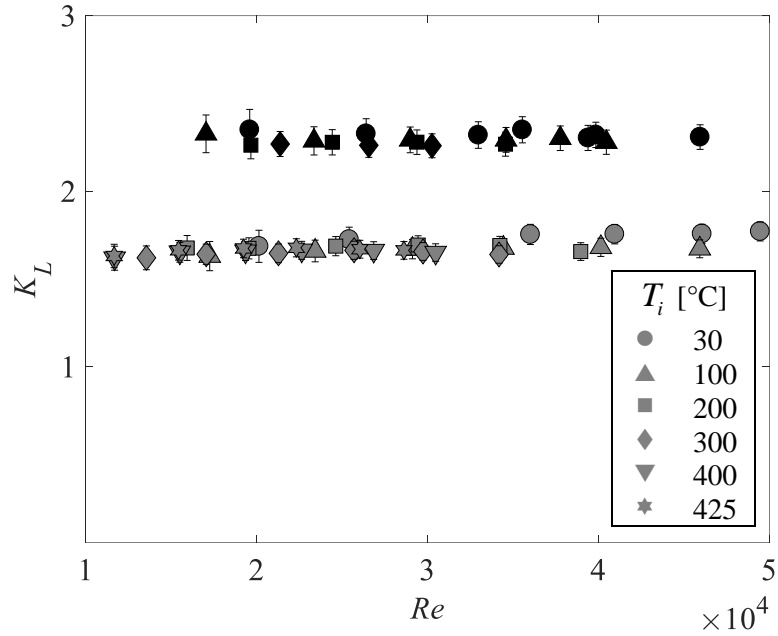
Figure 3.16. Loss coefficient K_L obtained before (black symbols) and
after (gray symbols) re-calibration of the differential pressure transducer.

In all cases, K_L is effectively independent of Re, though the K_L results after re-calibration

are significantly lower, and in good agreement with the numerical simulations as discussed

in Chapter 4. Hence, K_L for the HEMJ divertor was averaged over the entire range of Re

for the second set of experiments and assumed to be constant:

$$K_L = 1.68 \qquad (3.16)$$

3.3.   Prototypical Performance

The new correlation (Eq. 3.14) was used to estimate the thermal performance of the

HEMJ at typical operating conditions expected for a long-pulse magnetic fusion energy

reactor, such as DEMO. For a fixed Re, the maximum allowable heat flux at the pressure boundary was calculated from

$$\overline{q''_{\max}} = \frac{\overline{T_s} - T_i}{R_T} \quad \text{where} \quad R_T = \frac{A_h}{A_c \overline{h}} + \frac{\delta_s}{\overline{k_s}} \tag{3.17}$$

where $\overline{T_s}$ is the average maximum temperature of the W-alloy pressure boundary, R_T is the total thermal resistance, $\delta_s = 1$ mm is the thickness of the pressure boundary, and $\overline{k_s}$ is the thermal conductivity of the W-alloy evaluated at $(\overline{T_c} + T_s)/2$. The HEMJ thermal performance was investigated for two inlet temperatures $T_i = 600$ °C and 700 °C because the W-alloy DBTT is expected to increase with neutron irradiation effects. Moreover, the maximum heat flux was calculated for three maximum W-alloy temperatures $\overline{T_s} = 1100$ °C, 1200 °C, and 1300 °C (*i.e.*, the recrystallization temperature) for Re varying from 1×10^4 to 5×10^4 in intervals of 500.

Since $\overline{T_c}$ and T_o were initially unknown, κ was first calculated using Eq. 2.32 with estimated values for these temperatures. The HEMJ correlation was then used to calculate $\overline{Nu}$ from Eq. 3.14 at a fixed Re. Next, $\overline{h}$ was determined from Eq. 3.10 which allowed $\overline{q''_{\max}}$ to be determined from Eq. 3.17. Finally, $\overline{T_c}$ and T_o were calculated from Eq. 3.9 and Eq. 3.3, respectively, and compared with the initial estimates. An iterative procedure was used to achieve a convergence of 1×10^{-6} for the final values of $\overline{T_c}$ and T_o.

The coolant pumping power required at prototypical conditions was determined with a similar method. First, the average loss coefficient from the experiments was used to predict the pressure drop from Eq. 3.11. The pressure drop was calculated iteratively

since ρ_L depends on p_o. The converged value of Δp was then used to calculate the pumping power:

$$\dot{W} = \frac{\dot{m}(\Delta p)}{\overline{\rho}}$$

(3.18)

where $\overline{\rho}$ is the average of the He densities at T_i and T_o. The pumping power is normalized by the total incident thermal power:

$$\beta = \frac{\dot{W}}{q''_{max} A_h}$$

(3.19)

where $\overline{q''_{max}}$ was calculated for β = 5%, 10%, 15%, and 20%.

Figure 3.17 shows $\overline{q''_{max}}$ as a function of Re for a single HEMJ module at (a) T_i = 600 °C and (b) T_i = 700 °C. For a hexagonal tile with a flat to flat dimension of 18 mm, the ratio of the tile area to the heated surface area is A_T / A_h = 1.23. The maximum heat flux for the HEMJ test section must therefore be divided by this ratio to determine the true maximum heat flux that $\overline{q''_T}$ can be absorbed by the tile. At Re_p = 2.2×10⁴, T_i = 600 °C, and $\overline{T_s}$ = 1200 °C, the HEMJ module can accommodate a maximum heat flux of $\overline{q''_{max}}$ = 13.8 MW/m² ($\overline{q''_T}$ = 11.2 MW/m²) with β = 5%. Although these results are consistent with previous studies that suggest the HEMJ can accommodate $\overline{q''}$ = 10 MW/m² while keeping β < 10% [65, 76], the new correlation suggests that the tile can accommodate a ~0.7 MW/m² higher heat flux with a 2% lower pumping power at these conditions compared to the results obtained by Mills [32].
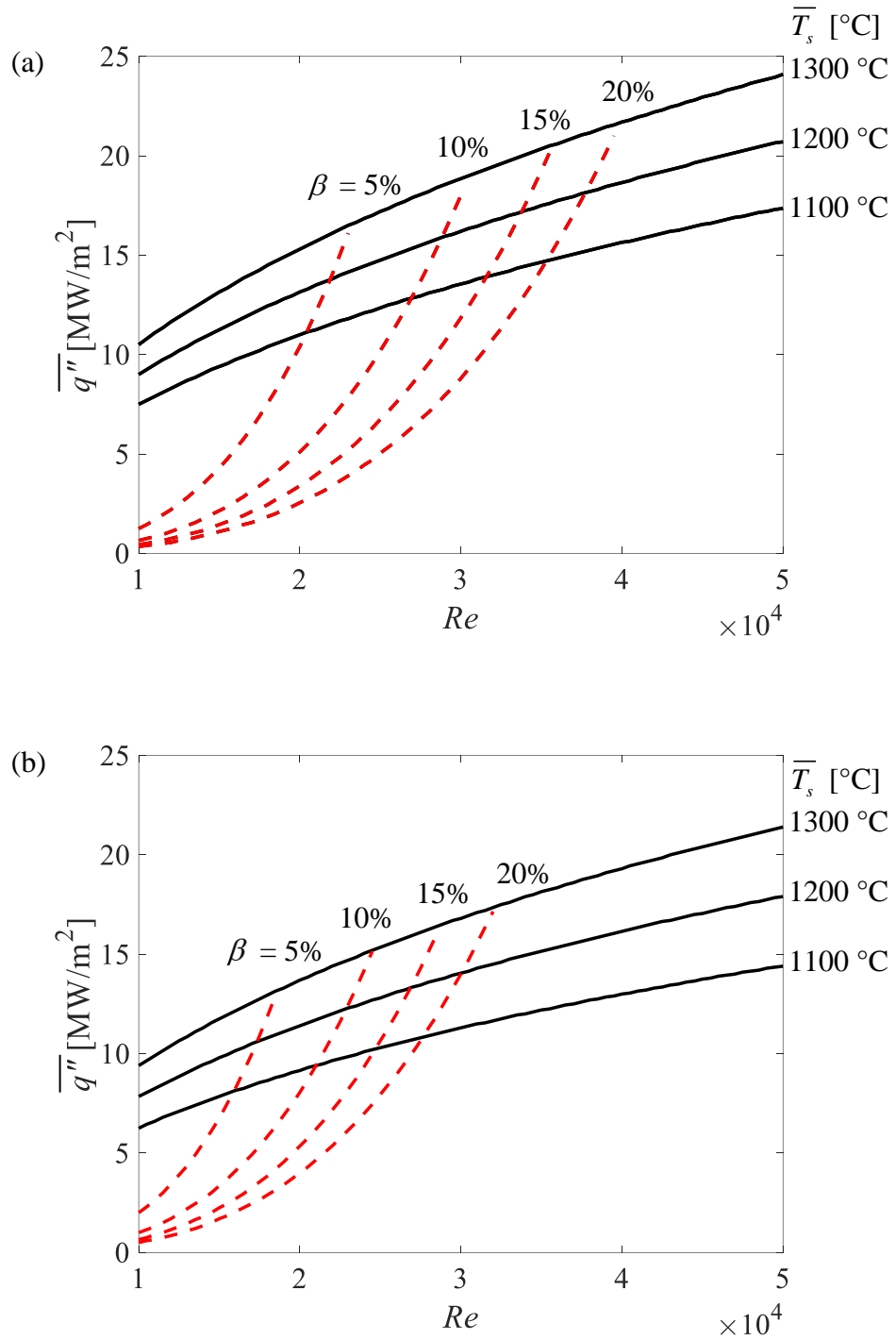
Figure 3.17. Maximum heat flux that can be absorbed by a single HEMJ module as a function of Re at (a) $T_i = 600\ °C$ and (b) $T_i = 700\ °C$.

If a higher coolant inlet temperature is required to avoid embrittlement of the W-alloy pressure boundary, it may be necessary to increase the mass flow rate to achieve the same thermal performance. Increasing T_i to 700 °C, for example, reduces $\overline{q''_{max}}$ to 12.0 MW/m² ($\overline{q''_T}$ = 9.72 MW/m²) with β = 9%, primarily due to a decrease in the He density. Table 3.2 summarizes the maximum heat flux limits and pumping power requirements at $\overline{Re_p}$ for T_i = 600 °C – 700 °C and $\overline{T_s}$ = 1100 °C – 1300 °C.

Table 3.2. Summary of the HEMJ thermal performance at $\overline{Re_p}$.

T_i [°C]	$\overline{T_s}$ [°C]	$\overline{q''_{max}}$ [MW/m²]	$\overline{q''_T}$ [MW/m²]	β [%]
600	1100	11.5	9.35	7
	1200	13.8	11.2	5
	1300	16.1	13.0	4.5
700	1100	9.65	7.81	11
	1200	12.0	9.72	9
	1300	14.4	11.7	8

3.4.   Thermal Losses and Radiation

To investigate the discrepancies in the $\overline{Nu}$ results at elevated temperatures, thermal losses from the test section were estimated using analytical, experimental, and numerical methods. The losses were first estimated analytically assuming one-dimensional, steady-state radial conduction using the thermal resistance method. The insulated test section assembly was modeled as the outer shell surrounded by two concentric cylinders exposed to ambient air. The cylinders represent the Marinite® and mineral wool insulation layers with effective radii based on the equivalent rectangular areas of the actual test section. The

area-averaged temperature of the outer wall of the thimble $\overline{T_w}$ was determined using simulation results based on a numerical model (discussed in Chapter 4) that includes the insulation. The geometry used for the analytical model and the corresponding thermal resistance network is depicted in Figure 3.18.
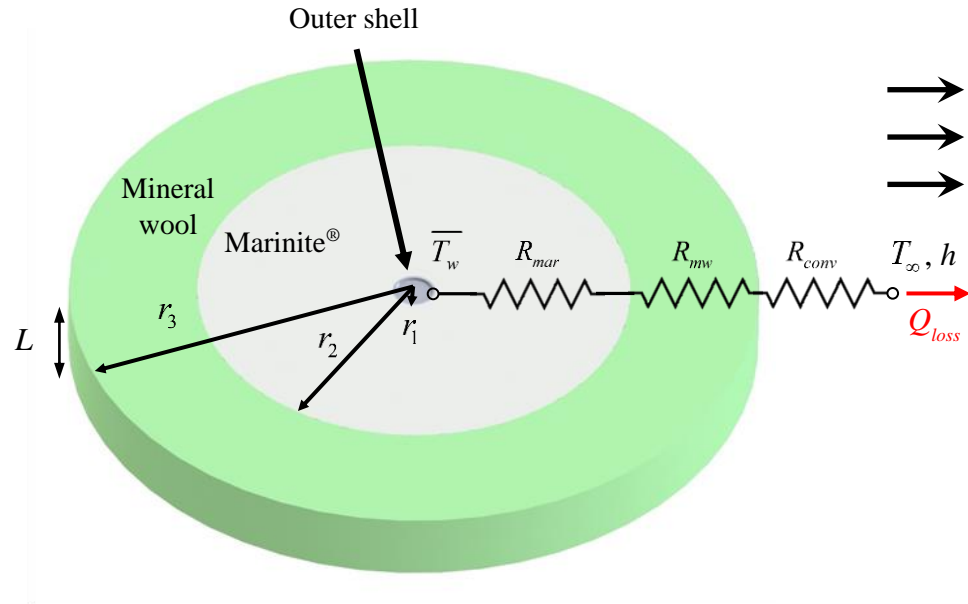
Figure 3.18. Thermal resistance network and geometry used for the 1-D thermal loss estimate.

The thermal energy due to losses through the insulation is then

$$Q_{loss} = \frac{\overline{T_w} - T_\infty}{R_{total}} \tag{3.20}$$

where $\overline{T_w}$ is the area-averaged temperature of the outer wall of the thimble, T_∞ is the ambient temperature assumed to be 25 °C, and $R_{total} = R_{mar} + R_{mw} + R_{conv}$ is the total thermal resistance from the Marinite®, mineral wool, and natural convection. The thermal resistances are given by

$$R_{mar} = \frac{\ln\left(\dfrac{r_2}{r_1}\right)}{2\pi k_{mar} L} \tag{3.21}$$

$$R_{mw} = \frac{\ln\left(\dfrac{r_3}{r_2}\right)}{2\pi k_{mw} L} \tag{3.22}$$

$$R_{conv} = \frac{1}{2\pi r_3 L h} \tag{3.23}$$

where $r_1 = 0.85$ cm is the radius of the outer shell, $r_2 = 8.6$ cm is the effective radius of the Marinite®, $r_3 = 13.6$ cm is the effective radius of the mineral wool, k_{mar} and k_{mw} are the thermal conductivities of the Marinite® and mineral wool (assumed to be 0.12 W/(m·K) and 0.1 W/(m·K)), respectively, $L = 27.8$ mm is the length of the outer shell, and h is a uniform natural convective HTC conservatively assumed to be 15 W/(m²·K).

A typical high inlet temperature case with (Re, T_i, $\overline{q''}$) values of (2.5×10^4, 300 °C, 5.2 MW/m²) was first considered since thermal losses are presumably higher at these conditions. The one-dimensional conduction analysis results in a heat loss of ~2.9 W through the insulation, which was less than 1% of the total incident power $Q_i \approx 1173$ W for this case. A detailed CFD model that includes both layers of insulation and convection to the environment was then developed and used to simulate the same case. The resulting heat loss was 2.7 W, which agrees with the analytical estimate.

The thermal resistance network approach was also used to estimate thermal losses based on experimentally measured temperatures. Two TCs were placed at the outer surface of the Marinite® to determine an average temperature for an experiment conducted with (Re, T_i, $\overline{q''}$) values of (2.4×10^4, 250 °C, 4.0 MW/m²). A CFD model that simulated the

same flow conditions was used to determine $\bar{T}_w$. The heat loss was then estimated using a thermal resistance network through the Marinite® insulation layer based on the following equation

$$Q_{loss} = \frac{2\pi k_{mar} L\left(\bar{T}_w - \bar{T}_{mar}\right)}{\ln\left(\dfrac{r_2}{r_1}\right)} \tag{3.24}$$

where $\bar{T}_{mar} \approx 152\ °C$ is the average temperature of the Marinite® measured by TCs. The resulting heat loss based on the one-dimensional conduction analysis was ~2.4 W for this case, which was again less than the total incident thermal power $Q_i \approx 909$ W. Moreover, this value agrees with a 2.5 W heat loss predicted by the simulations. These results suggest that thermal losses through the insulation are negligible, including experiments at high T_i.

Thermal losses at the outlet port have a greater effect on $\overline{Nu}$ since T_o is directly proportional to $\overline{q''}$ (from a coolant energy balance). The discrepancy in the $\overline{Nu}$ between the first and second set of experiments is therefore likely due to reduced thermal losses at the outlet from the use of the sealed Ar chamber. The chamber effectively eliminated any convection to the ambient environment, resulting in only conduction through the low thermal conductivity insulation.

The fraction of the thermal energy leaving the cooled surface due to radiation was also analytically estimated for two cases: thermal emission solely from the cooled surface, and radiation exchange between the cooled surface and jet nozzle. In the first case, the total emissive power from the cooled surface was calculated using:

$$Q_{rad} = A_c \varepsilon \sigma \bar{T}_c^{\,4} \tag{3.25}$$

where ε is the total, normal emissivity of pure W evaluated at $\overline{T}_c$ and $\sigma = 5.67 \times 10^{-8}$ W/(m$^2 \cdot$K^4) is the Stefan-Boltzmann constant. Temperature-dependent values for ε were obtained from [93]. The largest $\overline{T}_c$ observed in the HEMJ experiments was ~677 °C, which corresponded to (Re, T_i, $\overline{q''}$) values of (1.15×10^4, 400 °C, 2.9 MW/m^2) and $\varepsilon = 0.11$. The resulting emissive power $Q_{rad} = 0.77$ W is ~0.1% of the total incident power $Q_{in} = 655$ W for this case, which suggests that thermal emission from the cooled surface is negligible.

Radiation exchange between the cooled surface and the jet nozzle was also estimated assuming radiation between two diffuse surfaces in an enclosure, which is a conservative assumption since radiation from the cooled surface reaches additional surfaces in the impingement region. The thermal energy due to radiation was calculated from:

$$Q_{12} = \frac{\sigma(T_1^4 - T_2^4)}{\dfrac{1-\varepsilon_1}{\varepsilon_1 A_1} + \dfrac{1}{A_1 F_{12}} + \dfrac{1-\varepsilon_2}{\varepsilon_2 A_2}} \tag{3.26}$$

where the subscripts 1 and 2 denote the cooled surface and jet nozzle, respectively, the view factor F_{12} was assumed to be 1, $A_2 = 129$ mm^2 is the area of the jet nozzle, and $\varepsilon_2 \approx$ 0.4 was obtained from [93]. A high heat flux experiment with (Re, T_i, $\overline{q''}$) values of (1.96×10^4, 30 °C, 5.5 MW/m^2) was considered where $T_1 = 411$ °C was the average cooled surface temperature and $T_2 = 61$ °C was the area-averaged temperature of the jet nozzle obtained from a corresponding simulation. Solving for the radiative exchange yields Q_{12} = 0.12 W, which is a negligible amount of the total incident power. This thermal energy is actually removed by the incoming helium and is therefore included in the energy balance.

In summary, the thermal performance of the HEMJ divertor was experimentally investigated for $p_i \approx 10$ MPa, $T_i \leq 425$ °C, and $\overline{q''} \leq 6.6$ MW/m^2 at three different separation distances. Correlations were developed for $\overline{Nu}$ and K_L, and extrapolated to predict the thermal performance at prototypical conditions. These results were then used to validate a numerical CFD model developed in ANSYS® Workbench™. The numerical model and simulation results are discussed in detail in the next chapter.

CHAPTER 4: NUMERICAL SIMULATIONS

A numerical model was developed to complement the experimental studies of the HEMJ-like divertor performed at nearly prototypical conditions. Steady-state CFD and FEM numerical simulations with one-way coupling were performed on a three-dimensional model of the HEMJ test section. Given that the experiments can only measure a limited set of thermal-hydraulic parameters, this numerical model can, with appropriate experimental validation, provide insight into physical parameters that are inaccessible in the experiments. Moreover, this validated model can be used to predict the thermal performance of the divertor at fully prototypical conditions, which is not possible with the current facility. It can also be used to optimize the geometry of the divertor and quantify the sensitivity of divertor performance to manufacturing tolerances and changes in dimensions. These coupled simulations can also provide estimates of dimensional changes due to differential thermal expansion, which are important for the range of H values considered in the HEMJ divertor.

4.1. HEMJ Model

The 3D numerical model of the HEMJ test section (Figure 4.1) was created with ANSYS® Workbench™ 17.0. The model geometry consisted of a 60° "wedge" of the W-alloy outer shell, the jets cartridge, and the He confined within this region. The validity of modeling a wedge (*vs.* a full model) is discussed in Section 4.2. The WL10 thimble was assumed to have a constant density $\rho_{WL10} = 1.91 \times 10^4$ kg/m^3, a temperature-dependent

specific heat c_p^{WL10} estimated by linear interpolation of tabulated values in the ITER Materials Properties Handbook [94], and thermal conductivity given by Eq. 3.5. The steel cartridge was assumed to have a constant density $\rho_{steel} = 8 \times 10^3$ kg/m^3 and temperature-dependent thermal conductivity k_{steel} and specific heat c_p^{steel} obtained from linear interpolation of tabulated values [95]. Finally, the helium was assumed to be an ideal gas with properties at 10 MPa obtained from NIST [91].

Steady-state simulations were performed with boundary conditions based on experimentally measured values. A constant and uniform mass flux and coolant temperature were specified at the inlet based on experimentally determined values of $\dot{m}$, T_i, and the cross-sectional area of the inlet port. The He pressure and temperature at the outlet were specified as p_o and T_o, while a constant heat flux $\overline{q''}$ was specified at the heated surface. Symmetry boundary conditions were imposed on the faces on the two sides of the wedge, while adiabatic boundary conditions were imposed on the other outer walls.
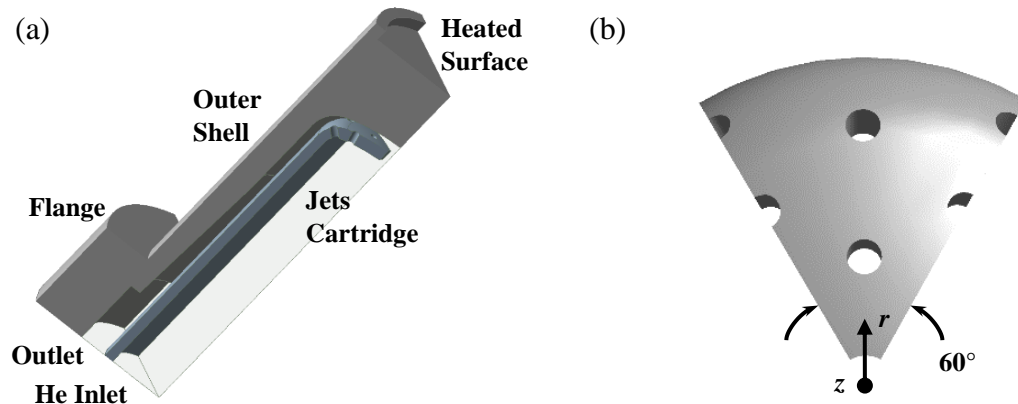
Figure 4.1. (a) Geometry of the HEMJ-like numerical model, and (b) end view of the jets cartridge projected along the axis of symmetry.

Mesh convergence studies were performed by reducing the maximum element size in the fluid to ensure that the numerical mesh was fine enough for the predictions to be essentially independent of mesh dimension. A structured hexahedral mesh was created using ANSYS® ICEM® with grid refinement at the solid/fluid interface such that the mesh dimension normal to the surface was less than one wall unit along the inner surface of the thimble (Figure 4.2). Mesh convergence studies were performed for numerical models ranging from ~4×10⁶ to ~8×10⁶ elements for a case with (Re, T_i, $\overline{q''}$) values of (2.0×10⁴, 100°C, 3.6 MW/m²) using the standard k-ε turbulence model with enhanced wall treatment available in ANSYS® Fluent®.
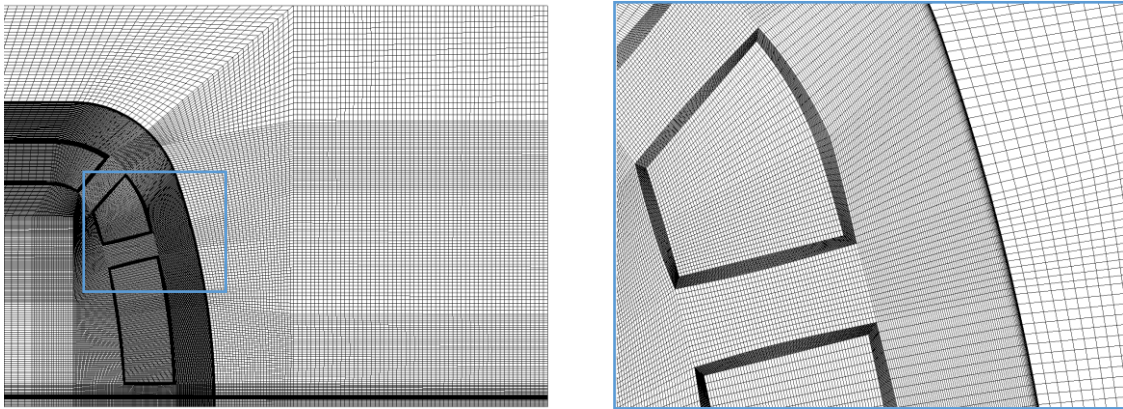
Figure 4.2. Picture of the ~6×10⁶ element mesh at one plane (left) and a closer view of the impingement region (right)

For the standard k-ε model, the turbulence kinetic energy k and turbulence dissipation rate ε were defined at the inlet and outlet using the following equations:

$$k = \frac{3}{2}\left(V_{avg}I\right)^2 \qquad (4.1)$$

97

$$\varepsilon = C_\mu^{3/4} \frac{k_t^{3/2}}{l} \tag{4.2}$$

where V_{avg} is the average velocity, I is the turbulence intensity, and l is the turbulence length scale defined as follows:

$$V_{avg} = \frac{\dot{m}}{\rho A} \tag{4.3}$$

$$I = 0.16 \left(Re_{D_h} \right)^{-1/8} \tag{4.4}$$

$$l = 0.07 D_h \tag{4.5}$$

Here, the inlet and outlet areas of the HEMJ test section A_i = 71.5 mm^2 and A_o = 102.4 mm^2, respectively, ρ is the He density determined from the ideal gas law, and Re_{D_h} is the Reynolds number based on the hydraulic diameters of the inlet (9.54 mm) and the outlet (4.81 mm). As discussed in Chapter 2, C_μ is an empirical constant assumed to be 0.09.

As metrics for mesh convergence, the numerical predictions for the local and area-averaged cooled surface temperatures were compared to the experimental results. Given that the local cooled surface temperature distribution is non-uniform, the simulation results for the nodal temperatures over the cooled surface were fitted to a sixth order polynomial for three different meshes. Figure 4.3, which compares $T_c(r)$ for each mesh, shows that the local cooled surface temperature distribution is essentially the same for the ~6×10^6 and ~8×10^6 element meshes. The predicted $\overline{T_c}$ was within ~3 °C of the experimental value of $\overline{T_c}$ = 314 °C for all three models. The ~6×10^6 element mesh was therefore used in the rest

of these simulations because of its more rapid convergence, with a typical convergence time less than 3 h.
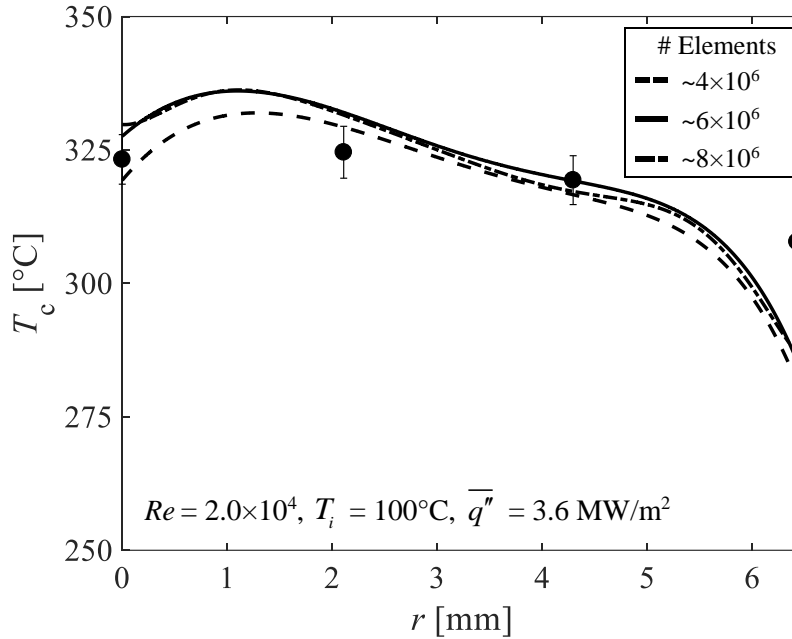
Figure 4.3. Radial profiles of the cooled surface temperature comparing the experimental measurements (●) with numerical predictions for three meshes using the standard $k\text{-}\varepsilon$ model.

To determine an appropriate turbulence model for the HEMJ divertor simulations, six of the turbulence models available as standard options in the software, namely Spalart-Allmaras, standard $k\text{-}\omega$, shear stress transport (SST) $k\text{-}\omega$, standard $k\text{-}\varepsilon$, realizable $k\text{-}\varepsilon$, and renormalization group (RNG) $k\text{-}\varepsilon$ were evaluated. The Spalart-Allmaras, standard $k\text{-}\omega$, and SST $k\text{-}\omega$ models require specifying various parameters at the inlet and outlet boundaries. For the Spalart-Allmaras model, the modified turbulent kinematic viscosity $\tilde{\nu}$ was defined as:

$$\tilde{v} = \sqrt{\frac{3}{2}} V_{avg} Il \qquad (4.6)$$

For the standard k-ω, and SST k-ω models, the specific dissipation rate ω was defined from the relationship:

$$\omega = \frac{k^{1/2}}{C_\mu^{1/4} l} \qquad (4.7)$$

These models were tested for a case with (Re, T_i, $\overline{q''}$) values of (2.0×10^4, 100°C, 4.3 MW/m²) at $p_i \approx 10$ MPa. The TC temperatures extrapolated to the cooled surface were directly compared to the numerical predictions for a radial profile of the cooled surface temperatures fitted to a sixth-order polynomial. Figure 4.4 compares the cooled surface TC measurements with the predictions obtained using the six turbulence models.
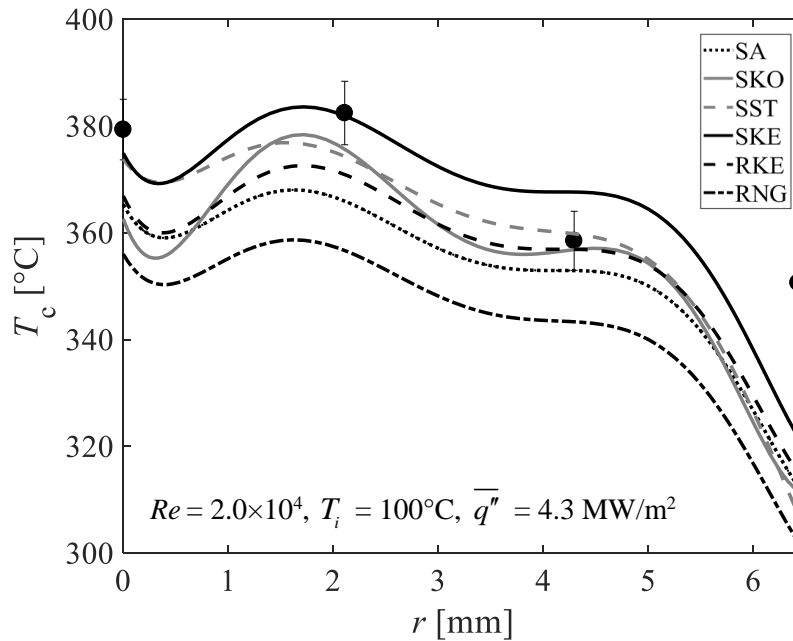
Figure 4.4. Radial profiles of the cooled surface temperature comparing the experimental measurements (●) with numerical predictions using a mesh of ~6×10^6 elements for six turbulence models.

All six turbulence models give similar cooled surface temperature distributions. As expected, the region near the stagnation points of the impinging jets have lower temperatures, while the regions between the jets have higher temperatures.

The experimental results for the area-averaged cooled surface temperature $\overline{T_c} = 358\ °C$ was then compared with that predicted by the six different turbulence models. The difference between the numerical and experimental values for $\overline{T_c}$ were $\Delta T = 14\ °C$, 11 °C, 12 °C, 1.3 °C, 11 °C and 24 °C for the S-A, standard and SST k-ω, and standard, realizable and RNG k-ε models, respectively (where the numerical values were less than the experimental values in all cases). Since the predictions from the standard k-ε model had the smallest ΔT, this model was used for the rest of the simulations presented here.

4.2. Symmetry Considerations

Given that the flow distribution in the impingement region may not be symmetric despite the six-fold symmetry of the actual HEMJ geometry, simulations were performed to verify the accuracy of the temperatures predicted by a numerical model based on a 60° symmetric wedge. To this end, a full model of the HEMJ test section was developed and used to simulate a case with (Re, T_i, $\overline{q''}$) values of (2.6×10^4, 30 °C, 5.9 MW/m²) based on the experiments. Mesh convergence studies were performed using the standard k-ε model on meshes containing $\sim7\times10^6$, $\sim15\times10^6$, and $\sim20\times10^6$ tetrahedral elements with grid refinement near the solid/fluid boundaries. The $\sim15\times10^6$ and $\sim20\times10^6$ meshes gave $\overline{T_c} = $ 364 °C, a value within 8 °C of the measured value $\overline{T_c} = 372\ °C$ and within 5 °C of the

value predicted by the simulation of the 60° wedge $\overline{T_c}$ = 369 °C. Additional simulations

were performed with the wedge for six cases where 371 °C < $\overline{T_c}$ < 423 °C, giving $\overline{T_c}$

predictions with an average deviation of 4 °C compared to the experiments. This suggests

that the wedge-based model can provide accurate cooled surface temperature predictions

with fewer elements and hence, less computational time, than a full model.

The outer shell temperature distributions were then compared to further investigate

any possible discrepancies between the two models. Figure 4.5 shows contour plots of the

temperature distribution in the outer shell for the same case described above. The

maximum and minimum temperatures in the outer shell differ by only 6 °C and 4 °C,

respectively, between the two models. Moreover, the temperature distributions are

qualitatively similar for both models, which provides additional confidence that the 60°

wedge can accurately simulate the thermal performance of the HEMJ test section, even if

the flow distribution may not be symmetric.
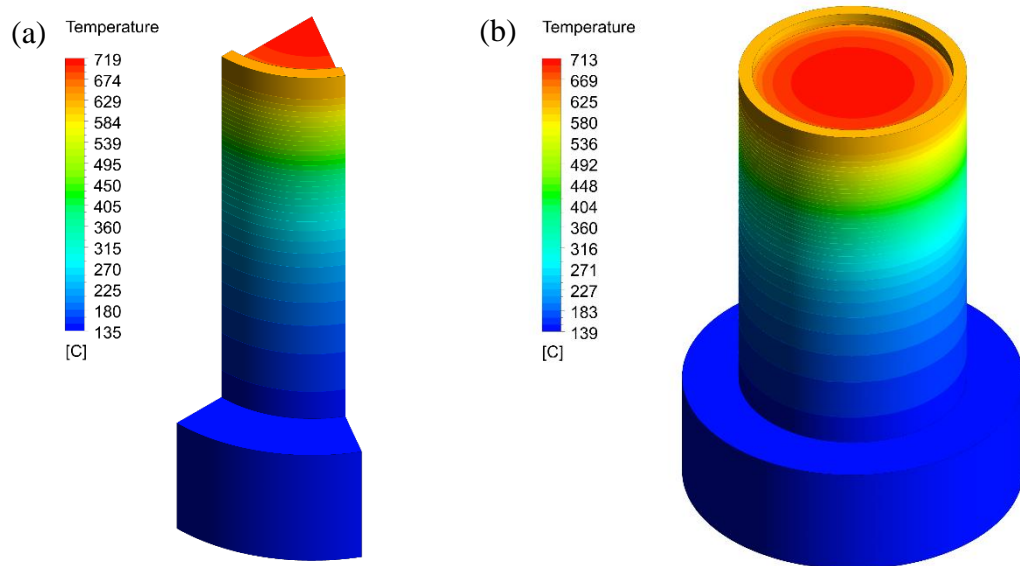
Figure 4.5. Temperature contours in the outer shell for the (a) 60° wedge and (b) the full HEMJ model at Re = 2.6×10^4, T_i = 30 °C, and $\overline{q''}$ = 5.9 MW/m^2.

The full model can, however, provide insight into the amount of temperature variations in the azimuthal direction. Figure 4.6 shows a contour plot of the local cooled surface temperature distribution, and the radial temperature profiles spaced by 15° in azimuth (θ). These temperature profiles should be similar along radii aligned with jet holes that have periodic symmetry.
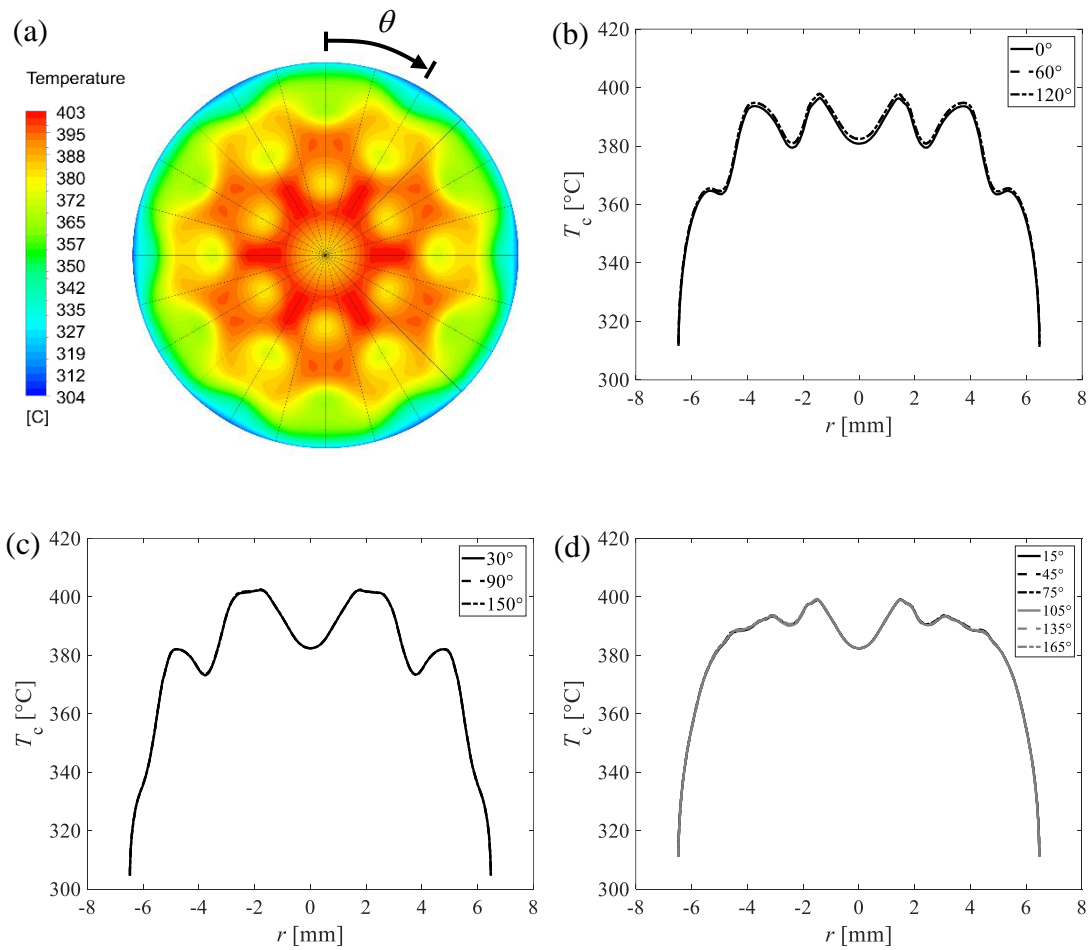
Figure 4.6. (a) Cooled surface temperature distribution for $Re = 2.6{\times}10^4$, $T_i = 30$ °C, and $\overline{q''} = 5.9$ MW/m^2 using the full HEMJ model. The black lines represent the radii where local temperatures were extracted at different azimuthal angles θ spaced 15° apart. (b)-(d) Radial temperature profiles for $\theta = 0 - 180°$.

The local maximum and minimum temperatures for the radii aligned with the jet holes located at $\theta = 0°$, $60°$, and $120°$, for example, differ by less than 2 °C (Figure 4.6). The temperature distributions for $\theta = 30°$, $90°$, and $150°$ are also nearly indistinguishable, with maximum nodal temperature differences of less than 3 °C and an average temperature deviation of 1 °C. These results suggest that azimuthal temperature variations at the cooled surface are effectively negligible for locations with periodic symmetry. Since the full model required significantly more mesh elements (and computational time) to achieve convergence, the wedge-based model was used for all of the subsequent HEMJ simulations in this work.

4.3.   Incident Heat Flux Uniformity

In the experiments, it is impractical to measure the incident heat flux distribution on the heated surface of the test section. The numerical simulations were therefore used to investigate how non-uniform incident heat fluxes may affect the thermal performance of the HEMJ test section using the same case described above. Four different non-uniform incident heat flux profiles were investigated. In all cases, a Gaussian distribution was used with the same total thermal power Q_i, with different peak-to-average heat flux ratios:

$$F = \frac{q_0''}{\overline{q''}} \tag{4.8}$$

Here, F is the ratio of the peak heat flux q_0'' to the average heat flux $\overline{q''}$ (*i.e.*, "peaking factor"); four values of F, namely $F = 1$, 2, 3, or 4 were evaluated. The incident heat flux spatial distribution is given as a function of radial position on the heated surface r by

$$q''(r) = \overline{q''}\, \frac{\alpha}{\zeta\sqrt{2\pi}}\, e^{-\frac{r^2}{2\sigma^2}} \qquad (4.9)$$

where α and ζ are a spreading coefficient and scaling factor to ensure the same Q_i, respectively. The parameters chosen for the four different cases considered here are given in Table 4.1 and the four corresponding radial incident heat flux profiles normalized by $\overline{q''}$ on the heated surface are shown in Figure 4.7.

Table 4.1. Parameters for incident heat flux uniformity study.

F	α	ζ
1	–	–
2	0.02370	0.00473
3	0.02672	0.00355
4	0.03022	0.00301
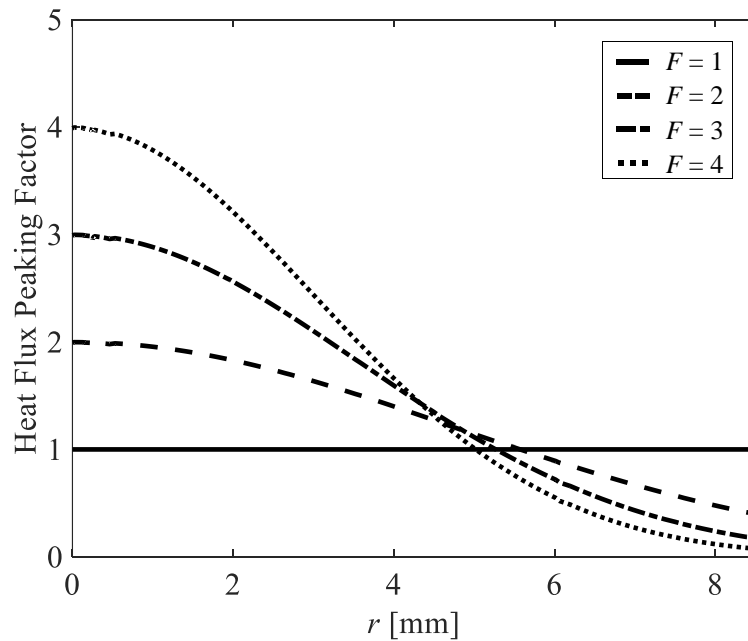
Figure 4.7. Normalized incident heat flux profiles on the heated surface along one radial plane for $Re = 2.6\times10^4$, $T_i = 30\ °C$, and $\overline{q''} = 5.9\ \mathrm{MW/m^2}$.

The resulting cooled surface temperatures for the four heat flux profiles are shown in Figure 4.8. The cooled surface temperatures are very similar for all four cases, even for the case at $F = 4$. The maximum temperature difference is 12 °C, which occurs near the stagnation point. However, the temperature distribution becomes nearly identical for $r \geq$ 3.5 mm for all four cases. Moreover, $\overline{T_c}$ for the cases with a non-uniform incident heat flux differed by less than 1 °C compared with the case with a uniform incident heat flux. The thickness of the solid "tip" region (which models the W tile in the J1c design) allows for enough conduction such that even a highly non-uniform incident heat flux profile has a negligible effect on the cooled surface temperatures.
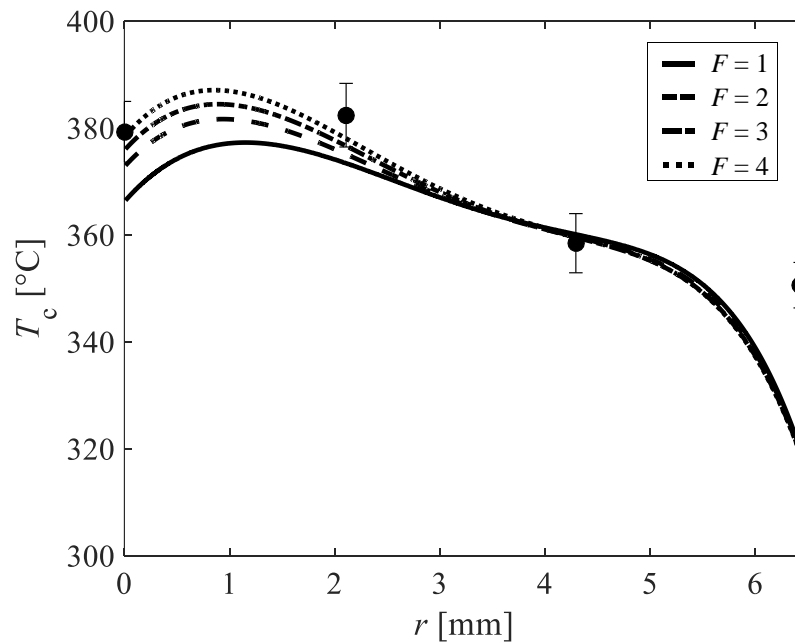
Figure 4.8. Cooled surface temperatures comparing the experimental measurements (●) with the simulations predictions for four different incident heat flux profiles at $Re = 2.6 \times 10^4$, $T_i = 30$ °C, and $\overline{q''} = 5.9$ MW/m^2.

Given that the incident heat flux in the experiments is likely more uniform than a Gaussian profile with a peaking factor of four, these simulation results suggest that a uniform average incident heat flux is a reasonable assumption for the numerical model and that the effect of a non-uniform incident heat flux on the experimental values for area-averaged cooled surface temperatures $\overline{T}_c$ is negligible..

4.4.   Simulation Results

The simulations were validated by simulating the second set of experiments conducted using the metal chamber and re-calibrated pressure transducer at $1.1 \times 10^4 < Re < 4.9 \times 10^4$, 30 °C $\leq T_i \leq 425$ °C, 0.75 MW/m² $\leq \overline{q}'' \leq 2.2$ MW/m², and $H = 0.90$ mm. The area-averaged cooled surface temperatures $\overline{T}_c$ extracted from the simulation results were used to calculate $\overline{h}$ and $\overline{Nu}$ based on Eq. 3.9 and Eq. 3.10, respectively. The average deviation in $\overline{T}_c$ between the experiments and simulation predictions was 3.4 °C. The $\Delta\overline{T}_c$ was less than 7 °C in all cases, except for a single case at $T_i = 425$ °C that had a $\Delta\overline{T}_c = 11$ °C for $\overline{T}_c = 468$ °C. The simulation predictions for Δp were used to calculate K_L using Eq. 3.11. Figure 4.9 compares the experimental values and numerical predictions for $\overline{Nu}$ and K_L for 36 cases.
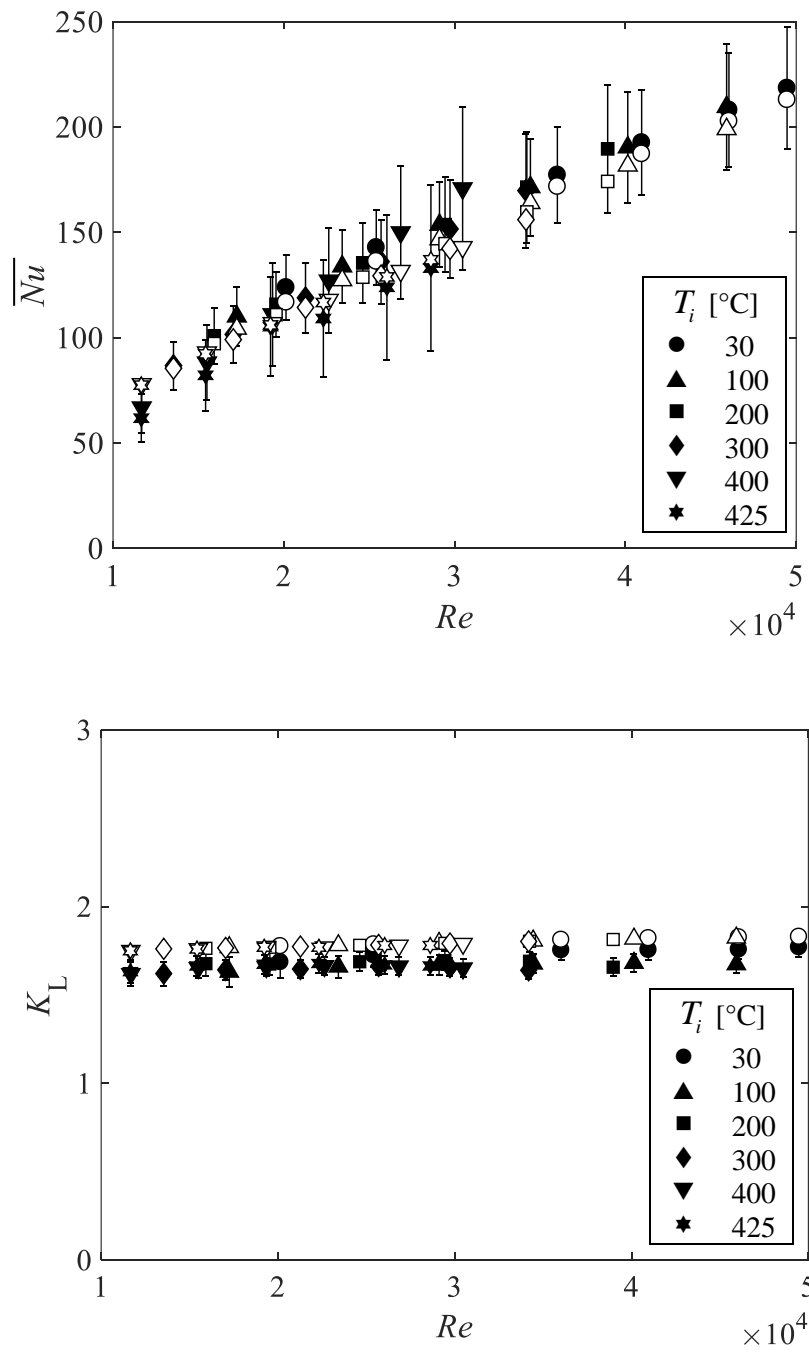
Figure 4.9. Comparison of the $\overline{Nu}$ (top) and K_L (bottom) results obtained from the experiments (filled symbols) and the simulations (open symbols) at $H = 0.90$ mm

The numerical predictions for $\overline{Nu}$ and K_L are in good agreement with the experimental results, with maximum differences of 6.2% and 6.7%, respectively, when averaged over this range of Re. Moreover, the simulation results are also effectively independent of T_i and $\overline{q''}$, suggesting that the model can be extrapolated to predict the divertor performance at prototypical conditions with reasonable accuracy.

The simulations enable access to local parameters that are difficult to measure experimentally, such as the amount of thermal energy removed at the cooled surface (*vs.* the amount conducted along the wall). Figure 4.10 shows the fraction of thermal energy removed by convection at the cooled surface as a function of Re for the 36 cases described above. The inlet temperature has a weak effect on the amount of convection at the cooled surface, which is significantly less than 100%.
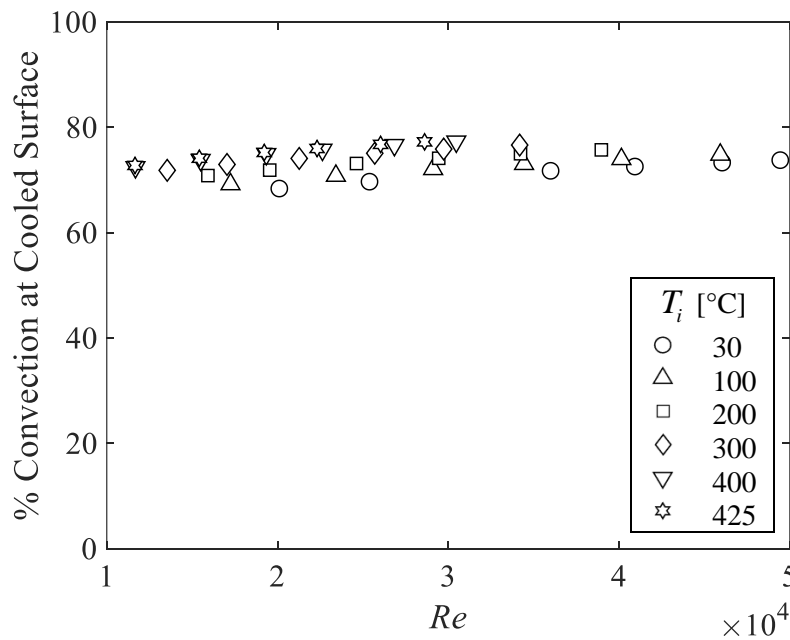
Figure 4.10. Fraction of total incident thermal power that is removed at the cooled surface by convection for the HEMJ test section at $H = 0.90$ mm.

However, these results suggest that the fraction of heat convected to the coolant at the cooled surface is effectively independent of Re and accounts for ~74% of the total incident thermal energy when averaged over this range of Re for all six T_i. The remaining thermal energy is removed by conduction through the sidewalls. As described in [32], the thermal conductivity ratio κ is used to account for the remaining fraction of thermal energy in the test section.

The numerical model was next used to simulate the HEMJ at prototypical conditions. Simulations were performed for $T_i = 600$ °C and $\overline{q''} = 10$ MW/m² for Re ranging from 1×10^4 to 5×10^4 in intervals of 5000; an additional case was simulated at the prototypical value Re_p. The inlet $\dot{m}$ boundary condition was calculated using Eq. 3.2, and the outlet pressure p_o was set to 10 MPa.

Figure 4.11 shows contour plots of the local cooled surface temperature distribution and static pressure of the He for $p_i \approx 10$ MPa, $T_i = 600$ °C and $\overline{q''} = 10$ MW/m² at Re_p. The maximum temperature $T_{max} = 1597$ °C occurs at the outer edge of the heated surface and exceeds the RCT of WL10, but remains within the 2500 °C design limit. The area-averaged cooled surface temperature and HTC are $\overline{T_c} = 945$ °C and $\overline{h} = 35.7$ kW/(m²·K), respectively. The combination of He (which has very high c_p for a gas) and multiple impinging jets enables cooled surface HTCs that rival values typically produced by forced convection with liquids or convection with phase change. At steady-state, most of the pressure drop occurs as the He enters the jet holes due to the vena contracta effect, where the flow velocity rapidly increases and the pressure decreases.
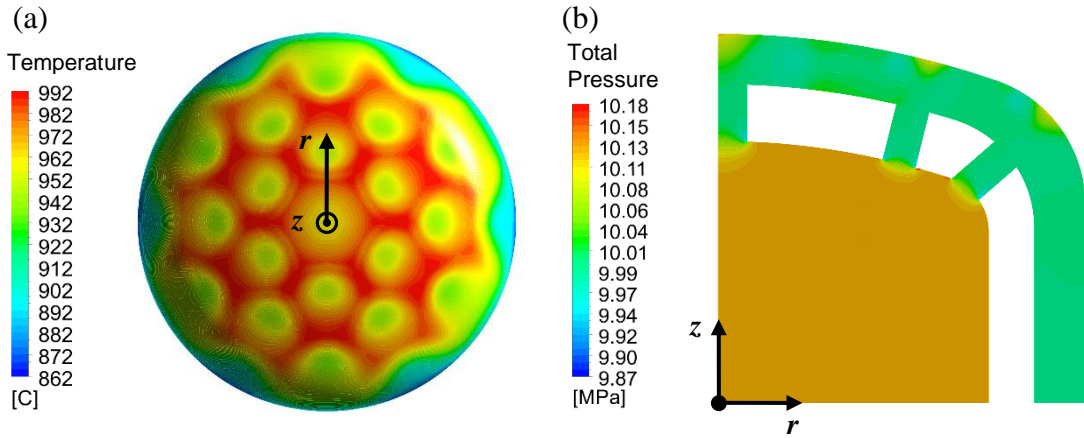
Figure 4.11. End view of the (a) cooled surface temperature distribution and (b) the static pressure of the He in the impingement region at one radial plane for $p_i \approx 10$ MPa, $T_i = 600$ °C, and $\overline{q''} = 10$ MW/m² at Re_p.

At each Re, average Nusselt numbers and loss coefficients were then calculated based on the numerical results for $\overline{T_c}$ and p_i, respectively. Numerical predictions for κ were also calculated using the results for $\overline{T_c}$ and T_{ave} to determine the values of $\overline{Nu\kappa}^{-0.19}$.

Figure 4.12 compares the simulation predictions for $\overline{Nu\kappa}^{-0.19}$ with the new correlation (Eq. 3.14). The two curves are nearly indistinguishable, with a maximum difference of 1%. The simulation predictions for K_L were nearly constant and gave an average $K_L = 1.79$, which is within 6.7% of the experimental value. These results enhance confidence that the correlation of Eq. 3.14 can be extrapolated to higher T_i and $\overline{q''}$ with reasonable accuracy. It should be noted, however, that these simulation results do not yet account for differential thermal expansion at elevated temperatures, which is discussed in the next section.

111
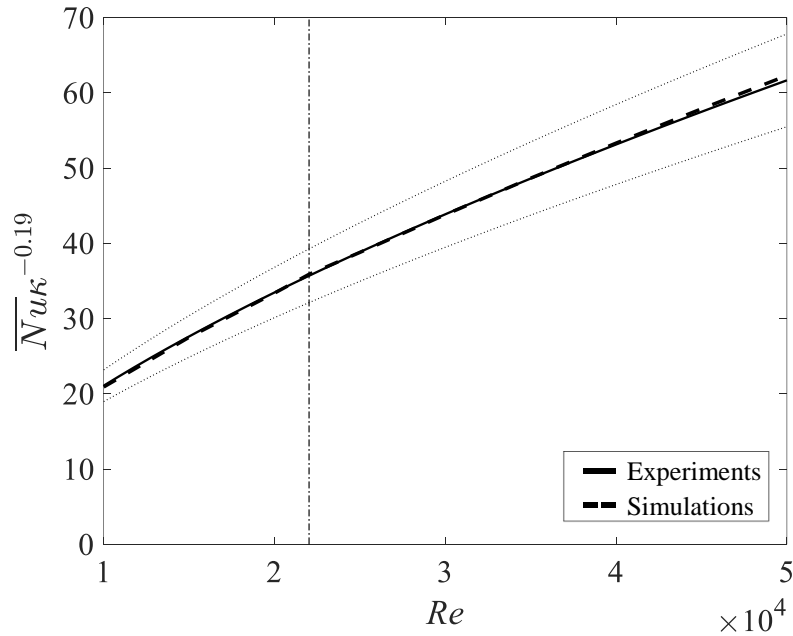
Figure 4.12. Average Nusselt numbers based on experimental (solid line) and numerical (dashed line) results. The dotted lines represent ±10% bounds on the correlation of 3.14. The vertical dash-dotted line denotes Re_p.

Given that the space available for TC probes within the outer shell is limited, only a few temperature measurements can be obtained within the outer shell in the experiments. Hence, the simulation results were used to investigate the maximum temperature in the test section, and the local maximum and minimum temperatures on the cooled surface (*i.e.*, pressure boundary). Figure 4.13 shows these temperature predictions for the HEMJ test section at T_i = 600 °C, $p_i \approx$ 10 MPa, and $\overline{q''}$ = 10 MW/m² as a function of *Re*. The maximum and minimum cooled surface temperatures fall between the DBTT and RCT of WL10, which satisfies the requirements of the HEMJ J1c design. Although the maximum temperature of the outer shell is above the RCT for all of the *Re* considered here, T_{max} is well below the 2500 °C design limit. The greatest maximum temperature T_{max} = 1837 °C occurs at $Re = 1 \times 10^4$ while the lowest T_{max} = 1438 °C at $Re = 5 \times 10^4$. Recent tests of both

112

W and WL10 suggest that exceeding the RCT may result in a significant loss of strength, even without neutron irradiation [96, 97]. Nevertheless, these results suggest that the HEMJ design can remain within all expected temperature limits over a wide range of *Re*.
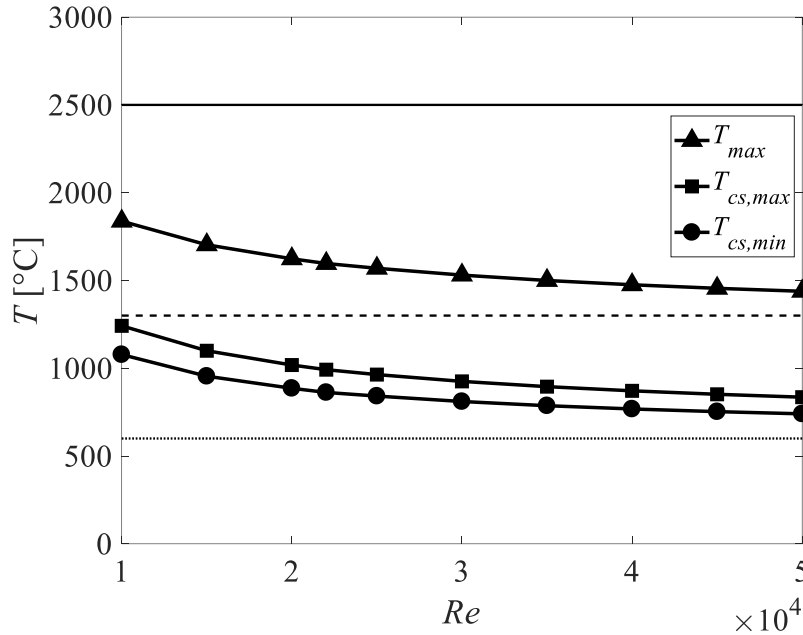
Figure 4.13. Simulation predictions for the maximum temperature in the HEMJ outer shell, and the maximum and minimum temperatures on the cooled surface at prototypical conditions. The lines represent the WL10 DBTT (dotted) and RCT (dashed), and the design limit for the W tile (solid).

4.5.   Thermo-Mechanical Evaluation

The extremely high heat fluxes incident on the divertor target plates result in elevated W/WL10 temperatures, and hence significant thermal stresses. Although several groups have performed thermo-mechanical simulations of the HEMJ and other finger-type divertors to characterize these stresses [28, 90, 98], the effects of thermal expansion, specifically differential expansion due to the different materials comprising the HEMJ,

have not yet been reported. The numerical model of the HEMJ test section was therefore extended to include a structural analysis using the steady-state FEM solver in ANSYS® Workbench™ 17.0.

For the structural analysis, the fluid domain was suppressed while the solid domains were modeled and meshed using $\sim 1.3 \times 10^6$ tetrahedral elements. The nodal temperatures and pressures predicted by the CFD simulations were interpolated onto the new mesh in the outer shell and jets cartridge, and at the solid/fluid interfaces, respectively. Fixed and frictionless constraints were applied over the bottom surface of the jets cartridge, and the top and bottom faces of the flange based upon the physical constraints on the actual HEMJ model tested in our helium loop. Finally, cyclic symmetry was applied to the periodic faces to completely define the model.

The FEM analysis produced a deformed mesh that was used to create an updated version of the HEMJ geometry with ANSYS® SpaceClaim®. This geometry was then re-meshed and a second CFD analysis was performed to account for the effects of thermal expansion on the fluid flow. The full simulation workflow for the CFD/FEM model is shown in Figure 4.14.

Figure 4.14. Workflow for the thermo-mechanical numerical model with one-way CFD/FEM coupling.

Figure 4.15 shows the local von Mises stress σ_v distribution over the cooled surface and the thermally-induced expansion of the HEMJ test section at prototypical conditions and Re_p. The highest local stresses occur in the curved regions near the stagnation points of the outer row of impinging jets. The maximum local stress was compared to the $3S_m$ criterion of Sec. III of the ASME Boiler and Pressure Code [99], where S_m is the design stress intensity. The $3S_m$ value at $\overline{T_c}$ is ~387 MPa based on linear interpolation of temperature-dependent values by reported by Norajitra [28]. Although the stresses over the majority of the cooled surface are well below the $3S_m$ limit, the locations with maximum stresses σ_v^{max} nearly exceed $3S_m$, which suggests that the reliability of divertor modules may be less than originally expected at prototypical conditions.
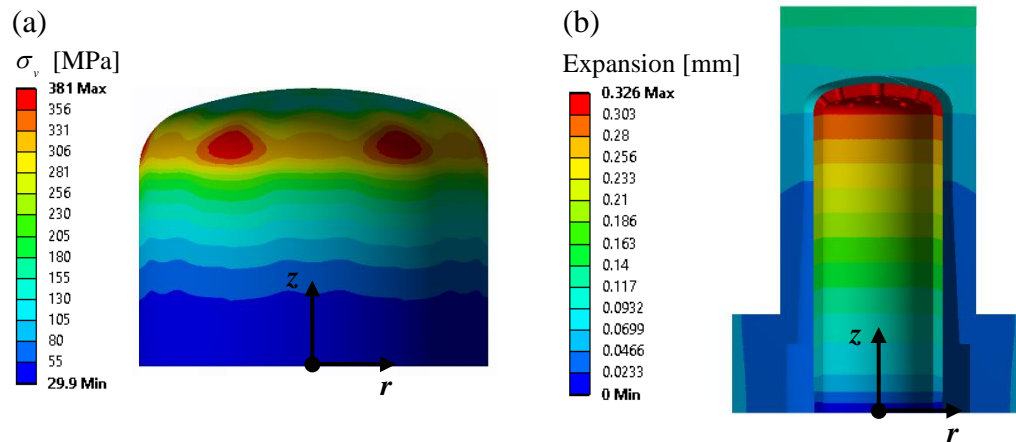
Figure 4.15. Diametric cross-sections of the (a) cooled surface von Mises stress distribution and (b) thermal expansion of the HEMJ test section for $p_i \approx 10$ MPa, $T_i = 600$ °C, and $\overline{q''} = 10$ MW/m^2 at Re_p.

The FEM simulations also suggest that the gap between the jets cartridge and the cooled surface H is reduced by ~0.23 mm due to the difference in the thermal expansions

of the AISI 304 stainless steel and the WL10. The steel expands by ~0.32 mm (due to a

higher coefficient of thermal expansion, CTE) compared to an expansion of ~0.09 mm by

the WL10.   While these dimensional changes are negligible in many engineering

applications, this reduction in H is significant for He-cooled finger-type divertors that

typically have separation distances of $O(1 \text{ mm})$. For the HEMJ design, H is reduced by

~25% compared to its initial value at ambient temperature.

A second series of CFD simulations were performed on the deformed HEMJ

geometry at prototypical conditions for Re ranging from 1×10^4 to 5×10^4 (including the case

at Re_p) using the same flow boundary conditions as the initial set of simulations. Figure

4.16 shows the simulation predictions for $\overline{Nu}$ based on the undeformed and deformed

HEMJ geometry (due to thermally induced expansion).
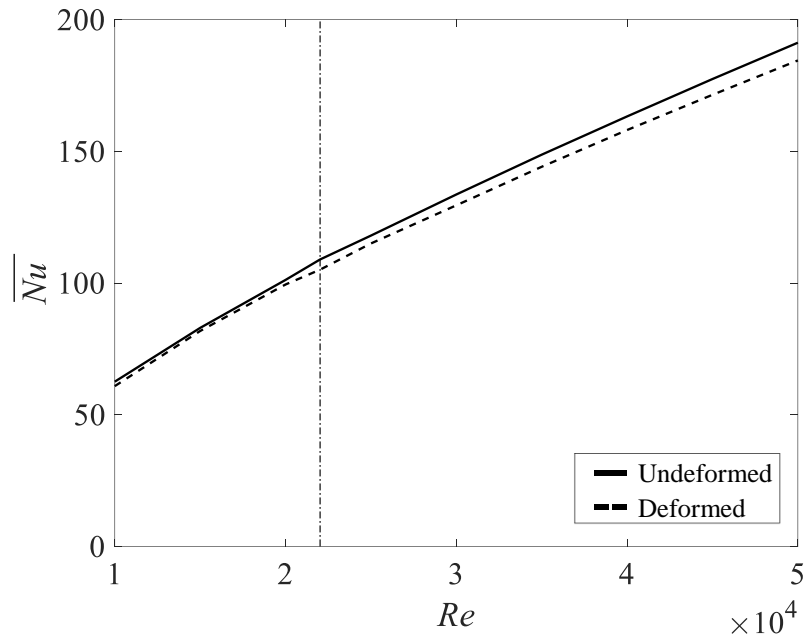
Figure 4.16. Simulation predictions of $\overline{Nu}$ for the undeformed HEMJ and the
deformed geometry due to thermal expansion at prototypical conditions. The vertical
dash-dotted line denotes Re_p.

The deformed geometry gives $\overline{Nu}$ that are consistently lower by 2.8% when averaged over this range of Re, which may be due to a decrease in the average velocity through the slightly enlarged inner diameter of the jets cartridge. At prototypical conditions, the simulations suggest that the ID of the jets cartridge expands by ~0.1 mm.

The loss coefficients averaged over this range of Re $K_L = 1.62$, which differs from the experimental value by 3.6%. The results from the thermo-mechanical simulations suggest that geometric changes due to differential thermal expansion have a small effect on both $\overline{Nu}$ and K_L, which further enhances confidence that the correlation can be accurately extrapolated to prototypical conditions.

CHAPTER 5: JET ARRAY OPTIMIZATION

Although the HEMJ divertor has been shown to provide superior thermal-hydraulic

performance compared the HEMP and HEMS divertors [28], the complex geometry of the

cooled surface and jet nozzle make accurate manufacturing a challenge, especially in pure

W and W-alloys. Thermo-mechanical simulations were therefore performed on different

variants of the HEMJ using the numerical model described in Chapter 4 to determine if

comparable, or even superior, thermal-hydraulic performance was possible with a simpler,

more optimal, design. The variant with the best performance was then fabricated and tested

in the helium loop to verify its thermal-hydraulic performance.

5.1   Jet Configurations

Parametric studies were performed on the baseline HEMJ design by systematically

varying the number of jet holes from 1 to 25 and the number of jet rows from 1 to 4 for

different H. This jet array parameterization was also performed for a "flat" design where

the jets issued from a flat surface with only a "fillet" with a prespecified radius of curvature

between the sides of the jet cartridge and this surface. In all cases, the total area of the jet

holes was equal to the total area of the jet holes on the HEMJ divertor of 7.83 mm^2. The

coolant mass flow rate, and hence the average velocity, was also kept constant, with the

mass flow rate equal to the prototypical value of 6.8 g/s in all cases. Figure 5.1 shows the

cross-sectional dimensions of the HEMJ test section and the flat design.
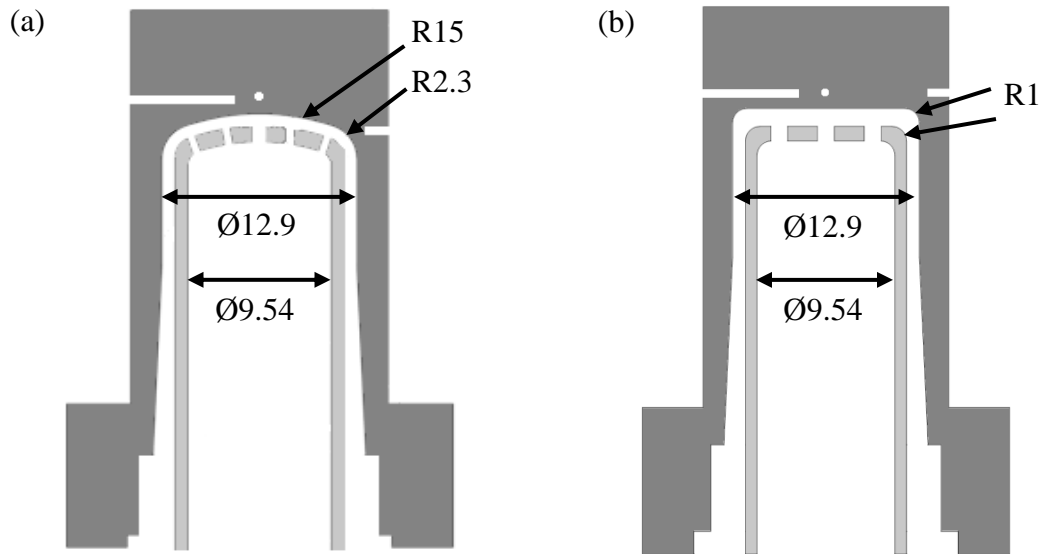
Figure 5.1. Cross-sections of the (a) HEMJ test section and (b) the flat design. The dimensions are given in mm.

To determine how the configuration of, and hence spacing between, the jets affected cooling performance, the jets were arranged on a hexagonal grid over 1 to 4 rows, with the jets evenly spaced over each row, surrounding a central jet. The actual number of jets was 1, 7, 13, 19 or 25. In these configurations, the normalized row spacing S/D and the normalized jets spacing within a row j/D varied by at least one. The simplest case of a single central jet was also considered. Based on these criteria, eight different jet-array configurations, as well as the HEMJ with its jets of two different diameters, were considered, all with a curved surface identical to that of the HEMJ with a major radius of curvature of 15 mm and a "fillet" at the edge with a radius of curvature of 2.3 mm (Figure 5.2, A-I). Four more configurations with a flat impingement surface and only a "fillet" at the edge with a radius of curvature of 1 mm were also considered (Figure 5.2, J-M). Finally, simulations were performed for two additional configurations, both with a flat

surface where one had 25 jets with diameters identical to the HEMJ over 4 rows (Figure 5.2, N) and the other having 37 jets over 3 rows (Figure 5.2, O). Thirteen of the fifteen geometries studied (all except for Figure 5.2, I and N) featured jets with the same D. For the arrays where all the jets have the same diameter, Re was defined to be the Reynolds number based on the jet diameter and average velocity, *i.e.*, that commonly used in jet impingement studies (Eq. 2.27).
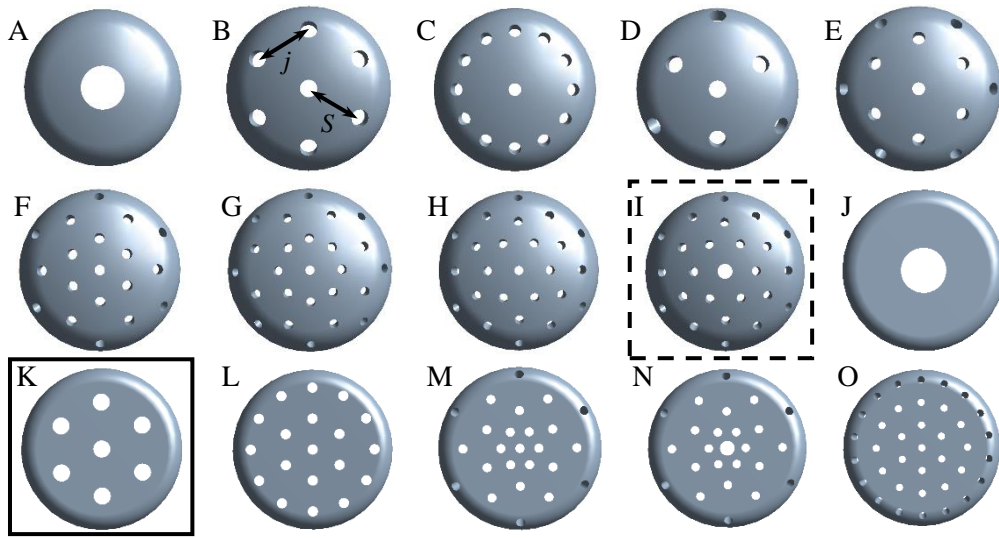
Figure 5.2. CAD models of the 15 jet array geometries, where I is the HEMJ design (dashed box) and K is the "optimized" design (solid box).

Table 5.1 summarizes the number of rows and jets, as well as (D, S, j) for each geometry considered. Note that the values for S were identical to the projected radii of the HEMJ for the curved cases, while the rows were spaced equally over the 12.9 mm diameter of the cooled surface for the flat cases. The area of the curved surface enabled S/D to vary from 2.13 to 10.4 while the flat designs had $1.24 < S/D < 9.45$.

Table 5.1. Summary of parameters for all 15 jet array geometries.

Surface	Jet Design	Number of Rows, Holes	D [mm]	S [mm]	j [mm]
Curved	A	0, 1	3.11	N/A	N/A
	B	1, 7	1.18	4.15	4.02
	C	1, 13	0.865	4.15	2.08
	D	2, 7	1.18	3.52, 6.49	4.37, 6.43
	E	2, 13	0.865	3.52, 6.49	3.43, 5.13
	F	3, 19	0.715	2.22, 4.15, 6.49	2.19, 3.3, 4.4
	G	3, 25	0.624	2.22, 4.15, 6.49	1.68, 2.45, 3.28
	H	4, 25	0.624	2.22, 3.52, 4.77 6.49	2.19, 2.81, 3.81, 4.5
	I	*4, 25*	*0.60, 1.04 center jet*	*2.22, 3.52, 4.77 6.49*	*2.19, 2.81, 3.81, 4.5*
Flat	J	0, 1	3.11	N/A	N/A
	K	**1, 7**	**1.18**	**3.24**	**3.24**
	L	2, 19	0.715	2.16, 4.31	2.16, 2.23
	M	4, 25	0.624	1.29, 2.59, 3.88, 5.17	1.29, 2.59, 3.88, 5.17
	N	4, 25	0.60, 1.04 center jet	1.29, 2.59, 3.88, 5.17	1.29, 2.59, 3.88, 5.17
	O	3, 37	0.513	1.62, 3.23, 4.85	1.62, 1.67, 1.4

Simulations were performed on each of the 15 array geometries for 5 values of the separation distance, namely $H = 0.50$ mm, 0.75 mm, 0.90 mm, 1.25 mm and 1.5 mm, giving a total of 75 different cases. Numerical models for all 75 cases were generated using ANSYS® ICEM® consisting of a structured hexahedral mesh with grid refinement at the solid/fluid interfaces with a mesh dimension of less than one wall unit along the inner pressure boundary of the outer shell. In all cases, the simulations were performed under prototypical conditions: He mass flow rate $\dot{m} = 6.8$ g/s, inlet temperature $T_i = 600$ °C, outlet pressure $p_o = 10$ MPa, and uniform steady-state heat flux $\overline{q''} = 10$ MW/m². Adiabatic boundary conditions were imposed on the outer walls, while symmetry boundary conditions were imposed upon the symmetry planes. The standard k-ε turbulence model

was used in these simulations on numerical models consisting of as many as 7×10^6 hexahedral elements.

5.2   Optimization Results

Several metrics were used to evaluate the thermal performance of the 75 designs. Specifically, the area-averaged HTC $\bar{h}$, the pressure drop across the divertor module Δp, the maximum temperature in the module T_{max}, the maximum and area-averaged temperatures over the cooled surface $T_{cs,max}$ and $\bar{T_c}$, respectively, and the maximum von Mises stress over the cooled surface σ_v^{max} were compared with the results obtained for the HEMJ module. Based on these criteria, the simulation results suggest that several jet designs, including design O with 37 total jets, provide similar or superior thermal performance compared to the HEMJ. However, given that the objective of this optimization study was to find a simpler geometry, only the flat designs with fewer jets and favorable thermal performance were considered for further evaluation. The thermal performance of all 75 cases are summarized in Appendix B.

The best performing flat designs with fewer holes correspond to design K at $H = 0.75$ mm, 0.90 mm, 1.25 mm, and 1.5 mm. Table 5.2 compares the thermal performance of these four cases with the results for the HEMJ at $H = 0.90$ mm. Note that $Re_p = 2.5 \times 10^4$ for the flat design at $\dot{m} = 6.8$ g/s. All four cases have higher $\bar{h}$ than that of the HEMJ, although this is partly due to the smaller cooled surface area of the flat design compared to

the curved surface (A_c = 154 mm^2 for the flat surface *vs.* 184 mm^2 for the curved surface),

since $\bar{h} \propto 1/A_c$.

Table 5.2. Summary of jet designs with favorable thermal performance.

Jet Design	Re_{D_o} [·10^4]	H [mm]	T_{max} [°C]	$T_{cs,max}$ [°C]	$\bar{T_c}$ [°C]	$\bar{h}$ [kW/m^2·K]	Δp [kPa]	σ_v^{max} [MPa]	Max ΔH [mm]
HEMJ	2.2	0.90	1597	992	945	35.7	128	381	0.235
K	2.5	0.75	1585	1059	1005	36.3	125	388	0.223
		0.90	1575	1050	997	37.1	122	391	0.223
		1.25	**1570**	**1049**	**994**	**37.3**	**120**	**379**	**0.222**
		1.50	1578	1052	1003	36.5	122	374	0.217

However, these four cases have higher $\bar{T_c}$ than the HEMJ, although the increase in $\bar{T_c}$ is relatively small. In this work, the maximum temperature of the outer shell was considered the most important measure of thermal performance, and all four cases give lower T_{max} compared with the HEMJ. The simulations also suggest that these four cases also have lower Δp than the HEMJ, and should therefore have lower He pumping power requirements. It should be noted, however, that the cases at H = 0.50 mm and H = 0.75 mm have slightly higher Δp than the cases with $H \geq 0.90$ mm. The H = 1.25 mm case has the lowest T_{max}, a 4.7% higher $\bar{h}$, and a 7% lower Δp compared with the HEMJ.
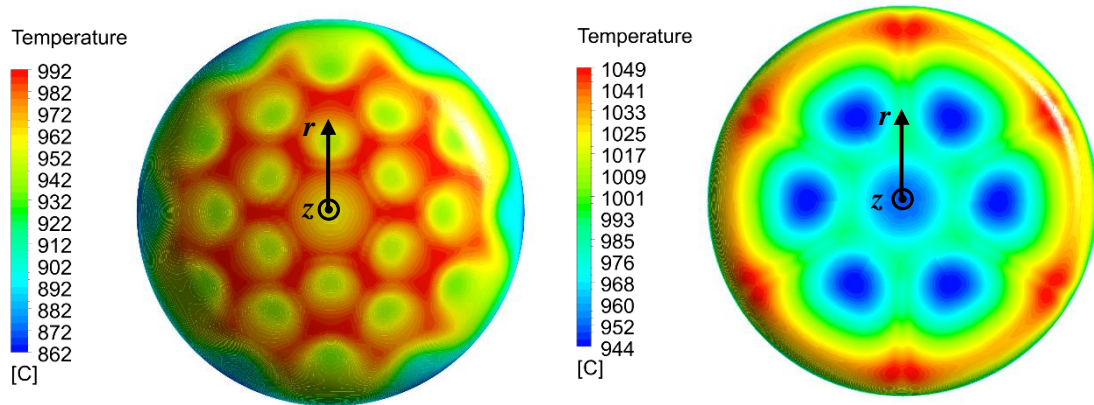
Figure 5.3. Cooled surface temperature distribution for the HEMJ at H = 0.90 mm (left) and jets design K at H = 1.25 mm (right) at prototypical conditions.

Figure 5.3 compares the cooled surface temperature distributions for the HEMJ at H = 0.90 mm and jets geometry K at H = 1.25 mm. The local maximum and minimum cooled surface temperatures for the flat configuration are both higher than the HEMJ because K has fewer impinging jets, resulting in less uniform "coverage" and larger temperature variations over the cooled surface. Nevertheless, T_{max} is 27 °C lower for this case than that of the HEMJ, which suggests that higher cooled surface temperatures do not necessarily lead to higher maximum temperatures overall. Modifying the shape of the impingement surface slightly reduced the volume of the divertor module by 1.6%, from 6544 mm^3 for the HEMJ to 6441 mm^3 for the flat configurations, which resulted in lower maximum thimble temperatures due to the large temperature gradients within the thimble.
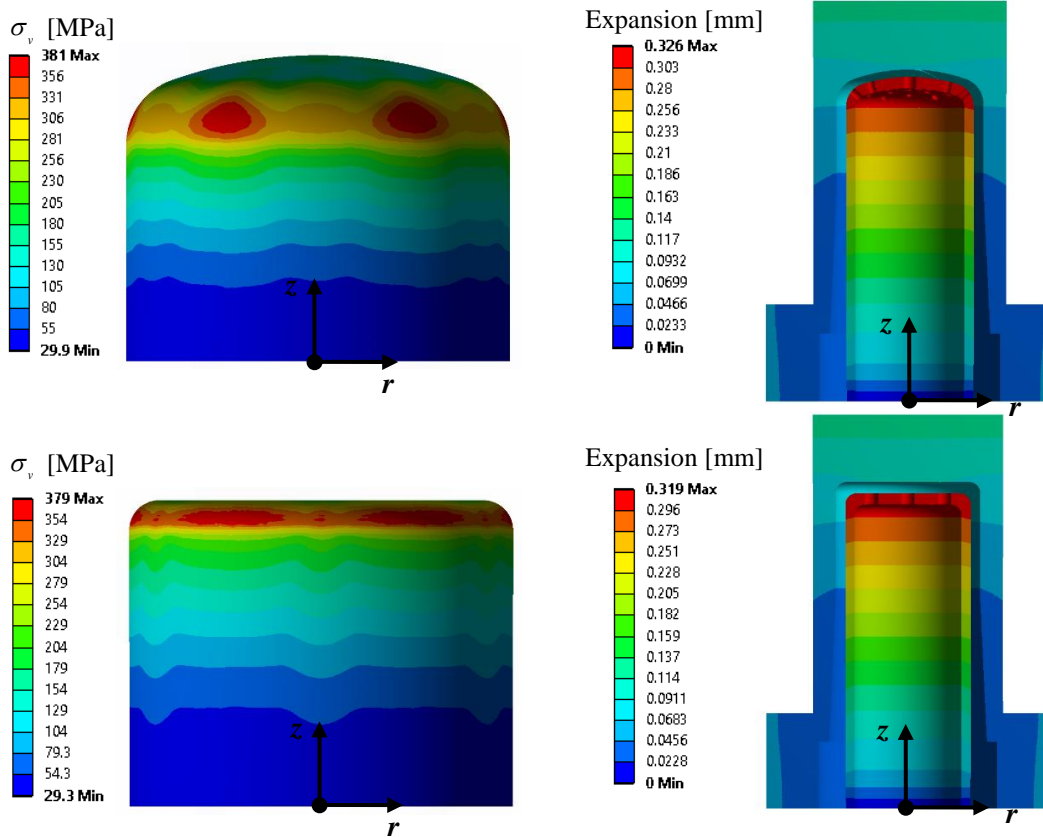
Figure 5.4. Diametric cross-sections of the cooled surface von Mises stresses and thermal expansion of the HEMJ at $H = 0.90$ mm (top row) and design K at $H = 1.25$ mm (bottom row) at prototypical conditions.

Figure 5.4 shows diametric slices of the cooled surface von Mises stress distributions and thermally-induced expansion for the HEMJ and design K. In both cases, the highest local von Mises stresses occur at the impingement locations near the outer row of jets. The flat configuration, however, has lower local and maximum stresses in the outer shell compared with the HEMJ. In all cases, the highest local stresses on the cooled surface occurred near the curved regions, with values ranging from 330 to 464 MPa. The maximum von Mises stress $\sigma_v^{max} = 379$ for design K at $H = 1.25$ mm, which slightly exceeds the corresponding $3S_m$ value of ~373 MPa at $\overline{T}_c$. The reliability of both the HEMJ

and flat designs should therefore be verified to ensure that the divertor target plates have operational lifetimes of ~1 – 2 years.

In all 75 cases, the separation distance H is reduced by ~0.23 mm due to the difference in thermal expansion coefficients of steel and W (Figure 5.4). Differential thermally-induced expansion therefore appears to be independent of variations in jet array geometry, at least for a given total jets area. It seems likely, however, that differential thermal expansion will have a greater effect on the fluid flow for smaller H if the reduction in H becomes comparable to the initial value of H at ambient temperature (*e.g.*, for $H <$ 0.50 mm).

5.3   Experimental Verification of the Optimized Design

In order to verify the thermal performance of the "optimal" HEMJ variant described in the previous section, a test section based on jets design K was fabricated and tested in the helium loop using the same experimental apparatus and procedures used for the HEMJ test section. The external dimensions of the WL10 thimble were identical to the 37.9 mm tall outer shell described in Section 3.1.1. The inner contours of the thimble and the AISI 304 stainless steel jets cartridge were fabricated using EDM and a custom reamer, respectively. Figure 5.5 shows the actual test section components for design K. The four co-planar TC holes were located ~0.5 mm away from the cooled surface and spaced 90° apart at radial distances $r = 0$, 2.1, 4.2, and 6.4 mm from the centerline.

Figure 5.5. Pictures of the WL10 outer shell (left) and steel jets cartridge (right) for the optimized flat design.

The induction heater was used to heat a WL10 workpiece placed at the top of the outer shell; a thin Cu disk between the workpiece and the top of the outer shell was used to improve thermal contact. The separation distance $H = 1.25$ mm based on the simulation results; air-dry clay was used to check the gap distance with two independent sets of measurements before the experiments. The flat design was tested using the Ar-filled chamber at low incident heat fluxes to minimize oxidation of the outer shell and workpiece.

The thermal-hydraulic performance of the flat design was evaluated with the same approach used in the HEMJ experiments. However, the flat design has a smaller $A_c = 154$ mm^2 (*vs.* 184 mm^2 for the HEMJ), so a new area-averaged cooled surface temperature expression was derived for the flat design using a CAD model:

$$\bar{T}_c^F = 0.022T_0 + 0.186T_{2.1} + 0.401T_{4.2} + 0.391T_{6.4} \qquad (5.1)$$

The remaining thermal-hydraulic parameters were calculated using the methods described in Section 3.2.1, where $D_o = 1.18$ mm for the flat design.

Experiments for the flat design were conducted at $1.4 \times 10^4 \le Re \le 6.1 \times 10^4$, 30 °C $\le$ $T_i \le 425$ °C, and 1.1 MW/m² $\le \overline{q''} \le 2.9$ MW/m². Here, $Re_p = 2.5 \times 10^4$ at $\dot{m} = 6.8$ g/s for the flat design. Figure 5.6 compares the $\overline{Nu}$ results from 34 steady-state cases for the flat design with the results from the second set of HEMJ experiments. In both cases, the effect of T_i and $\overline{q''}$ is negligible for all of the inlet temperatures studied here, suggesting that these results can be extrapolated to $T_i = 600$ °C. The $\overline{Nu}$ results for both designs are similar for $T_i < 425$ °C and $Re < 4.0 \times 10^4$, which suggests that the simpler flat design has a thermal performance comparable to the HEMJ divertor over a large range of coolant flow rates, including that at prototypical conditions.
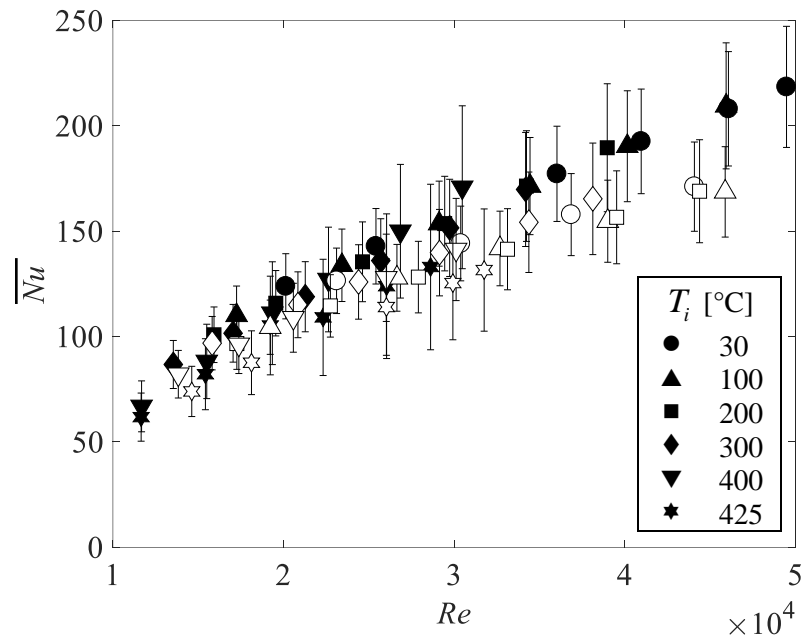
Figure 5.6. Average Nusselt numbers for the HEMJ design at $H = 0.90$ mm (filled symbols) and the flat design at $H = 1.25$ mm (open symbols) as a function of Reynolds number Re.

The loss coefficients K_L for the two designs are shown in Figure 5.7. In both cases K_L is effectively constant over the entire range of Re studied here, with $K_L = 1.68$ and 2.29 for the HEMJ and flat design, respectively. Interestingly, the experiments suggest that the flat design has a K_L significantly higher than that predicted by the simulations, which may be due to imperfections in the machining process or the accuracy of the available turbulence models. Previous simulations of finger-type divertors have shown that small O(1 mm) geometric differences in the jet port geometry can significantly affect the discrepancies in Δp between the numerical predictions and experimental values [32].
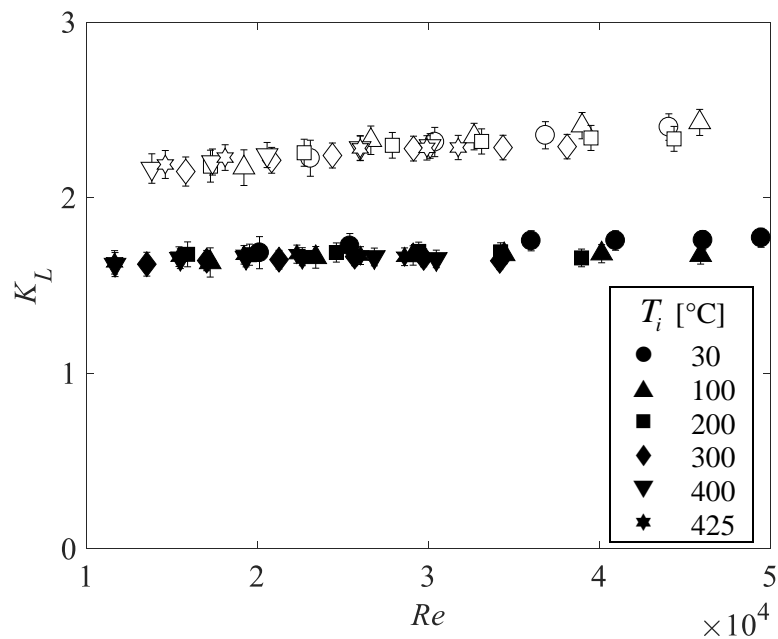
Figure 5.7. Loss coefficients for the HEMJ (filled symbols) and the flat design (open symbols) as a function of Reynolds number Re.

The $\overline{Nu}$ results for the flat design was then compared to the new correlation proposed for the HEMJ divertor (Eq. 3.14). A correlation for the flat design was developed assuming $\overline{Nu} \propto \kappa^{0.19}$ and fitted to the results for all 34 cases, giving the following expression:

$$\overline{Nu} = 0.2163 Re^{0.504} \kappa^{0.19} \qquad (5.2)$$

which is valid for:

$$\begin{bmatrix} 1.4 \times 10^4 \leq Re \leq 6.1 \times 10^4 \\ Pr \approx 0.65 \\ 480 \leq \kappa \leq 974 \end{bmatrix} \qquad (5.3)$$

Figure 5.8 compares the new correlations for the HEMJ (Eq. 3.14) and flat design (Eq. 5.2). The correlation for the flat design predicts a nearly identical $\overline{Nu}$ at $Re = 1 \times 10^4$ compared with Eq. 3.14 but gives a $\overline{Nu}$ that is 18% lower than that for the HEMJ at $Re = 5 \times 10^4$. Although this $\overline{Nu}$ difference between the HEMJ and flat design increases with Re, the flat design $\overline{Nu}$ is only 6% lower than that for the HEMJ at Re_p.
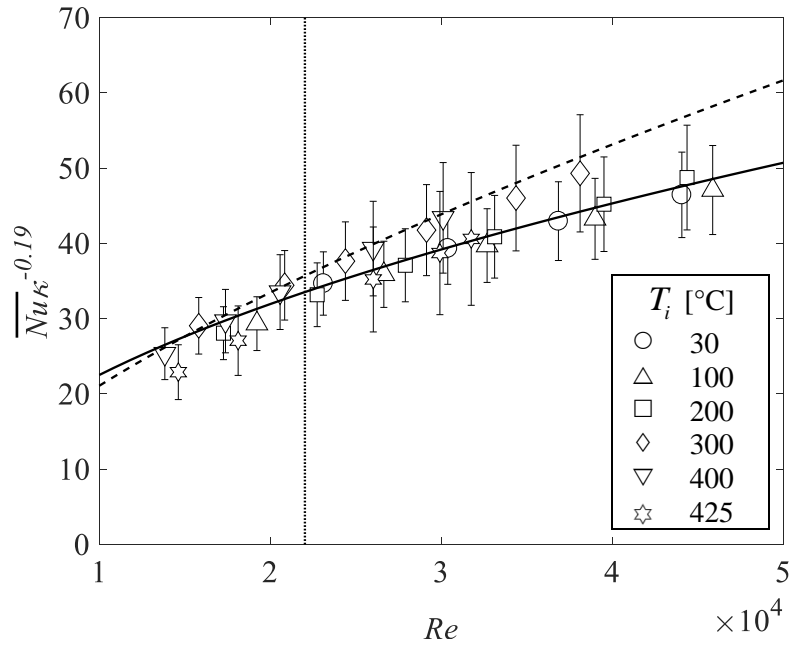
Figure 5.8. Comparison of the $\overline{Nu}$ correlation for the flat design (solid line) (Eq. 5.2) and the HEMJ (dashed line) (Eq. 3.14). The vertical dotted line denotes Re_p for the HEMJ design.

5.4   Prototypical Performance of the Optimized Design

The thermal performance of the flat design at prototypical conditions was estimated using a procedure similar to that described in Section 3.3 for the HEMJ test section. Two He inlet temperatures (T_i = 600 °C and 700 °C) that correspond to the prototypical value and an elevated value based on the estimated increase in the DBTT under neutron irradiation were considered.   Three average pressure boundary temperatures were considered ($\overline{T}_s$ = 1100 °C, 1200 °C, and 1300 °C) to quantify changes in thermal

performance as $\overline{T_s}$ approaches the RCT of 1300 °C, since the actual material temperature limits, especially for W irradiated by fusion-relevant neutrons, are currently unknown.

For a fixed Re, the maximum allowable heat flux $\overline{q''_{max}}$ is calculated from Eq. 3.17 where $\overline{h}$ is obtained from the $\overline{Nu}$ correlation for the flat design (Eq. 5.2). Initial values for the unknown parameters $\overline{T_c}$ and T_o are then updated using an iterative procedure. The process is repeated until $\overline{q''_{max}}$, $\overline{T_c}$, and T_o converge with an error of less than 0.01%. Similarly, $\overline{q''_{max}}$ is calculated for a fixed β from Eq. 3.18 and Eq. 3.19 based on the average loss coefficient for the flat design $K_L = 2.29$.

Figure 5.9 shows $\overline{q''_{max}}$ as over a range of Re that span Re_p for the flat design at inlet temperatures of (a) 600 °C and (b) 700 °C. At Re_p, $T_i = 600$ °C, and $\overline{T_s} = 1200$ °C, a single module of the flat design can accommodate $\overline{q''_{max}} = 10.2$ MW/m² with $\beta = 6.5\%$. Accounting for the larger area of the hexagonal tile gives $\overline{q''_T} = 8.25$ MW/m², which suggests that the flat design could be a viable alternative to the HEMJ in regions where the incident heat flux on the divertor target plates is less than ~8.25 MW/m².
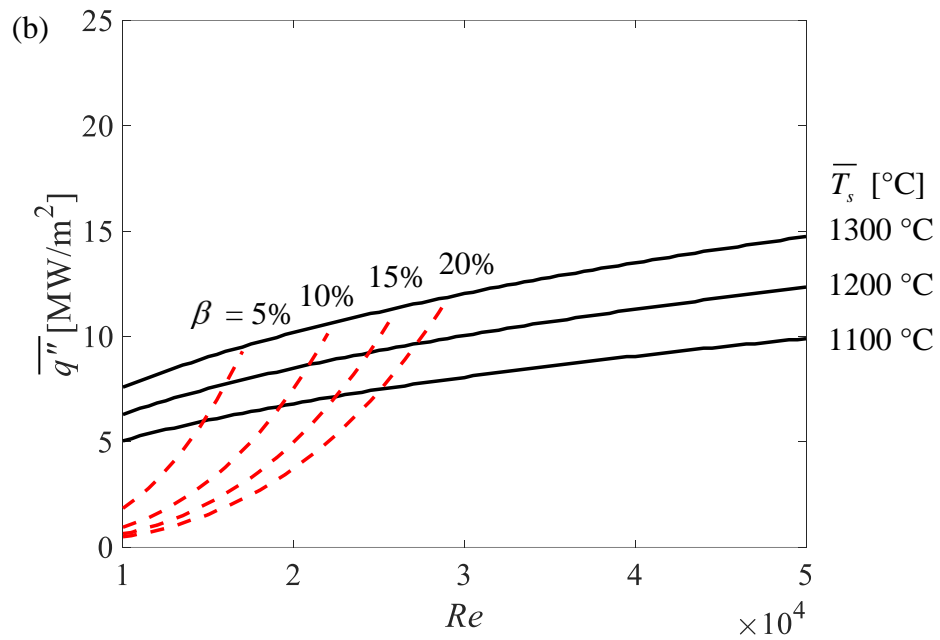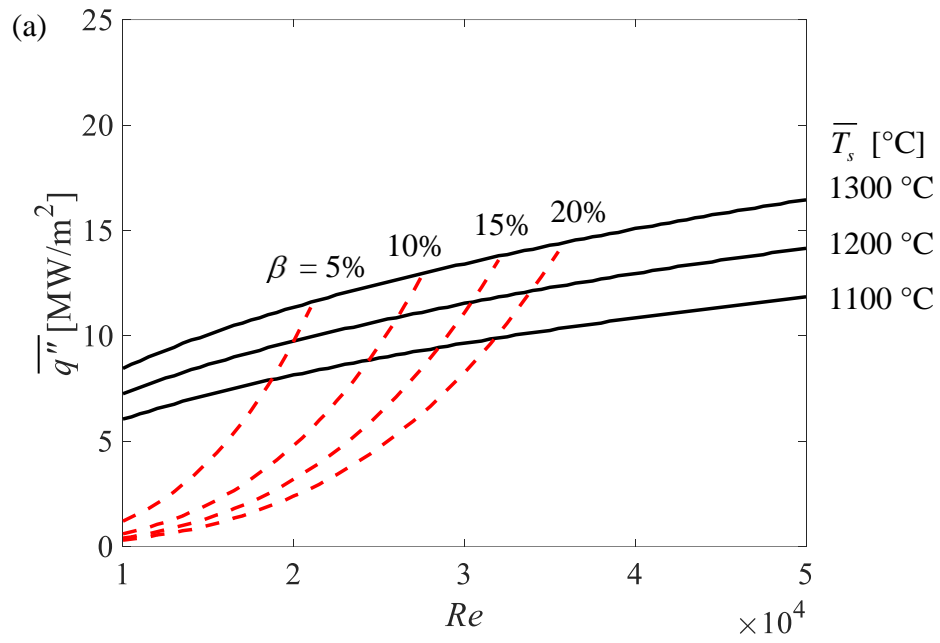
Figure 5.9. Maximum heat flux curves for the flat design as a function of Re at (a) $T_i = 600\,°\text{C}$ and (b) $T_i = 700\,°\text{C}$.

Increasing T_i to 700 °C, however, has a significant impact on the thermal performance for the flat design due to a decrease in the He density and an increase in its viscosity. In this case, $\overline{q''_{max}}$ is reduced to 8.85 MW/m² ($\overline{q''_T}$ = 7.2 MW/m²) with β increases to 11.5% at Re_p and $\overline{T_s}$ = 1200 °C. The thermal performance of the flat design for all six cases are given in Table 5.3.

Table 5.3. Summary of the thermal performance for the flat design at Re_p.

T_i [°C]	$\overline{T_s}$ [°C]	$\overline{q''_{max}}$ [MW/m²]	$\overline{q''_T}$ [MW/m²]	β [%]
	1100	8.45	6.87	7.5
600	1200	10.2	8.25	6.5
	1300	11.8	9.59	5.5
	1100	7.10	5.77	14
700	1200	8.85	7.19	11.5
	1300	10.6	8.62	9.5

CHAPTER 6: CONCLUSIONS AND RECOMMENDATIONS

This chapter summarizes the results presented in the previous chapters, discusses the contributions of this research to the fusion community, and provides recommendations for future work. In this work, the HEMJ divertor was experimentally and numerically studied in order to optimize its thermal-hydraulic performance. Specifically, the objectives of this research were to:

- perform experiments at nearly prototypical conditions, specifically at inlet temperatures as great as 425 °C (*vs.* prototypical values of ~600 °C) and heat fluxes as great as 6.6 MW/m^2 (*vs.* prototypical values of ~10 MW/m^2), for a range of separation distances H varying from 0.5 mm to 1.5 mm;

- conduct coupled CFD and FEM numerical simulations to parametrically evaluate the effect of differential thermal expansion and geometric changes using an experimentally validated model;

- examine the effect of various geometrical parameters (number and arrangement of the jets, jet diameters, and separation distance) to optimize the divertor design; and

- develop generalized design charts that allow designers to estimate the maximum heat flux and pressure drop corresponding to different coolant temperatures and maximum allowable wall temperatures.

6.1   Summary of Research Findings

The thermal performance of a single HEMJ module was experimentally evaluated using a closed He loop constructed in 2013. A new electrical heater was used in the He loop to increase the range of coolant inlet temperatures. A sealed Ar-filled chamber enclosing the induction heater and test section was fabricated and installed in the loop to minimize degradation of the test section and obtain reliable measurements when using an induction heater as a heat source. These experiments were conducted at prototypical coolant inlet pressures of ~10 MPa, inlet temperatures ranging from 30 °C to 425 °C, and incident heat fluxes as great as 6.6 MW/m^2 for coolant mass flow rates up to 10 g/s. A total of 95 experiments were conducted. Correlations were developed for $\overline{Nu}(Re, \kappa)$ and $K_L(Re)$ that were within 10% of the experimental measurements for all but two steady-state cases. The experimental results for area-averaged cooled surface temperatures suggest that $\overline{Nu}$ is effectively independent of T_i and $\overline{q''}$, and can be written in terms of a power-law correlation in terms of Re and κ. The measured pressure drops suggest that K_L is essentially constant and independent of Re. These correlations were used to predict the maximum allowable heat flux at prototypical conditions. The resulting parametric design charts suggest that the HEMJ divertor can accommodate a maximum heat flux of $\overline{q''_{max}} = 13.8$ MW/m^2 on the heated surface ($\overline{q''_T} = 11.2$ MW/m^2 on a hexagonal tile) with a coolant pumping power fraction (compared with the total incident thermal power) $\beta = 5\%$ at $Re_p = 2.2 \times 10^4$, $T_i = 600$ °C, and $\overline{T_s} = 1200$ °C. The HEMJ design can therefore withstand the $\overline{q''} = 10$ MW/m^2 heat fluxes expected for DEMO while keeping $\beta < 10\%$.

The effect of varying H from ~0.5 mm to 1.5 mm was experimentally investigated for H = 0.44 mm, 0.90 mm, and 1.49 mm in the HEMJ divertor. The effect of T_i and $\overline{q''}$ on $\overline{Nu}$ was negligible for all three H. Moreover, $\overline{Nu}$ was effectively independent of H for the range of H studied here. Reducing H to 0.44 mm, however, increased K_L by 33% and 28% compared with the results at H = 0.90 mm and H = 1.49 mm, respectively. Hence, the optimal value of H appears to be in the range 0.90 mm $\leq H \leq$ 1.50 mm.

Three-dimensional numerical CFD simulations of the HEMJ geometry were performed using ANSYS® Fluent® and validated against the experimental measurements. Six turbulence models were evaluated and the standard k-e model gave predictions in best agreement (within 7% on average for $\overline{Nu}$ and K_L) with the experimental results. The area-averaged cooled surface temperature was found to be insensitive to both flow asymmetry and non-uniform incident heat fluxes with Gaussian profiles. At $p_i \approx$ 10 MPa, T_i = 600 °C, $\overline{q''}$ = 10 MW/m² and Re_p, the average HTC for the HEMJ is $\overline{h}$ = 35.7 kW/(m²·K) which corresponds to a maximum tile temperature T_{max} = 1597 °C. Although T_{max} exceeds the RCT of WL10, it satisfies the 2500 °C design limit of the W tile. The maximum and minimum cooled surface temperatures also satisfy the temperature limits imposed by the WL10 DBTT and RCT. A thermo-mechanical model was developed by coupling the initial CFD simulation results to an FEM model. The maximum local von Mises stresses over the cooled surface σ_v^{max} = 381 MPa, which nearly matches the ASME 3S$_m$ value of 387 MPa for the corresponding $\overline{T_c}$. The operational lifetime of a single HEMJ module may therefore be shorter than expected due to damage from thermal stresses. At prototypical conditions, the simulation results suggest H is reduced by ~0.23

mm due to differential thermal expansion, which does not significantly affect thermal performance for $H > 0.50$ mm, but may increase pressure drop for $H \leq 0.50$ mm.

Finally, the coupled CFD/FEM model was used to evaluate the thermal performance of 75 different HEMJ variants, including "flat" designs with cooled surface and jet nozzle geometries more favorable for fabrication. All the variants had the same total jets area, and included jet configurations with 1 to 37 holes equally spaced over 1 to 4 rows. A flat design with one row of six holes surrounding one central hole (all 1.18 mm in diameter) at $H = 1.25$ mm had a 27 °C lower $T_{\max}$, a 4.7% higher $\overline{h}$, and 7% lower Δp compared with the HEMJ at prototypical conditions. This design also had lower $\sigma_v^{\max}$ but higher local cooled surface temperatures. The "optimized" flat design was fabricated and tested in the He loop for $T_i = 30$ °C to 425 °C, and $\overline{q''} = 1.1$ MW/m² to 2.9 MW/m² over a range of Re. The $\overline{Nu}$ results were similar to that of the HEMJ for $Re < 4 \times 10^4$, and K_L was again effectively constant over the entire range of Re; however, the average K_L was 36% higher compared with that of the HEMJ. Nevertheless, the parametric design curves developed for the flat design suggest that a single module can accommodate $\overline{q''_{\max}} = 10.2$ MW/m² on the heated surface ($\overline{q''_T} = 8.25$ MW/m² on a hexagonal tile) with $\beta = 6.5\%$ at Re_p, $T_i = 600$ °C, and $\overline{T}_s = 1200$ °C. These results suggest that the flat design cannot withstand the 10 MW/m² heat fluxes expected at the strike points of the divertor target plates at Re_p and $\overline{T}_s = 1200$ °C. However, the flat variant could potentially be used in locations where the incident heat fluxes are less that ~8 MW/m² to simplify manufacturing and reduce costs associated with the fabrication of these modular target plates.

6.2   Contributions

The thermal-hydraulic performance of the HEMJ divertor was experimentally investigated over a wide range of coolant flow rates, inlet temperatures, and incident heat fluxes in this work. Given the challenges in fabricating such complex geometries and reproducing fusion-relevant operating conditions, there have been few experimental studies of modular finger-type gas-cooled divertor designs. The research findings in this work therefore provide valuable empirical data that will inform the design of future divertor cooling systems. The contributions of the experimental work include:

- characterization of the effects of H on thermal performance

- new correlations for the average Nusselt number and loss coefficients for a wider range of coolant inlet temperature and incident heat fluxes

- evaluation and verification of the thermal performance of a simplified flat HEMJ variant that can withstand slightly lower heat fluxes than the HEMJ at prototypical conditions, but should be easier to manufacture

- new parametric design charts that predict the maximum allowable heat flux that can be accommodated by a single divertor module for different material temperature limits and coolant mass flow rate constraints.

These correlations can be implemented into system codes and used by designers to quickly examine performance trade-offs to improve the overall efficiency of future commercial fusion reactors.

The experimentally validated numerical model was used to provide estimates of thermal expansion effects and their effect on thermal performance, which has not been

previously reported in the literature. These thermo-mechanical simulations provide additional insight into the divertor thermal performance in terms of thermally-induced stresses. These simulations therefore provide a more comprehensive assessment of the performance of finger-type divertors.

6.3 Recommendations for Future Work

The following recommendations would complement and extend the work presented in this dissertation:

- Experimental studies of the divertor modules that extend the range of coolant inlet temperatures and incident heat fluxes to fully prototypical conditions (*i.e.*, p_i = 10 MPa, T_i = 600 °C and $\overline{q''}$ ≥ 10 MW/m^2). Since it is impractical in many cases to achieve such high incident heat fluxes, especially over larger areas, the "reversed heat flux" approach [64] may be a useful alternative for removing large amounts of thermal power from divertor modules based on a coolant energy balance. Such studies will not, however, provide any information on materials behavior at prototypical conditions.

- Other divertor designs, such as the T-Tube or HCFP, should be experimentally studied at fusion-relevant operating conditions. Although such designs have been previously studied using dynamic similarity and numerical simulations [30, 71, 100], there are to date no experimental studies at prototypical, or even near-prototypical, conditions.

- Thermo-mechanical simulations should be performed on the T-Tube and HCFP designs to investigate the effects of thermal deformation on divertor performance. Although Tillack *et al.* [85] performed thermo-mechanical simulations of the both designs for the ARIES study, the effects of deformed geometry on the fluid flow have not been reported for either design.

- Numerical simulations should be used to optimize the HCFP geometry. While the ARIES study used thermo-mechanical simulations to improve the HCFP design [86], there are few numerical and no experimental studies of this improved design, to our knowledge. A parametric numerical study should be performed to examine a wider range of geometric variations such as varying the slot width and slot-to-impingement surface distance. The thermal performance of this optimized design should then be experimentally evaluated.

- The effect of surface roughness on the cooled surface should be investigated. Greater surface roughness would generally improve heat transfer rates at the expense of increased pressure drop. Detailed measurements of the surface roughness in the existing test sections should be taken to determine if surface roughness has a significant effect on thermal performance.

- The effects of neutron irradiation should be considered when evaluating the thermal performance of W-based divertor modules. The few studies of neutron irradiation effects on W suggest that its thermal conductivity will decrease while its DBTT will increase [92, 101]. The impact of these material property changes on thermal performance could be investigated numerically.

APPENDIX A: DETAILED EXPERIMENTAL PROCEDURE

A.1.   Separation Distance

The nozzle exit-to-impingement surface separation distance H is an important geometric parameter for jet impingement cooling designs such as the HEMJ. Given that the values of H considered here are quite small (*i.e.*, $O(1$ mm)), it is important that the procedure for setting the separation distance give an accurate and repeatable value of H. Numerous measurements of H at room temperature were therefore performed using air-dry clay based on the procedure described below:

1. Prepare the test section by compressing clay on the inner surface of the jets cartridge to prevent clay in the impingement region from falling through the cartridge and into the manifold tubing. Thread the cartridge onto compression spring and cartridge holder in the manifold to an arbitrary depth.

2. Set the separation distance. First, finger-tighten an aluminum bracket to the manifold. Next, use the depth micrometer to set the jets cartridge depth relative to the inner surface of the top of the bracket, as shown in Figure A.1. The stagnation point is defined as the nozzle location that produces the lowest reading on the micrometer.

3. Remove the micrometer and bracket, and place a gasket in the sealing surface.

4. Place a dime-sized amount of clay on the tip of the jets cartridge nozzle.
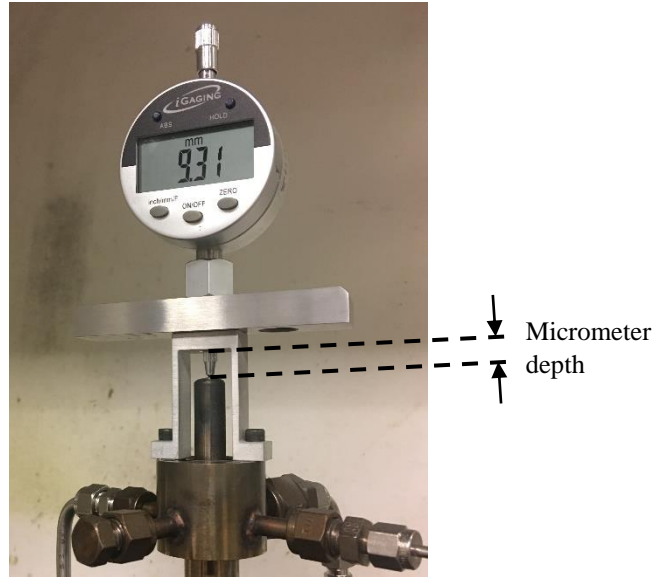
Figure A.1. Picture of the separation distance adjustment process for $H = 0.90$ mm.

5. Cover the cooled surface of the outer shell with a lubricant (*e.g.*, vegetable oil) to enable smoother clay separation after it has been compressed.

6. Assemble the outer shell to the manifold and compress the clay inside the impingement region. Bolt the compression collar onto the outer shell using a star pattern. Use a thin gage block to ensure that the gap between the collar and manifold is azimuthally even. The collar should be tightened until this gap is less than the smallest gage block size (0.305 mm).

7. Allow the clay to dry for at least 24 h. Slowly remove the outer shell and separate the clay from the test section, ensuring that the clay does not bend or tear. If necessary, direct a low flow rate of compressed air at the inner and outer surfaces of the clay, allowing it to dry further until both surfaces are stiff.

8. Measure the thickness of the clay around the central jet using a digital height gage with a fine tip and a smooth, flat surface. Calculate a mean value and standard deviation based on ten measurements with the gage. The separation

distance is assumed to be equal to the average clay thickness around the central

jet hole.

9. Remove the remaining clay from the inner surface of the jets cartridge, and

   clean both the cartridge and outer shell using a solvent.

This procedure was used to obtain independent measurements for nominal separations $H = 0.50$ mm, 0.90 mm, and 1.50 mm. Each measurement was repeated three times for each H to verify the required micrometer depth settings. The corresponding average depths for these separation distances and their standard deviations (SD) are summarized in Table A.1.

Table A.1. Summary of micrometer depths for three H values.

Micrometer Depth [mm]	Mean $H \pm$ SD [mm]
8.86	0.50 ± 0.03
9.31	0.90 ± 0.03
9.99	1.50 ± 0.02

A.2. Helium Loop Operation

Before performing an experiment, the HEMJ test section was first fitted with thermocouples, sealed, and insulated. The Ar enclosure and W-alloy workpiece were then installed above the test section. For the sake of efficiency, the experiments on the HEMJ test section were performed in sets that consisted of several individual steady-state cases. Specifically, the coolant inlet temperature and incident thermal power were increased to the desired value at a given mass flow rate until steady-state conditions were reached. After

acquiring the data for that specific case, the mass flow rate and electric heater power was then changed (without adjusting the induction heater), and data were acquired at each flow rate. The following procedure is an example of a typical experiment performed at high He inlet temperatures:

1. Fully open all of the valves in the loop except the buffer tank ball valves, and the bypass ball valve. For experiments at room temperature, open the bypass ball and needle valve, and close the recuperator needle valve.

2. Evacuate this portion of the loop with the vacuum pump. Slowly open the downstream buffer tank valve until atmospheric pressure is reached. Repeat this step two more times.

3. Slowly open the downstream buffer tank valve (to avoid fluid hammer) until the valve is fully open. Open the upstream buffer tank valve in the same manner.

4. Turn on the cooling water supply for the induction heater, water-cooled heat exchanger, and compressor.

5. Open the oxygen tank that controls the pneumatic valves on the compressor.

6. Turn on the compressor in manual mode, and press the right arrow twice. Select the "Start Cooling" option followed by "Open Valves".

7. Slowly open the inlet and discharge ball valves on the compressor lines.

8. Open the He source tank. Slowly open the source tank needle valve to charge the loop to a pressure slightly less than 10 MPa (*e.g.*, 1420 psig), then close the valve and the tank. The He in the loop will reach 10 MPa after being heated.

9. On the compressor, select the "Close Valves" option, followed by "Stop Cooling". Switch the compressor to automatic mode. Start the data acquisition system. Press "Start".

10. Begin closing the main bypass valve and recuperator valve. Closing the main bypass valve will increase both the mass flow rate and pressure drop across the compressor. Closing the recuperator valve will decrease the mass flow rate and increase the compressor pressure drop. Adjust the valves until the desired mass flow rate is reached and the compressor pressure drop is ~1.03 – 1.24 MPa (~150 – 180 psig).

11. Begin the heating process. Open the argon tank and flow Ar at ~55 kPa (8 psig). Turn on the induction heater and apply a low amount of power. Turn on the electric heater and begin heating the coolant. Gradually increase the power to both heaters until the desired coolant inlet temperature and incident heat flux are achieved, which may take 1 – 2 h.

12. Allow the experiment to reach steady-state. This may take up to 1.5 h for a single case. Save the data and begin sampling again.

13. Change the mass flow rate by adjusting the main bypass valve and recuperator valve while remaining within the same compressor pressure drop range. Also adjust the electric heater to achieve the proper coolant inlet temperature at the new mass flow rate.

14. Repeat steps 11 and 12 until steady-state data are acquired at every desired mass flow rate. A set of high T_i experiments may take ~4 – 5 h.

15. Begin the cool down process. Gradually decrease power to the electric heater and induction heater. Open slightly the main bypass valve to lower the compressor pressure drop. Open the recuperator valve until the mass flow rate is ~8 g/s to allow for faster cooling. Once the thimble temperatures fall below ~250 °C, open the bypass ball and needle valves while closing the recuperator valve. This process may take ~1 – 2 h.

16. When the coolant inlet and outlet temperatures have reached room temperature, turn off the induction and electric heaters.

17. Stop the compressor and immediately close the buffer tank valves.

APPENDIX B: EXPERIMENTAL AND NUMERICAL DATA

This appendix presents all the experimental and numerical data for the HEMJ and flat designs. Section B.1 gives the time-averaged experimental measurements for all of the cases presented in this work, where each row corresponds to a single steady-state case. Section B.2 provides the simulation results for comparison with the experiments, the thermo-mechanical simulation results at fully prototypical conditions, and the jet array optimization results.

B.1.   Experimental Data

Table B.1. HEMJ Experimental Results at $H = 0.44$ mm

$\dot{m}$	Re	$\overline{q''}$	T_i	T_o	$T_{c,8}$	$T_{c,6}$	$T_{c,4}$	$T_{c,2}$	$\overline{T_c}$	p_o	Δp	$\overline{h}$	$\overline{Nu}$	κ	K_L
[g/s]	[–]	[W/m²]				[°C]					[Pa]	[W/m²·K]		[–]	
3.18	21181	4018696	31.0	86.3	364	355	353	308	331	10027769	16265	16473	98.88	503	3.009
4.04	26908	3990026	31.0	74.2	322	312	311	269	291	10015116	26379	18921	114.96	507	3.021
4.70	31345	3976591	30.9	67.8	297	287	287	246	267	9987853	35781	20712	126.66	508	3.014
6.25	41658	3926819	30.7	58.2	255	246	247	210	229	9931199	63163	24432	150.92	509	3.000
7.01	46856	3945609	29.3	54.0	242	234	235	198	216	9895119	79189	25965	161.30	511	2.992
3.12	18172	3664723	99.0	150	397	388	386	347	367	10024710	19213	16823	89.59	448	3.017
4.02	23348	3666406	100	140	361	353	352	313	333	9966933	32223	19380	103.99	450	3.024
5.22	30346	3683188	100	131	327	319	320	283	301	9933834	54701	22522	121.83	452	3.032
5.94	34535	3720024	100	127	315	307	308	271	290	9951932	70536	24164	131.10	452	3.024
6.77	39273	3748996	102	126	304	296	297	261	279	9908095	91942	25961	140.86	452	3.006
3.00	14839	3274036	200	248	460	453	452	417	435	9959796	23577	17175	78.79	388	3.130
3.99	19760	3276787	200	236	422	415	415	382	399	9900624	42260	20279	93.83	391	3.151
4.87	24114	3290858	200	230	401	394	395	362	379	9927378	63510	22664	105.30	392	3.186
5.90	29163	3311237	201	225	384	378	378	347	363	9899926	94297	25139	117.07	392	3.213
6.91	34247	3331392	199	220	369	363	364	333	349	9810217	129639	27466	128.49	393	3.198
7.95	39377	3377073	200	219	364	357	358	327	343	9841757	172781	29189	136.62	393	3.220
2.83	12328	2879495	299	343	535	528	528	496	512	10224085	25714	16579	67.45	346	3.243
3.98	17269	2847264	300	331	494	487	488	459	473	10164617	50954	20207	82.69	347	3.237
4.93	21423	2809624	299	324	469	462	464	436	450	10109215	78925	22883	94.10	348	3.255
5.89	25583	2752465	300	320	450	444	445	420	433	10053972	114309	25443	104.83	349	3.279
6.71	29073	2717784	302	320	440	434	435	412	423	9997739	149630	27525	113.28	348	3.273

Table B.2. HEMJ Experimental Results at H = 0.90 mm

$\dot{m}$	Re	$\overline{q''}$	T_i	T_o	$T_{c,8}$	$T_{c,6}$	$T_{c,4}$	$T_{c,2}$	$\overline{T_c}$	p_o	Δp	$\overline{h}$	$\overline{Nu}$	κ	K_L
[g/s]	[−]	[W/m^2]				[°C]					[Pa]		[W/m^2·K]		[−]	
2.94	19587	5473207	31.3	113	410	418	427	398	410	10222097	10685	17770	103.95	813	2.351
3.43	22911	5165241	30.6	96.3	352	361	369	353	359	10009008	14581	19360	115.12	847	2.309
3.95	26403	5893333	30.0	95.2	378	385	388	361	373	10091133	19290	21143	125.92	842	2.328
4.94	32965	6053098	30.6	84.2	343	348	354	330	340	10075212	30161	24068	144.82	865	2.321
5.33	35543	5648783	30.9	77.2	305	313	323	308	314	10193050	35174	24579	148.89	882	2.350
5.92	39387	6577790	31.4	80.0	337	339	351	320	333	9974242	43417	26858	162.17	871	2.304
5.96	39843	6080893	29.7	74.3	314	317	324	302	311	10059445	43821	26565	161.59	886	2.322
6.89	45945	6194638	31.0	70.2	292	295	304	285	292	10031162	58685	29169	177.92	897	2.309
7.93	52801	6265711	31.2	65.8	275	276	287	269	276	9999298	77106	31534	193.16	909	2.285
2.93	17029	5372291	101	181	462	473	481	450	463	10255155	12895	18250	94.61	703	2.327
4.01	23348	5683640	100	162	423	430	434	410	421	10033645	24137	21802	114.96	729	2.287
4.99	28978	5693395	101	151	386	393	399	377	387	10012239	37640	24534	130.40	747	2.293
5.95	34588	5670379	101	142	357	365	371	352	360	9970857	53732	26915	144.13	762	2.293
6.50	37764	5656311	100	139	337	343	357	338	345	10010493	64015	28532	153.27	770	2.302
6.96	40459	5891497	100	138	342	347	355	337	344	9928214	73360	29790	160.17	771	2.280
3.98	19655	5024795	202	257	480	490	494	469	480	10109984	29735	22223	101.19	612	2.263
4.95	24417	5423933	202	250	468	478	483	460	470	10084055	46348	24925	114.04	618	2.279
5.94	29375	5449598	201	241	442	453	459	438	447	10016812	67182	27313	125.81	629	2.280
6.98	34558	5538225	200	235	422	433	438	419	427	9995810	92245	30012	138.95	638	2.268
8.29	41076	5091126	199	226	375	381	399	383	388	9898902	130764	33254	154.91	654	2.261
4.92	21368	4566808	300	340	517	530	542	515	526	10060073	55233	24898	101.36	537	2.269
6.14	26556	4582800	303	336	495	508	521	496	506	9948381	87063	27837	113.45	542	2.262
6.98	30255	4656554	301	330	483	496	510	487	495	9901105	112627	29541	120.86	547	2.259

Table B.3. HEMJ Experimental Results at H = 1.49 mm

$\dot{m}$	Re	$\overline{q''}$	T_i	T_o	$T_{c,8}$	$T_{c,6}$	$T_{c,4}$	$T_{c,2}$	$\overline{T_c}$	p_o	Δp	$\overline{h}$	$\overline{Nu}$	κ	K_L
[g/s]	[−]	[W/m^2]				[°C]					[Pa]		[W/m^2·K]		[−]	
3.55	23845	4807513	27.4	86.6	336	322	328	336	331	9984175	15794	19461	117.21	869	2.361
3.98	26752	4831912	27.5	80.5	318	304	309	321	315	9969496	20003	20685	125.32	881	2.369
4.41	29647	4817778	27.1	74.9	300	287	292	306	299	9961991	24592	21822	133.00	894	2.377
5.17	34711	4812174	27.4	68.1	277	264	269	287	278	9957724	33807	23644	145.06	909	2.378
5.95	39952	4814671	27.4	62.8	259	246	251	271	261	9941254	44769	25390	156.60	922	2.372
6.89	46290	4838758	27.5	58.2	242	229	235	256	245	9915793	59904	27363	169.57	933	2.357
8.03	53945	4860710	27.5	53.9	224	212	218	241	229	9878258	80507	29624	184.39	945	2.324
4.91	28486	5091537	102	147	373	353	368	354	359	10005247	37778	24397	129.98	759	2.367
5.92	34420	5097553	101	138	347	327	342	330	334	9978797	54799	26908	144.58	774	2.363
6.95	40442	5178564	99.4	132	330	310	326	314	318	9922808	74908	29182	157.79	785	2.345
7.98	46387	5164522	100	129	316	296	312	300	303	9916264	98070	31305	169.63	793	2.318
3.43	16982	3294381	200	242	424	405	395	431	416	10047807	22107	18756	86.45	639	2.267
4.05	19999	3492291	201	239	421	400	393	422	409	10044320	31437	20662	95.30	641	2.306
5.01	24794	3691362	200	233	410	392	381	405	396	10037085	48822	23279	107.90	648	2.337
5.89	29144	3805347	200	229	400	385	371	393	385	10015149	68084	25394	118.01	653	2.353
6.83	33854	3910144	200	225	389	377	361	381	375	9978435	91903	27532	128.37	659	2.354
8.05	39802	3953852	201	223	378	371	350	369	364	9930589	127339	30011	139.95	662	2.330

Table B.4. HEMJ Experimental Results at H = 0.90 mm with the Sealed Chamber

$\dot{m}$	Re	$\overline{q''}$	T_i	T_o	$T_{c,8}$	$T_{c,6}$	$T_{c,4}$	$T_{c,2}$	$\overline{T_c}$	p_o	Δp	$\overline{h}$	$\overline{Nu}$	κ	K_L
[g/s]	[–]	[W/m^2]				[°C]					[Pa]		[W/m^2·K]		[–]	
3.02	20128	1450477	31.5	52.4	126	136	124	115	121	9864062	8399	19957	123.90	997	1.687
3.82	25411	1393502	31.8	47.7	111	121	109	101	107	9850328	13747	22912	142.89	1009	1.726
5.41	36015	1326148	31.7	42.4	92.9	104	91.5	84.2	89.4	9754864	28327	28265	177.28	1024	1.754
6.16	40950	1306487	32.3	41.5	87.7	98.5	86.4	79.7	84.6	9716967	36955	30712	192.68	1027	1.756
6.94	46060	1293455	32.6	40.7	83.4	94.0	82.2	75.9	80.6	9693123	47029	33159	208.15	1030	1.758
7.45	49463	1288710	32.7	40.2	80.8	91.4	79.7	73.7	78.2	9732932	54468	34802	218.55	1032	1.771
2.97	17246	1442429	101	122	194	199	193	183	189	9781905	9689	20209	110.09	845	1.631
4.02	23416	1402201	99.1	114	175	180	174	165	170	9736415	18090	24379	133.86	860	1.660
5.01	29113	1378131	100	112	165	170	164	156	161	9678169	28516	27958	153.63	864	1.671
5.92	34436	1361903	100	110	157	163	157	149	154	9616066	40165	31120	171.47	870	1.677
6.90	40136	1355646	100	109	152	157	151	144	148	9558557	55068	34515	190.37	873	1.681
7.91	45925	1357442	101	108	148	153	147	141	145	9537682	72301	38015	209.54	874	1.673
3.22	15923	1459986	200	220	291	296	290	276	284	9756713	14860	21582	100.89	691	1.677
3.94	19541	1449499	199	215	279	284	277	265	272	9664213	22440	24680	115.86	698	1.675
4.97	24623	1439949	200	213	268	273	267	255	261	9590104	36279	28822	135.52	702	1.688
5.94	29438	1439205	200	210	260	265	259	247	254	9564937	52094	32618	153.66	706	1.694
6.92	34228	1444492	200	210	255	261	254	243	249	9519401	70947	36404	171.47	708	1.691
7.86	38961	1459113	200	208	250	255	249	238	244	9489628	90049	40203	189.66	711	1.657
3.12	13539	2081167	300	329	432	437	430	411	421	9525691	16725	21180	86.78	566	1.621
3.92	17041	2091170	299	323	413	420	412	393	404	9503019	26817	24691	101.59	573	1.642
4.90	21269	2111559	300	318	399	405	398	380	390	9489245	42023	28842	118.94	578	1.647
5.91	25693	2123397	299	314	387	393	386	369	378	9548644	61332	32904	136.10	583	1.664
6.84	29729	2145028	299	313	380	386	379	362	371	9470131	82608	36636	151.62	586	1.657
7.87	34178	2182815	300	312	373	380	373	357	365	9406468	109057	41032	169.86	588	1.640

Table B.4 (continued). HEMJ Experimental Results at $H = 0.90$ mm with the Sealed Chamber

$\dot{m}$	Re	$\overline{q''}$	T_i	T_o	$T_{c,8}$	$T_{c,6}$	$T_{c,4}$	$T_{c,2}$	$\overline{T_c}$	p_o	Δp	$\overline{h}$	$\overline{Nu}$	κ	K_L
[g/s]	[–]	[W/m^2]				[°C]					[Pa]	[W/m^2·K]		[–]	
3.00	11680	735094	399	410	455	455	465	438	449	9890993	17509	17987	66.91	507	1.619
3.99	15498	818025	400	409	447	448	458	431	442	9856709	31691	23724	88.24	509	1.653
4.98	19341	888905	400	408	442	442	452	426	437	9792324	49876	29865	111.13	511	1.658
5.82	22630	1266769	399	408	450	450	462	432	445	9786752	68254	34151	127.12	509	1.664
6.91	26844	1337514	399	408	446	445	457	428	440	9736255	96608	40304	150.03	510	1.662
7.84	30467	1385375	399	407	442	442	452	425	437	9663454	124553	45897	170.91	511	1.651
3.08	11654	757181	424	435	487	486	486	472	479	9802410	19358	17032	61.79	488	1.632
4.07	15420	843791	425	434	478	478	478	465	471	9783847	34718	22642	82.15	490	1.664
5.08	19222	938572	425	433	472	472	472	459	465	9754186	54530	29013	105.28	491	1.674
5.89	22315	904177	425	432	469	468	469	456	462	9730167	73766	30047	109.13	493	1.678
6.87	26034	937860	424	430	465	464	465	453	458	9676896	100267	34092	123.94	494	1.670
7.55	28611	952320	424	430	462	462	463	450	456	9633602	120976	36574	133.05	495	1.664

$\dot{m}$	Re	$\overline{q''}$	T_i	T_o	$T_{c,8}$	$T_{c,6}$	$T_{c,4}$	$T_{c,2}$	$\overline{T_c}$	p_o	Δp	$\overline{h}$	$\overline{Nu}$	κ	K_L
[g/s]	[–]	[W/m^2]				[°C]					[Pa]		[W/m^2·K]		[–]	
3.06	23103	2884257	31.7	73.0	196	222	261	288	263	9385286	11933	18341	126.49	907	2.225
4.02	30377	2846347	31.8	62.8	164	191	229	264	234	9401575	21465	20699	144.21	930	2.317
4.88	36849	2827345	31.6	56.9	145	171	208	250	216	9393440	32082	22527	157.92	945	2.356
5.83	44067	2797335	31.3	52.2	127	154	191	237	201	9384359	46717	24293	171.19	957	2.402
6.90	52169	2790888	31.3	49.0	113	139	176	227	188	9345970	66177	26241	185.52	967	2.417
8.10	61184	2795597	31.5	46.6	101	128	164	218	177	9302455	91679	28223	200.02	974	2.420
2.91	19217	2114383	100	132	221	242	277	311	283	9734679	12473	17043	104.46	798	2.171
4.04	26639	2551420	100	128	213	238	272	314	281	9607804	26005	20792	127.92	802	2.327
4.95	32677	2596579	100	123	198	223	257	300	266	9478973	39940	22952	141.85	812	2.348
5.91	38991	2647913	100	119	186	211	246	291	256	9530098	58020	24967	154.78	819	2.410
6.95	45870	2708582	100	117	175	201	236	282	246	9463931	81365	27144	168.71	825	2.429
8.03	53025	2753221	100	115	166	193	228	275	238	9395475	108790	29182	181.67	829	2.411
3.07	17261	1696789	200	224	289	305	337	354	336	9779067	17528	18273	96.72	672	2.180
4.04	22740	1769369	199	218	273	289	320	336	320	9672876	31688	21547	114.59	680	2.256
4.96	27895	1808211	200	216	263	279	311	327	310	9607050	49136	24092	128.26	684	2.298
5.90	33117	1844613	200	214	256	272	303	319	303	9556708	70513	26559	141.48	687	2.320
7.03	39511	1882796	200	211	247	263	294	311	294	9467312	101791	29333	156.64	692	2.340
7.89	44370	1920377	200	210	242	259	289	306	289	9412006	128868	31630	169.01	694	2.335

Table B.5 (continued). Flat Design Experimental Results at $H = 1.25$ mm with the Sealed Chamber

$\dot{m}$	Re	$\overline{q''}$	T_i	T_o	$T_{c,8}$	$T_{c,6}$	$T_{c,4}$	$T_{c,2}$	$\overline{T_c}$	p_o	Δp	$\overline{h}$	$\overline{Nu}$	κ	K_L
[g/s]	[−]	[W/m²]				[°C]					[Pa]	[W/m²·K]		[−]	
4.95	24392	1898026	300	316	365	383	413	406	403	9347301	59310	26891	125.95	575	2.240
5.92	29134	1922868	300	314	356	373	403	399	395	9331310	86379	29830	139.87	578	2.280
6.98	34369	1941374	300	312	347	364	393	394	387	9349836	120212	32860	154.29	581	2.286
7.73	38116	1972598	300	311	342	359	387	390	382	9354603	147951	35196	165.40	583	2.291
3.14	13832	1679365	399	422	491	509	541	519	525	9734566	25942	19596	82.17	487	2.166
3.94	17378	1748458	400	419	477	495	526	507	512	9666171	42019	22940	96.33	491	2.203
4.67	20572	1796762	400	416	468	485	516	497	502	9613328	60272	25915	108.96	494	2.243
5.90	26016	1865592	399	413	455	473	503	486	490	9521877	98989	30372	127.92	497	2.283
6.82	30107	1902420	398	411	448	466	495	478	482	9413509	134237	33499	141.36	500	2.295
3.40	14620	1088054	424	438	489	502	522	511	513	9654654	32266	18007	73.99	480	2.189
4.21	18118	1157924	424	436	479	492	511	504	504	9670131	50252	21290	87.62	483	2.228
6.06	26023	1283196	425	434	466	479	497	497	493	9620618	107041	27704	114.04	485	2.281
6.97	29917	1342263	426	434	462	476	494	496	491	9610950	142318	30487	125.42	485	2.284
7.38	31749	1363611	424	432	458	471	489	493	487	9600384	159538	31924	131.60	487	2.286

B.2.   Numerical Data

Table B.6. HEMJ Simulation Results at $H = 0.90$ mm Based on Experiments with the Sealed Chamber

$\dot{m}$	Re	$\overline{q''}$	T_i	$\overline{T_c}$	p_o	$\overline{h}$	$\overline{Nu}$	K_L
[g/s]	[−]	[W/m^2]	[°C]		[Pa]	[W/m^2·K]	[−]	
3.02	20128	1450477	31.5	126	9971911	18830	116.90	1.777
3.82	25411	1393502	31.8	110	9963564	21858	136.32	1.787
5.41	36015	1326148	31.7	91.3	9883131	27398	171.84	1.813
6.16	40950	1306487	32.3	86.1	9854308	29861	187.34	1.822
6.94	46060	1293455	32.6	81.8	9841003	32310	202.82	1.827
7.45	49463	1288710	32.7	79.4	9888194	33922	213.03	1.830
2.97	17246	1442429	101	193	9891417	19147	104.31	1.770
4.02	23416	1402201	99	174	9854821	23184	127.30	1.781
5.01	29113	1378131	100	164	9807784	26700	146.72	1.794
5.92	34436	1361903	100	156	9758362	29752	163.93	1.807
6.90	40136	1355646	100	151	9717131	32948	181.72	1.818
7.91	45925	1357442	101	147	9715541	36103	199.00	1.824
3.22	15923	1459986	200	287	9871342	20797	97.22	1.764
3.94	19541	1449499	199	275	9786927	23626	110.91	1.770
4.97	24623	1439949	200	265	9727385	27383	128.75	1.781
5.94	29438	1439205	200	257	9719039	30703	144.64	1.792
6.92	34228	1444492	200	253	9694062	33907	159.71	1.804
7.86	38961	1459113	200	248	9687240	36925	174.20	1.814

Table B.6 (continued). HEMJ Simulation Results at $H = 0.90$ mm Based on Experiments with the Sealed Chamber

$\dot{m}$	Re	$\overline{q''}$	T_i	$\overline{T_c}$	p_o	$\overline{h}$	$\overline{Nu}$	K_L
[g/s]	[−]	[W/m^2]	[°C]		[Pa]	[W/m^2·K]	[−]	
3.12	13539	2081167	300	423	9642865	20864	85.49	1.761
3.92	17041	2091170	299	406	9630867	24090	99.12	1.766
4.90	21269	2111559	300	393	9633520	27733	114.37	1.774
5.91	25693	2123397	299	382	9713342	31273	129.35	1.783
6.84	29729	2145028	299	376	9658418	34387	142.32	1.791
7.87	34178	2182815	300	371	9625327	37702	156.07	1.803
3.00	11680	735094	399	442	10008959	20959	77.96	1.754
3.99	15498	818025	400	440	9989430	25011	93.02	1.758
4.98	19341	888905	400	438	9944436	28743	106.95	1.766
5.82	22630	1266769	399	448	9958511	31698	117.99	1.774
6.91	26844	1337514	399	446	9938810	35381	131.71	1.782
7.84	30467	1385375	399	444	9897502	38412	143.03	1.790
3.08	11654	757181	424	468	9922213	21367	77.52	1.753
4.07	15420	843791	425	466	9919530	25449	92.34	1.758
5.08	19222	938572	425	465	9910686	29233	106.08	1.766
5.89	22315	904177	425	460	9907034	32135	116.71	1.772
6.87	26034	937860	424	457	9882731	35451	128.88	1.780
7.55	28611	952320	424	455	9862395	37666	137.02	1.785

Table B.7. Flat Design Simulation Results at H = 1.25 mm Based on Experiments with the Sealed Chamber

$\dot{m}$	Re	$\overline{q''}$	T_i	$\overline{T_c}$	p_o	$\overline{h}$	$\overline{Nu}$	K_L
[g/s]	[−]	[W/m^2]	\multicolumn{2}{c}{[°C]}	[Pa]	[W/m^2·K]	\multicolumn{2}{c}{[−]}
3.06	23103	2884257	31.7	243	9493653	20090	138.55	1.746
4.02	30377	2846347	31.8	205	9516037	24136	168.16	1.669
4.88	36849	2827345	31.6	184	9514727	27345	191.70	1.636
5.83	44067	2797335	31.3	164	9515844	30900	217.75	1.670
6.90	52169	2790888	31.3	149	9492570	34738	245.60	1.738
8.10	61184	2795597	31.5	137	9469677	38992	276.34	1.801
2.91	19217	2114383	100	255	9843192	20050	122.90	1.656
4.04	26639	2551420	100	252	9725467	24709	152.02	1.670
4.95	32677	2596579	100	235	9605657	28329	175.08	1.628
5.91	38991	2647913	100	222	9669598	31762	196.90	1.682
6.95	45870	2708582	100	212	9618726	35525	220.80	1.665
8.03	53025	2753221	100	203	9571668	39295	244.63	1.711
3.07	17261	1696789	200	317	9891397	21333	112.92	1.658
4.04	22740	1769369	199	301	9795968	25407	135.12	1.715
4.96	27895	1808211	200	291	9741885	29062	154.71	1.676
5.90	33117	1844613	200	283	9704147	32739	174.40	1.594
7.03	39511	1882796	200	275	9639771	36698	195.97	1.689
7.89	44370	1920377	200	271	9607267	39595	211.58	1.744
3.21	15814	1844122	299	420	9386168	22435	104.62	1.649
4.22	20840	1887124	298	402	9401854	26621	124.71	1.647
4.95	24392	1898026	300	394	9492280	29516	138.25	1.737
5.92	29134	1922868	300	385	9491747	33345	156.35	1.621
6.98	34369	1941374	300	377	9534946	37219	174.76	1.637
7.73	38116	1972598	300	372	9559480	39871	187.38	1.639

Table B.7 (continued). Flat Design Simulation Results at H = 1.25 mm Based on Experiments with the Sealed Chamber

$\dot{m}$	Re	$\overline{q''}$	T_i	$\overline{T_c}$	p_o	$\bar{h}$	$\overline{Nu}$	K_L
[g/s]	[–]	[W/m^2]	[°C]		[Pa]	[W/m^2·K]	[–]	
3.14	13832	1679365	399	509	9853104	22453	94.15	1.631
3.94	17378	1748458	400	499	9796637	25935	108.91	1.650
4.67	20572	1796762	400	491	9759283	28835	121.24	1.747
5.90	26016	1865592	399	481	9693930	33660	141.77	1.685
6.82	30107	1902420	398	474	9620234	36863	155.56	1.841
3.40	14620	1088054	424	492	9777331	23831	97.92	1.606
4.21	18118	1157924	424	486	9806440	27206	111.96	1.654
6.06	26023	1283196	425	480	9795061	34426	141.72	1.608
6.97	29917	1342263	426	478	9810831	37917	155.99	1.619
7.38	31749	1363611	424	475	9812211	39261	161.85	1.617

Table B.8. HEMJ Simulation Results at Prototypical Conditions (Undeformed Geometry).

$\dot{m}$	Re	$T_{\max}$	$\overline{T_c}$	$T_{cs,\max}$	$T_{cs,\min}$	p_i	$\overline{h}$	$\overline{Nu}$	K_L	$\sigma_v^{\max}$	Max ΔH
[g/s]	[−]			[°C]		[Pa]	[W/m²·K]		[−]	[MPa]	[mm]
3.09	10000	1838	1183	1242	1078	10026847	21128	62.55	1.810	342	0.225
4.63	15000	1703	1048	1100	955	10059600	27531	82.97	1.786	365	0.224
6.18	20000	1623	970	1018	886	10103092	33273	101.19	1.738	377	0.225
6.80	22023	1597	945	992	862	10128401	35740	108.96	1.785	381	0.234
7.72	25000	1569	919	964	842	10166550	38595	118.02	1.797	386	0.224
9.26	30000	1530	883	925	811	10240124	43539	133.63	1.799	393	0.224
10.8	35000	1500	855	895	787	10325209	48335	148.74	1.790	398	0.224
12.4	40000	1476	833	871	768	10425059	52950	163.27	1.792	403	0.224
13.9	45000	1455	814	852	753	10543736	57465	177.47	1.811	406	0.224
15.4	50000	1438	799	835	740	10671333	61856	191.27	1.811	410	0.225

Table B.9. HEMJ Simulation Results at Prototypical Conditions (Deformed Geometry).

$\dot{m}$	Re	$T_{\max}$	$\overline{T_c}$	$T_{\mathrm{cs,max}}$	$T_{\mathrm{cs,min}}$	p_i	$\bar{h}$	$\overline{Nu}$	K_L
[g/s]	[−]			[°C]		[Pa]	[W/m²·K]		[−]
3.09	10000	1858	1199	1260	1100	10022942	20579	60.86	1.547
4.63	15000	1741	1052	1142	986	10054862	27247	81.80	1.644
6.18	20000	1712	976	1106	969	10091764	32767	99.46	1.547
6.80	22023	1613	957	1004	882	10116409	34534	105.09	1.619
7.72	25000	1582	927	973	855	10147532	37669	115.03	1.592
9.26	30000	1543	892	933	823	10219646	42234	129.52	1.646
10.8	35000	1511	863	901	798	10296266	46875	144.15	1.631
12.4	40000	1487	840	878	778	10403832	51288	158.10	1.702
13.9	45000	1467	822	858	763	10489964	55539	171.47	1.632
15.4	50000	1450	806	842	750	10604379	59686	184.53	1.630

Table B.10. Simulation Results for the Flat Design at Prototypical Conditions (Undeformed Geometry).

$\dot{m}$	Re	T_{max}	$\overline{T_c}$	$T_{cs,max}$	$T_{cs,min}$	p_i	$\overline{h}$	$\overline{Nu}$	K_L	σ_v^{max}	Max ΔH
[g/s]	[−]			[°C]		[Pa]	[W/m^2·K]		[−]	[MPa]	[mm]
3.09	11346	1836	1265	1321	1208	10024560	22126	74.44	1.656	299	0.223
4.63	17019	1673	1093	1178	879	10053463	29829	102.07	1.602	384	0.215
6.18	22692	1597	1021	1071	968	10106920	34936	120.61	1.803	372	0.220
6.80	25000	1570	994	1049	941	10119465	37311	129.05	1.661	379	0.222
7.72	28365	1540	965	1015	912	10168473	40272	139.76	1.818	388	0.220
9.26	34038	1495	922	971	871	10228391	45644	158.95	1.711	401	0.221
10.8	39712	1461	891	939	840	10320418	50634	176.81	1.764	411	0.220
12.4	45385	1434	865	912	815	10404396	55606	194.54	1.704	421	0.221
13.9	51058	1411	844	891	795	10520662	60380	211.59	1.734	428	0.221
15.4	56731	1393	827	874	779	10614804	64942	227.89	1.658	435	0.222

Table B.11. Simulation Results for the Flat Design at Prototypical Conditions (Deformed Geometry).

$\dot{m}$	Re	T_{max}	$\overline{T_c}$	$T_{cs,max}$	$T_{cs,min}$	p_i	$\overline{h}$	$\overline{Nu}$	K_L
[g/s]	[−]			[°C]		[Pa]	[W/m²·K]		[−]
3.09	11346	1836	1251	1317	1153	10027646	22607	75.87	1.864
4.63	17019	1675	1088	1147	1006	10059590	30172	103.11	1.786
6.18	22692	1584	998	1059	917	10093074	36973	127.49	1.569
6.80	25000	1549	964	1023	876	10110706	40434	139.79	1.539
7.72	28365	1513	930	988	844	10150836	44581	154.60	1.628
9.26	34038	1465	884	943	803	10216959	51754	180.15	1.626
10.8	39712	1435	857	915	774	10324701	57363	200.25	1.787
12.4	45385	1408	831	891	752	10386773	63639	222.57	1.630
13.9	51058	1386	811	871	734	10487287	69694	244.13	1.623
15.4	56731	1355	784	834	716	10616596	80097	280.93	1.663

Table B.12. Jet Array Optimization Results for $H = 0.50$ mm at Prototypical Conditions.

Jet Design	D	T_{max}	$\overline{T_c}$	p_i	$\overline{h}$	$\overline{Nu}$	K_L	σ_v^{max}	Max ΔH
	[mm]	[°C]		[MPa]	[W/m²·K]	[–]		[MPa]	[mm]
A	3.120	1668	943	10246571	35870	328.44	3.428	418	0.229
B	1.178	982	1720	10145848	10977	37.96	2.028	365	0.227
C	0.865	1726	994	10131838	31234	79.27	1.833	348	0.230
D	1.178	1713	972	10138172	33077	114.40	1.921	464	0.229
E	0.865	1698	959	10121076	34224	86.85	1.683	383	0.230
F	0.715	1689	951	10124936	35025	73.53	1.737	401	0.232
G	0.624	1681	947	10121850	35414	64.81	1.694	381	0.231
H	0.624	1683	946	10127688	35555	65.07	1.775	402	0.232
I	1.040	1684	947	10130516	35454	108.21	1.815	398	0.227
J	3.120	1497	991	10216496	37607	344.35	3.010	381	0.224
K	1.178	1480	979	10134930	38827	134.29	1.876	398	0.229
L	0.715	1443	944	10162228	42727	89.69	2.256	437	0.236
M	0.624	1392	903	10122081	48561	88.87	1.697	438	0.241
N	0.624	1501	1005	10132614	36307	66.44	1.844	413	0.230
O	0.513	1445	946	10139378	42463	63.88	1.938	397	0.230

Table B.13. Jet Array Optimization Results for $H = 0.75$ mm at Prototypical Conditions.

Jet Design	D	T_{max}	$\overline{T_c}$	p_i	$\overline{h}$	$\overline{Nu}$	K_L	σ_v^{max}	Max ΔH
	[mm]	[°C]		[MPa]	[W/m²·K]	[–]		[MPa]	[mm]
A	3.120	1745	1013	10167916	29760	272.50	2.335	361	0.217
B	1.178	1713	975	10117408	32823	113.52	1.632	361	0.226
C	0.865	1723	990	10123893	31546	80.06	1.723	344	0.228
D	1.178	1709	968	10118499	33413	115.56	1.648	460	0.226
E	0.865	1701	962	10120366	33987	86.25	1.674	386	0.229
F	0.715	1690	952	10122171	34934	73.34	1.699	402	0.227
G	0.624	1687	952	10118311	34916	63.90	1.645	384	0.228
H	0.624	1678	941	10127522	36061	65.99	1.773	401	0.228
I	1.040	1685	948	10126785	35370	107.95	1.763	390	0.228
J	3.120	1532	1025	10153389	34570	316.54	2.133	375	0.218
K	1.178	1585	1005	10125450	36294	125.53	1.744	388	0.223
L	0.715	1467	967	10147481	40114	84.21	2.051	408	0.226
M	0.624	1453	958	10136853	41042	75.11	1.903	431	0.229
N	0.624	1450	957	10133804	41239	75.47	1.860	430	0.228
O	0.513	1441	943	10156294	42830	64.43	2.173	403	0.229

Table B.14. Jet Array Optimization Results for $H = 0.90$ mm at Prototypical Conditions.

Jet Design	D	T_{max}	$\overline{T_c}$	p_i	$\bar{h}$	$\overline{Nu}$	K_L	σ_v^{max}	Max ΔH
	[mm]	[°C]		[MPa]	[W/m²·K]	[–]		[MPa]	[mm]
A	3.120	1751	1019	10142790	29370	268.92	1.985	354	0.215
B	1.178	1710	971	10112609	33120	114.55	1.566	357	0.225
C	0.865	1723	990	10122693	31540	80.04	1.706	343	0.225
D	1.178	1647	910	10294884	39662	137.17	4.100	377	0.222
E	0.865	1700	960	10120795	34157	86.69	1.680	385	0.228
F	0.715	1690	951	10122220	35003	73.48	1.699	400	0.225
G	0.624	1688	953	10118326	34805	63.70	1.645	379	0.226
H	0.624	1680	942	10135265	35985	65.85	1.881	395	0.226
I	1.040	1597	945	10128401	35740	108.96	1.785	381	0.235
J	3.120	1540	1035	10137390	33830	309.76	1.910	351	0.222
K	1.178	1575	997	10121958	37065	128.19	1.696	391	0.223
L	0.715	1475	976	10141567	39123	82.13	1.968	383	0.224
M	0.624	1478	981	10125867	38590	70.62	1.750	435	0.224
N	0.624	1490	993	10141000	37408	68.46	1.960	426	0.230
O	0.513	1462	963	10132552	40541	60.99	1.843	395	0.225

Table B.15. Jet Array Optimization Results for $H = 1.25$ mm at Prototypical Conditions.

Jet Design	D	T_{max}	$\overline{T_c}$	p_i	$\bar{h}$	$\overline{Nu}$	K_L	σ_v^{max}	Max ΔH
	[mm]	[°C]		[MPa]	[W/m²·K]	[–]		[MPa]	[mm]
A	3.120	1728	995	10119429	31129	285.03	1.661	335	0.216
B	1.178	1708	969	10113796	33306	115.19	1.582	357	0.222
C	0.865	1728	994	10121720	31227	79.25	1.692	342	0.221
D	1.178	1708	968	10202400	33450	115.69	2.814	357	0.220
E	0.865	1705	964	10122537	33735	85.61	1.704	380	0.224
F	0.715	1699	959	10123920	34237	71.87	1.723	390	0.221
G	0.624	1696	960	10119234	34118	62.44	1.658	370	0.223
H	0.624	1695	956	10133773	34539	63.21	1.860	388	0.222
I	1.040	1684	947	10129154	35469	108.25	1.796	401	0.219
J	3.120	1527	1025	10124854	34617	316.97	1.736	354	0.216
K	1.178	1570	994	10119465	37311	129.04	1.661	379	0.222
L	0.715	1432	935	10161848	43880	92.11	2.250	419	0.229
M	0.624	1490	993	10128823	37401	68.45	1.791	426	0.220
N	0.624	1490	991	10137000	37609	68.83	1.905	421	0.220
O	0.513	1447	948	10141276	42222	63.52	1.964	398	0.221

Table B.16. Jet Array Optimization Results for $H = 1.50$ mm at Prototypical Conditions.

Jet Design	D	T_{max}	$\overline{T_c}$	p_i	$\bar{h}$	$\overline{Nu}$	K_L	σ_v^{max}	Max ΔH
	[mm]	[°C]		[MPa]	[W/m²·K]	[–]		[MPa]	[mm]
A	3.120	1729	995	10112904	31103	284.79	1.570	330	0.215
B	1.178	1708	970	10114274	33268	115.06	1.589	355	0.221
C	0.865	1732	998	10121397	30881	78.37	1.688	341	0.217
D	1.178	1726	984	10154820	32029	110.77	2.153	446	0.216
E	0.865	1710	969	10123650	33305	84.52	1.719	376	0.221
F	0.715	1704	964	10124991	33764	70.88	1.738	385	0.219
G	0.624	1704	968	10119740	33436	61.19	1.665	362	0.220
H	0.624	1707	967	10143373	33531	61.36	1.993	379	0.219
I	1.040	1699	960	10130958	34173	104.30	1.821	373	0.219
J	3.120	1520	1020	10122638	35027	320.72	1.705	346	0.217
K	1.178	1578	1003	10122340	36505	126.25	1.701	374	0.217
L	0.715	1502	1003	10137473	36472	76.56	1.911	366	0.216
M	0.624	1498	1002	10129756	36609	67.00	1.804	420	0.223
N	0.624	1493	995	10127000	37256	68.18	1.766	413	0.215
O	0.513	1437	939	10137564	43367	65.24	1.913	405	0.221

APPENDIX C: MATERIAL PROPERTIES

Accurate material properties are required to ensure the validity of the results and conclusions drawn from experimental data and numerical simulations. This section summarizes the solid and coolant material properties that were used to perform the calculations presented in this thesis. These properties were obtained from a number of different sources, and temperature-dependent properties were used whenever possible.

C.1. Fluid Properties

All of the experiments in this work were conducted with a single coolant: high purity (99.997%) helium at approximately 10 MPa. Calculations involving helium properties were therefore performed assuming that the properties only changed with temperature, and obeyed the ideal gas law. Table C.1 shows the temperature-dependent properties of helium at 10 MPa based on data available from NIST [91].

Table C.1. Temperature-dependent properties of He at 10 MPa [91].

T (K)	ρ (kg/m^3)	c_p (J/kg·K)	μ (μPa·s)	k (W/m·K)
250	18.23	5191	18.10	0.144
275	16.66	5189	19.19	0.153
300	15.34	5187	20.26	0.162
325	14.22	5186	21.36	0.171
350	13.24	5185	22.44	0.179
375	12.40	5185	23.50	0.188
400	11.65	5185	24.54	0.196
425	10.99	5185	25.57	0.204
450	10.40	5185	26.58	0.212
475	9.866	5185	27.58	0.220

Table C.1 (continued). Temperature-dependent properties of He at 10 MPa [91].

T (K)	ρ (kg/m³)	c_p (J/kg·K)	μ (μPa·s)	k (W/m·K)
500	9.387	5185	28.56	0.228
525	8.953	5185	29.54	0.235
550	8.556	5185	30.50	0.243
575	8.194	5186	31.45	0.250
600	7.860	5186	32.38	0.257
625	7.553	5186	33.31	0.265
650	7.269	5186	34.23	0.272
675	7.005	5186	35.14	0.279
700	6.760	5187	36.04	0.286
725	6.531	5187	36.93	0.293
750	6.318	5187	37.81	0.300
775	6.118	5187	38.69	0.307
800	5.930	5187	39.56	0.313
825	5.753	5187	40.42	0.320
850	5.586	5188	41.27	0.327
875	5.429	5188	42.12	0.333
900	5.281	5188	42.96	0.340
925	5.140	5188	43.79	0.346
950	5.007	5188	44.62	0.352
975	4.880	5188	45.45	0.359
1000	4.760	5188	46.26	0.365

C.2. Solid Material Properties

The divertor modules used in this work were composed of two different tungsten alloys: MT185 and WL10. Since only steady-state conduction through the module was studied here, the most important solid material property was the thermal conductivity. The thermal conductivity of WL10 was reported by Roedig *et al*. who performed laser flash measurements at temperatures ranging from 24 °C to 1400 °C [92]. Table C.2 shows the discrete WL10 thermal conductivity values at seven different temperatures.

Table C.2. Temperature-dependent thermal conductivity of WL10 [92].

T (K)	$k_{s,WL10}$ (W/m·K)
297.07	176.50
373.15	170.83
673.15	139.03
1073.15	127.58
1273.15	115.92
1473.15	111.79
1673.15	108.99

These values were fitted with a second-order polynomial (Eq. 3.5) to obtain thermal conductivity values between each discrete temperature.

The thermal conductivity of MT185 was based on laser flash measurements taken at ORNL for temperatures ranging from ~27 °C to ~727 °C [32]. The thermal conductivity at 15 different temperatures are given in Table C.3. These data were fitted to a third-order polynomial (Eq. 3.6) and used for the calculations in the experiments and simulations.

Table C.3. Temperature-dependent thermal conductivity of MT185 [32].

T (K)	$k_{s,MT185}$ (W/m·K)
300	80.46
350	81.94
400	83.23
450	84.37
500	85.36
550	86.23
600	86.98
650	87.63
700	88.16
750	88.60
800	88.93
850	89.17
900	89.32
950	89.38
1000	89.34

APPENDIX D: UNCERTAINTY ANALYSIS

This appendix summarizes the procedure used to estimate the uncertainties in the experimental results. The total uncertainty for derived quantities (*e.g.*, heat flux, Nusselt number, loss coefficient) was determined using a standard error-propagation procedure that includes uncertainty in the independent variables (*i.e.*, measured quantities, material properties, and geometric dimensions). The error propagation for a derived result $R = f(x_1, x_2, ..., x_n)$ was calculated using the root-sum-squared technique

$$U_R(x_1, x_2, ..., x_n) = \pm \sqrt{\sum_{i=1}^{n} \left(U_{x_i} \frac{\partial R}{\partial x_i} \right)^2} \tag{D.1}$$

where x_i is an independent variable, U_{x_i} is the uncertainty interval of x_i, and U_R is the total uncertainty of R [102]. The partial derivative terms are known as sensitivity coefficients, which provide a reasonable approximation of the error propagation if variations in x_i are small.

D.1. Uncertainty in the Geometric Dimensions

The uncertainty in the geometric dimensions of the test sections used in this work are summarized in Table D.1. These uncertainties have the smallest contribution to the total uncertainties of the derived results.

Table D.1. Uncertainty in the geometric dimensions.

Dimension	Uncertainty	Units
D_j	0.05	mm
D_o	0.05	mm
δ_{TC}	0.10	mm
A_c	2.03	mm^2
A_h	1.33	mm^2
A_j	0.09	mm^2

D.2. Uncertainty in the Material Properties

The uncertainty in the material properties of the solids and coolant was either assumed to be that specified by the supplier, or conservatively assumed to be as great as 10%. These uncertainties are summarized in Table D.2.

Table D.2. Uncertainty in the material properties.

Material or Coolant	Property	Uncertainty (%)
Helium	c_p	5
	k	5
	μ	10
MT185	k_s	5
WL10	k_s	5

D.3. Uncertainty in the Instruments

The uncertainties for all the measurement instrumentation used in this work were available from the manufacturer. Each instrument and its associated uncertainty is listed in Table D.3.

Table D.3. Uncertainty in the instruments.

Instrument	Uncertainty	Units
Dwyer 626-16-GH-P1-E2-S1	25855	Pa
OMEGA KMQXL-020U-6	1.1 (< 275 °C) $0.004T$ (≥ 275 °C)	°C
OMEGA P-M-A-1/8-6-0-TS-8	$0.15 + 0.002T$	°C
OMEGA PX309-2KGI	34474	Pa
Rosemount 1151DP4E22	12	Pa
Rosemount 1151DP5S22	329	Pa

REFERENCES

[1]   IPCC, "Climate Change 2014: Synthesis Report. Contribution of Working Groups I, II and III to the Fifth Assessment Report of the Intergovernmental Panel on Climate Change," IPCC, Geneva, Switzerland, 2014.

[2]   J. R. Petit, J. Jouzel, D. Raynaud, N. I. Barkov, J. M. Barnola, I. Basile, *et al.*, "Climate and Atmospheric History of the Past 420,000 Years from the Vostok Ice Core, Antarctica," ed, 1999.

[3]   NASA. (2016). *Global Climate Change: Vital Signs of the Planet: Carbon Dioxide*. Available: http://climate.nasa.gov/vital-signs/carbon-dioxide/

[4]   FESAC, "Report on Strategic Planning," U.S. Department of Energy Office of Science, 2014.

[5]   T. E. Brown, H. E. LeMay, B. E. Bursten, C. Murphy, P. Woodward, and M. E. Stoltzfus, *Chemistry: The Central Science*: Pearson Education, 2017.

[6]   S. Atzeni, J. Meyer-ter-Vehn, *The Physics of Inertial Fusion: Beam Plasma Interaction, Hydrodynamics, Hot Dense Matter*: Clarendon Press-Oxford, 2004.

[7]   "Fusion - A Clean Future," ed. Culham Centre for Fusion Energy, 2012.

[8]   D. Bradley, Jaskula B., "Lithium—for Harnessing Renewable Energy: U.S. Geological Survey Fact Sheet 2014–3035," 2014.

[9]   M. Steinberg and V. D. Dang, *Preliminary Design and Analysis of a Process for the Extraction of Lithium from Seawater*: Brookhaven National Lab, 1975.

[10]   E. Böhm-Vitense, *Introduction to Stellar Astrophysics*: Cambridge University Press, 1992.

[11]   L. Spitzer, "The Stellarator Concept," *Physics of Fluids,* vol. 1, pp. 253-264, 1958.

[12]   R. Wolf, "Fusion Research: On the Way to a New Primary Energy Source ", ed, 2013.

[13]   V. P. Smirnov, "Tokamak Foundation in USSR/Russia 1950–1990," *Nuclear Fusion,* vol. 50, p. 014003, 2010.

[14] *ITER Organization*. Available: https://www.iter.org/

[15] M. Abdou, N. B. Morley, S. Smolentsev, A. Ying, S. Malang, A. Rowcliffe*, et al.*, "Blanket/First Wall Challenges and Required R&D on the Pathway to Demo," *Fusion Engineering and Design,* vol. 100, pp. 2-43, 2015.

[16] G. H. Neilson, G. Federici, J. Li, D. Maisonnier, and R. Wolf, "Summary of the International Workshop on Magnetic Fusion Energy (MFE) Roadmapping in the ITER Era," *Nuclear Fusion,* vol. 52, p. 047001, 2012.

[17] P. C. Stangeby, *The Plasma Boundary of Magnetic Fusion Devices* vol. 224: Institute of Physics Publishing Bristol, 2000.

[18] EUROfusion. (2016). *Snowflake and the Multiple Divertor Concepts*. Available: https://www.euro-fusion.org/newsletter/divertor-concepts/

[19] Y. Igitkhanov, B. Bazylev, and R. Fetzer, *The Quantification of the Key Physics Parameters for the DEMO Fusion Power Reactor and Analysis of the Reactor Relevant Physics Issues*: KIT Scientific Publishing, 2015.

[20] M. Kotschenreuther, P. Valanju, S. Mahajan, L. J. Zheng, L. D. Pearlstein, R. H. Bulmer*, et al.*, "The Super X Divertor (SXD) and a Compact Fusion Neutron Source (CFNS)," *Nuclear Fusion,* vol. 50, p. 035003, 2010.

[21] D. D. Ryutov, R. H. Cohen, T. D. Rognlien, and M. V. Umansky, "A Snowflake Divertor: A Possible Solution to the Power Exhaust Problem for Tokamaks," *Plasma Physics and Controlled Fusion,* vol. 54, p. 124050, 2012.

[22] T. Loarer, S. Brezinsek, V. Philipps, J. Bucalossi, D. Douai, H. G. Esser*, et al.*, "Comparison of Long Term Fuel Retention in JET between Carbon and the ITER-Like Wall," *Journal of Nuclear Materials,* vol. 438, Supplement, pp. S108-S113, 2013.

[23] R. Behrisch and W. Eckstein, *Sputtering by Particle Bombardment: Experiments and Computer Calculations from Threshold to Mev Energies*: Springer Berlin Heidelberg, 2007.

[24] M. R. Gilbert and J.-C. Sublet, "Neutron-Induced Transmutation Effects in W and W-Alloys in a Fusion Environment," *Nuclear Fusion,* vol. 51, p. 043005, 2011.

[25] F. W. Meyer, H. Hijazi, M. E. Bannister, P. S. Krstic, J. Dadras, I. H. M. Meyer*, et al.*, "He-Ion and Self-Atom Induced Damage and Surface-Morphology Changes of a Hot W Target," *Physica Scripta,* vol. 2014, p. 014029, 2014.

[26]   D. Donovan, D. Buchenauer, J. Whaley, and R. Friddle, "Characterization of a Compact ECR Plasma Source and Its Applications to Studies of Helium Ion Damage to Tungsten," *Physica Scripta,* vol. 2016, p. 014040, 2016.

[27]   M. S. Tillack, P. W. Humrickhouse, S. Malang, and A. F. Rowcliffe, "The Use of Water in a Fusion Power Core," *Fusion Engineering and Design,* vol. 91, pp. 52-59, 2015.

[28]   P. Norajitra, *Divertor Development for a Future Fusion Power Plant*: Karlsruhe Institute of Technology, 2011.

[29]   C. E. Kessel, M. S. Tillack, F. Najmabadi, F. M. Poli, K. Ghantous, N. Gorelenkov*, et al.*, "The ARIES Advanced and Conservative Tokamak Power Plant Study," *Fusion Science and Technology,* vol. 67, pp. 1-21, 2015.

[30]   M. Hageman, "Experimental Investigation of the Thermal Performance of Gas-Cooled Divertor Plate Concepts," M.S. Thesis, George W. Woodruff School of Mechanical Engineering, Georgia Institute of Technology, 2010.

[31]   J. D. Rader, "Thermal Performance of Finger-Type Gas-Cooled Divertors," Ph.D. Dissertation, George W. Woodruff School of Mechanical Engineering, Georgia Institute of Technology, 2013.

[32]   B. H. Mills, "On the Use of Dynamically Similar Experiments to Evaluate the Thermal Performance of Helium-Cooled Tungsten Divertors," Ph.D. Dissertation, George W. Woodruff School of Mechanical Engineering, Georgia Institute of Technology, 2014.

[33]   "ANSYS Fluent Theory Guide," ed. ANSYS, Inc., ANSYS Release 16.2.

[34]   B. E. Launder and D. B. Spalding, "The Numerical Computation of Turbulent Flows," *Computer Methods in Applied Mechanics and Engineering,* vol. 3, pp. 269-289, 1974.

[35]   W. M. Kays, "Turbulent Prandtl Number—Where Are We?," *Journal of Heat Transfer,* vol. 116, pp. 284-295, 1994.

[36]   J. N. B. Livingood, Hrycak, P., "Impingement Heat Transfer from Turbulent Air Stream Jets to Flat Plates," NASA, 1973.

[37]   D. Cooper, D. C. Jackson, B. E. Launder, and G. X. Liao, "Impinging Jet Studies for Turbulence Model Assessment—I. Flow-Field Experiments," *International Journal of Heat and Mass Transfer,* vol. 36, pp. 2675-2684, 1993.

[38] F. P. Incropera, *Fundamentals of Heat and Mass Transfer*, 7 ed. Hoboken, New Jersey: Wiley, 2011.

[39] L. F. G. Geers, "Multiple Impinging Jet Arrays: An Experimental Study on Flow and Heat Transfer," Ph.D. Dissertation, Delft University of Technology, 2004.

[40] H. Glaser, "Untersuchungen an Schlitz- Und Mehrdüsenanordnungen Bei Der Trocknung Feuchter Oberflächen Durch Warmluftstrahlen," *Chemie Ingenieur Technik,* vol. 34, pp. 200-207, 1962.

[41] B. Weigand and S. Spring, "Multiple Jet Impingement - A Review," *Heat Transfer Research,* vol. 42, pp. 101-142, 2011.

[42] R. Viskanta, "Heat Transfer to Impinging Isothermal Gas and Flame Jets," *Experimental Thermal and Fluid Science,* vol. 6, pp. 111-134, 1993.

[43] A. I. Behbahani and R. J. Goldstein, "Local Heat Transfer to Staggered Arrays of Impinging Circular Air Jets," *Journal of Engineering for Power,* vol. 105, pp. 354-360, 1983.

[44] B. Han and R. J. Goldstein, "Jet-Impingement Heat Transfer in Gas Turbine Systems," *Annals of the New York Academy of Sciences,* vol. 934, pp. 147-161, 2001.

[45] D. M. Kercher and W. Tabakoff, "Heat Transfer by a Square Array of Round Air Jets Impinging Perpendicular to a Flat Surface Including the Effect of Spent Air," *Journal of Engineering for Power,* vol. 92, pp. 73-82, 1970.

[46] R. J. Goldstein and J. F. Timmers, "Visualization of Heat Transfer from Arrays of Impinging Jets," *International Journal of Heat and Mass Transfer,* vol. 25, pp. 1857-1868, 1982.

[47] S. V. Garimella and V. P. Schroeder, "Local Heat Transfer Distributions in Confined Multiple Air Jet Impingement," *Journal of Electronic Packaging,* vol. 123, pp. 165-172, 2000.

[48] A. M. Huber and R. Viskanta, "Effect of Jet-Jet Spacing on Convective Heat Transfer to Confined, Impinging Arrays of Axisymmetric Air Jets," *International Journal of Heat and Mass Transfer,* vol. 37, pp. 2859-2869, 1994.

[49] B. R. Hollworth and R. D. Berry, "Heat Transfer from Arrays of Impinging Jets with Large Jet-to-Jet Spacing," *Journal of Heat Transfer,* vol. 100, pp. 352-357, 1978.

[50]   A. M. Huber and R. Viskanta, "Comparison of Convective Heat Transfer to Perimeter and Center Jets in a Confined, Impinging Array of Axisymmetric Air Jets," *International Journal of Heat and Mass Transfer,* vol. 37, pp. 3025-3030, 1994.

[51]   B. R. Hollworth and G. H. Cole, "Heat Transfer to Arrays of Impinging Jets in a Crossflow," *J. Tubomach.,* vol. 109, pp. 564-571, 1987.

[52]   V. Katti and S. V. Prabhu, "Influence of Spanwise Pitch on Local Heat Transfer Distribution for in-Line Arrays of Circular Jets with Spent Air Flow in Two Opposite Directions," *Experimental Thermal and Fluid Science,* vol. 33, pp. 84-95, 2008.

[53]   M. A. M. Attalla, "Experimental Investigation of Heat Transfer Characteristics from Arrays of Free Impinging Circular Jets and Hole Channels," Ph.D. Dissertation, Otto-von-Guericke University Magdeburg, 2005.

[54]   J.-Y. San and M.-D. Lai, "Optimum Jet-to-Jet Spacing of Heat Transfer for Staggered Arrays of Impinging Air Jets," *International Journal of Heat and Mass Transfer,* vol. 44, pp. 3997-4007, 2001.

[55]   K. R. Saripalli, "Visualization of Flow Patterns Induced by an Impinging Jet Issuing from a Circular Planform," *AIAA Journal,* vol. 21, pp. 1764-1766, 1983.

[56]   N. T. Obot and T. A. Trabold, "Impingement Heat Transfer within Arrays of Circular Jets: Part 1—Effects of Minimum, Intermediate, and Complete Crossflow for Small and Large Spacings," *Journal of Heat Transfer,* vol. 109, pp. 872-879, 1987.

[57]   H. Thomann, "Effect of Streamwise Wall Curvature on Heat Transfer in a Turbulent Boundary Layer," *Journal of Fluid Mechanics,* vol. 33, pp. 283-292, 1968.

[58]   R. Ito, K. Takeishi, Y. Oda, and N. Yoshida, "Heat Transfer for Round Air Jets Flowing Along a Concave Surface," in *ASME/JSME 2007 Thermal Engineering Heat Transfer Summer Conference collocated with the ASME 2007 InterPACK Conference*, 2007, pp. 597-605.

[59]   S. N. Yasaswy, V. V. Katti, and S. V. Prabhu, "Heat Transfer Distribution of Semicylindrical Concave Surface Impinged by Circular Jet Rows," *Journal of Thermophysics and Heat Transfer,* vol. 24, pp. 765-776, 2010.

[60]   P. Norajira, *et al.*, "Conceptual Design of a He-Cooled Divertor with Integrated Flow and Heat Transfer Promotors (PPCS Subtask TW3-TRP-001-D2)," Forschungszentrum Karlsruhe, 2004.

[61]   T. Ihli, S. Hermsmeyer, C. Köhly, and P. Norajitra, "Integration of an Advanced He-Cooled Divertor in a DEMO-Relevant Tokamak Geometry," *Fusion Engineering and Design,* vol. 81, pp. 121-126, 2006.

[62]   S. Hermsmeyer and K. Kleefeldt, "Review and Comparative Assessment of Helium-Cooled Divertor Concepts," Forschungszentrum Karlsruhe, 2001.

[63]   I. Ovchinnikov, R. Giniyatulin, T. Ihli, G. Janeschitz, A. Komarov, R. Kruessmann*, et al.*, "Experimental Study of DEMO Helium Cooled Divertor Target Mock-Ups to Estimate Their Thermal and Pumping Efficiencies," *Fusion Engineering and Design,* vol. 73, pp. 181-186, 2005.

[64]   P. Norajira, *et al.*, "Status of He-Cooled Divertor Development (PPCS Subtask TW4-TRP-001-D2)," Forschungszentrum Karlsruhe, 2005.

[65]   P. Norajitra, A. Gervash, R. Giniyatulin, T. Ihli, W. Krauss, R. Kruessmann*, et al.*, "He-Cooled Divertor for DEMO: Experimental Verification of the Conceptual Modular Design," *Fusion Engineering and Design,* vol. 81, pp. 341-346, 2006.

[66]   P. Norajitra, R. Giniyatulin, T. Ihli, G. Janeschitz, W. Krauss, R. Kruessmann*, et al.*, "He-Cooled Divertor Development for DEMO," *Fusion Engineering and Design,* vol. 82, pp. 2740-2744, 2007.

[67]   P. Norajitra, R. Giniyatulin, V. Kuznetsov, I. V. Mazul, and G. Ritz, "He-Cooled Divertor for DEMO: Status of Development and HHF Tests," *Fusion Engineering and Design,* vol. 85, pp. 2251-2256, 2010.

[68]   G. Ritz, T. Hirai, J. Linke, P. Norajitra, R. Giniyatulin, and L. Singheiser, "Post-Examination of Helium-Cooled Tungsten Components Exposed to DEMO Specific Cyclic Thermal Loads," *Fusion Engineering and Design,* vol. 84, pp. 1623-1627, 2009.

[69]   P. Norajitra, W. W. Basuki, R. Giniyatulin, C. Hernandez, V. Kuznetsov, I. V. Mazoul*, et al.*, "Recent Progress in the Development of Helium-Cooled Divertor for DEMO," *Fusion Science and Technology,* vol. 67, pp. 732-744, 2015.

[70]   P. Norajitra, *et al.*, "Status and Prospects of the EU Development of the He-Cooled Divertor for DEMO Power Plant," in *ISFNT 2013*, Barcelona, 2013.

[71]   J. B. Weathers, "Thermal Performance of Helium-Cooled Divertors for Magnetic Fusion Applications," M.S. Thesis, George W. Woodruff School of Mechanical Engineering, Georgia Institute of Technology, 2007.

[72]   J. B. Weathers, L. Crosatti, R. Kruessmann, D. L. Sadowski, and S. I. Abdel-Khalik, "Development of Modular Helium-Cooled Divertor for DEMO Based on the Multi-Jet Impingement (HEMJ) Concept: Experimental Validation of Thermal Performance," *Fusion Engineering and Design,* vol. 83, pp. 1120-1125, 2008.

[73]   L. Crosatti, "Experimental and Numerical Investigation of the Thermal Performance of Gas-Cooled Divertor Modules," Ph.D. Dissertation, George W. Woodruff School of Mechanical Engineering, Georgia Institute of Technology, 2008.

[74]   L. Crosatti, J. B. Weathers, D. L. Sadowski, S. I. Abdel-Khalik, M. Yoda, R. Kruessmann*, et al.*, "Experimental and Numerical Investigation of Prototypical Multi-Jet Impingement (HEMJ) Helium-Cooled Divertor Modules," *Fusion Science and Technology,* vol. 56, pp. 70-74, 2009.

[75]   J. D. Rader, B. H. Mills, D. L. Sadowski, M. Yoda, and S. I. Abdel-Khalik, "Verification of Thermal Performance Predictions of Prototypical Multi-Jet Impingement Helium-Cooled Divertor Module," *Fusion Science and Technology,* vol. 64, pp. 282-287, 2013.

[76]   B. H. Mills, B. Zhao, S. I. Abdel-Khalik, and M. Yoda, "An Experimental Study of the Helium-Cooled Modular Divertor with Multiple Jets at Nearly Prototypical Conditions," *Fusion Science and Technology,* vol. 68, pp. 541-545, 2015.

[77]   E. Diegele, R. Kruessmann, S. Malang, P. Norajitra, and G. Rizzi, "Modular He-Cooled Divertor for Power Plant Application," *Fusion Engineering and Design,* vol. 66–68, pp. 383-387, 2003.

[78]   P. Norajira, *et al.*, "Assessment of the Integration of a He-Cooled Divertor System in the Power Conversion System for the Dual-Coolant Blanket Concept (PPCS Subtask TW2-TRP-PPCS12D8)," Forschungszentrum Karlsruhe, 2002.

[79]   J. D. Rader, B. H. Mills, D. L. Sadowski, M. Yoda, and S. I. Abdel-Khalik, "Experimental and Numerical Investigation of Thermal Performance of Gas-Cooled Jet-Impingement Finger-Type Divertor Concept," *Fusion Science and Technology,* vol. 60, pp. 223-227, 2011.

[80]   B. H. Mills, J. D. Rader, D. L. Sadowski, S. I. Abdel-Khalik, and M. Yoda, "Experimental Investigation of Fin Enhancement for Gas-Cooled Divertor Concepts," *Fusion Science and Technology,* vol. 60, pp. 190-196, 2011.

[81]   B. H. Mills, J. D. Rader, D. L. Sadowski, M. Yoda, and S. I. Abdel-Khalik, "Dynamically Similar Studies of the Thermal Performance of Helium-Cooled Finger-Type Divertors with and without Fins," *Fusion Science and Technology,* vol. 62, pp. 379-388, 2012.

[82]   T. Ihli, A. R. Raffray, S. I. Abdel-Khalik, and S. Shin, "Design and Performance Study of the Helium-Cooled T-Tube Divertor Concept," *Fusion Engineering and Design,* vol. 82, pp. 249-264, 2007.

[83]   J. A. Burke, X. R. Wang, and M. S. Tillack, "Optimization of the ARIES T-Tube Divertor Concept," *Fusion Science and Technology,* vol. 60, pp. 213-217, 2011.

[84]   X. R. Wang, S. Malang, and A. R. Raffray, "Design Optimization of High-Performance Helium-Cooled Divertor Plate Concept," *Fusion Science and Technology,* vol. 56, pp. 1023-1027, 2009.

[85]   M. S. Tillack, A. R. Raffray, X. R. Wang, S. Malang, S. I. Abdel-Khalik, M. Yoda*, et al.*, "Recent U.S. Activities on Advanced He-Cooled W-Alloy Divertor Concepts for Fusion Power Plants," *Fusion Engineering and Design,* vol. 86, pp. 71-98, 2011.

[86]   X. R. Wang, S. Malang, M. S. Tillack, and J. Burke, "Recent Improvements of the Helium-Cooled W-Based Divertor for Fusion Power Plants," *Fusion Engineering and Design,* vol. 87, pp. 732-736, 2012.

[87]   Y. Igitkhanov, R. Fetzer, and B. Bazylev, "Effect of Design Geometry of the DEMO First Wall on the Plasma Heat Load," *Nuclear Materials and Energy,* vol. 9, pp. 560-564, 2016.

[88]   A. R. Raffray, S. Malang, and X. R. Wang, "Optimizing the Overall Configuration of a He-Cooled W-Alloy Divertor for a Power Plant," *Fusion Engineering and Design,* vol. 84, pp. 1553-1557, 2009.

[89]   R. Kruessmann, *et al.*, "Overview of Thermohydraulic Simulations for the Development of a Helium-Cooled Divertor," Forschungszentrum Karlsruhe, 2008.

[90]   X. R. Wang, S. Malang, M. S. Tillack, and the ARIES Team, "High Performance Divertor Target Plate for a Power Plant: A Combination of Plate and Finger Concepts," *Fusion Science and Technology,* vol. 60, pp. 218-222, 2011.

[91]   *NIST Chemistry Webbook.* Available: http://webbook.nist.gov

[92]   M. Roedig, W. Kuehnlein, J. Linke, D. Pitzer, M. Merola, E. Rigal, *et al.*, "Post Irradiation Testing of Samples from the Irradiation Experiments Paride 3 and Paride 4," *Journal of Nuclear Materials,* vol. 329–333, Part A, pp. 766-770, 2004.

[93]   W. F. Gale and T. C. Totemeier, *Smithells Metals Reference Book*: Elsevier Science, 2003.

[94]   *ITER Materials Properties Handbook*: ITER Doc. G 74 MA 16 04-05-07 R0.1.

[95]   P. D. Harvey, *Engineering Properties of Steel*: American Society for Metals, 1982.

[96]   X.-X. Zhang, Q.-Z. Yan, C.-T. Yang, T.-N. Wang, M. Xia, and C.-C. Ge, "Recrystallization Temperature of Tungsten with Different Deformation Degrees," *Rare Metals,* vol. 35, pp. 566-570, 2016.

[97]   M. Rieth and B. Dafferner, "Limitations of W and W–1%La2o3 for Use as Structural Materials," *Journal of Nuclear Materials,* vol. 342, pp. 20-25, 2005.

[98]   B. Končar, I. Simonovski, and M. Draksler, "Influence of Multiple Jet Cooling on the Heat Transfer and Thermal Stresses in DEMO Divertor Cooling Finger," *Fusion Engineering and Design,* vol. 86, pp. 167-173, 2011.

[99]   ASME, *Boiler and Pressure Vessel Code*, 2011.

[100]   E. F. Gayton, "Experimental and Numerical Investigation of the Thermal Performance of the Gas-Cooled Divertor Plate Concept," M.S. Thesis, George W. Woodruff School of Mechanical Engineering, Georgia Institute of Technology, 2008.

[101]   V. Barabash, G. Federici, J. Linke, and C. H. Wu, "Material/Plasma Surface Interaction Issues Following Neutron Damage," *Journal of Nuclear Materials,* vol. 313, pp. 42-51, 2003/03/01/ 2003.

[102]   S. J. Kline and F. A. McClintock, "Describing Uncertainties in Single-Sample Experiments," *Mechanical Engineering,* vol. 75, 1953.